4-24-2024

Advancements in Scanning Electron Microscopy

Surya Kamal
sk9559@rit.edu

Advancements in Scanning Electron Microscopy

by

Surya Kamal

M.S. Physics, Rochester Institute of Technology (2021)

A dissertation submitted in partial fulfillment

of the requirements towards the degree of

Doctor of Philosophy in *Imaging Science*

at the

ROCHESTER INSTITUTE OF TECHNOLOGY

Chester F. Carlson Center for Imaging Science,

College of Science, Rochester Institute of Technology,

Rochester, New York, USA

24^{th} *April* 2024

Author's Signature _____

Certified by _____ _____

Ph.D. Program Director Date

CHESTER F. CARLSON CENTER FOR IMAGING SCIENCE
COLLEGE OF SCIENCE
ROCHESTER INSTITUTE OF TECHNOLOGY
ROCHESTER, NEW YORK

CERTIFICATE OF APPROVAL

Ph.D. DEGREE DISSERTATION

The Ph.D. Degree Dissertation of *Surya Kamal* has been examined and approved by the dissertation committee as satisfactory for the dissertation requirement for the Ph.D. degree in Imaging Science.

Prof. Richard Hailstone, Advisor

Dr. Nathan Cahill, Committee Member

Dr. Roger Easton Jr., Committee Member

Dr. Benjamin Zwickl, External Chair

Date

Advancements in Scanning Electron Microscopy

by

Surya Kamal

Submitted to the Chester F. Carlson Center for Imaging Science in partial fulfillment of the requirements towards the Doctor of Philosophy Degree in Imaging Science at the Rochester Institute of Technology

Abstract

Scanning electron microscopes (SEM) are poorly characterized imaging instruments. The SEM optics (lens and aperture assembly) is designed to form a focused electron probe that scans the specimen to produce images. Therefore, the imaging efficacy in SEM strongly depends on the quality of the optics. However, there is no way to accurately characterize the optics in an uncorrected SEM (without multipole correctors) due to the lack of an exit wave. This work focuses on improving the imaging capabilities of an uncorrected SEM by understanding its optical performance using wave optical theory, simulation, and experiment. In this dissertation, we have developed two different simulations based on wave optical treatment of the electron beam to model the optical column and probe formation. Using one of the simulations for data generation, we have developed an aberration diagnostic method for the uncorrected SEM based on deep learning. Further, we have developed an experimental technique to perform non-interferometric phase retrieval of the electron probe. We have used the recovered phase information to visualize the point-spread function of the SEM optics (PSF_{optics}) for the first time. Finally, we have proposed an experiment based on electron vortex beams to improve phase retrieval. This work lays out the initial steps required to move towards "aberration-free" imaging in SEM without the use of multipole correctors.

Publications

Journal Articles

1. **Kamal, S.**, & Hailstone, R. (2022). 'SEM Nano: An Electron Wave Optical Simulation for the Scanning Electron Microscope'. *Microscopy and Microanalysis*, https://doi.org/10.1017/S1431927622000198

2. **Kamal, S.**, Zhou Y., & Gong, Z. (2024). 'Wave Optical Modeling of SEM Column From Source to Specimen'. *Microscopy and Microanalysis*, https://doi.org/10.1093/mam/ozae072

3. **Kamal, S.**, & Hailstone, R. (2024). 'Point Spread Function of the Optics in Scanning Electron Microscopes', https://arxiv.org/abs/2407.01439 (under peer-review)

4. **Kamal, S.**, Prajapati, H., Cahill, N., & Hailstone, R. (2024). 'Aberration Diagnostics Based on Deep Learning for the Uncorrected Scanning Electron Microscope', (to be submitted)

5. **Kamal, S.**, & Hailstone, R. (2024). 'Wave Optics of Scanning Electron Microscopes for Aberration Correction'., (to be submitted)

Conference Proceedings

1. **Kamal, S.**, & Hailstone, R. (2024). 'Visualizing the Point-Spread Function of the SEM Optics'. *Microscopy and Microanalysis*, https://doi.org/10.1093/mam/ozae044.320

2. **Kamal, S.**, & Hailstone, R. (2023). 'Electron Vortex Beam and Probe Phase in Scanning Electron Microscopy'. *Microscopy and Microanalysis*, Volume 29, Issue Supplement 1, Pages 487 - 488. https://doi.org/10.1093/micmic/ozad067.231

3. **Kamal, S.**, Prajapati, H., Cahill, N., & Hailstone, R. (2023). 'Probe Aberration Correction in Scanning Electron Microscopy using Artificial Neural Networks'. *Mi-*

croscopy and Microanalysis, Volume 29, Issue Supplement 1, Pages 739-740. https://doi.org/10.1093/micmic/ozad067.364

4. **Kamal, S.**, & Hailstone, R. (2023). 'Electron Probe Phase using Defocus in Scanning Electron Microscopy'. *Microscopy and Microanalysis*, , Volume 29, Issue Supplement 1, Pages 454-455. https://doi.org/10.1093/micmic/ozad067.213

5. **Kamal, S.**, & Hailstone, R. (2023). 'Need for Wavefront Sensing in Scanning Electron Microscopy'. *Microscopy and Microanalysis*, , Volume 29, Issue Supplement 1, Pages 491-492. https://doi.org/10.1093/micmic/ozad067.233.

6. **Kamal, S.**, & Hailstone, R. (2023). 'Quantum Wavefunction Reconstruction of Electron Beam in Scanning Electron Microscopy'. *Proc. SPIE 12447, Quantum Sensing, Imaging, and Precision Metrology, 124470R*; https://doi.org/10.1117/12.2647634

7. **Kamal, S.**, & Hailstone, R. (2021). 'Modeling SEM Column, Probe Formation, and Imaging Using Fourier Optics'. *Microscopy and Microanalysis*, 27(S1), 3336-3337. https://doi.org/10.1017/S1431927621011466

Acknowledgements

This dissertation would not have been possible if it wasn't for so many people. People who have been a support for me. First and foremost, I thank my academic advisor at RIT, *Prof. Richard Hailstone* for always being available and encouraging for our research discussions. Thank you for allowing me to have the freedom to pursue whatever I wanted to do. This work wouldn't have been possible if you didn't have my back through the difficult times in my life. I am indebted to two wonderful teachers; *Dr. Kedar Khare* (Indian Institute of Technology, Delhi, India) and *Dr. Chandrashekhar Garde* (Vishwakarma Institute of Information Technology, Pune, India) who pushed me toward Optics and Physics research. I also thank *Dr. Shriganesh Prabhu* (Tata Institute of Fundamental Research, Mumbai, India) for his support during my time in India. I would also like to thank *Dr. Roger Easton Jr.*, *Dr. Grover Swartzlander*, *Dr. Nathan Cahill*, and *Dr. Benjamin Zwickl* here at RIT for all the invaluable discussions. Special thanks to *Dr. Eric Lifshin* (SUNY, Albany) for starting the research that led to my inquiry into electron optics. I would like to acknowledge the contributions of my colleagues at *ASML, Inc.* (*Dr. Yongjian Zhou* and *Dr. Zizhou Gong*) to the work shown in Chapter 3. I would explicitly like to thank my friend and colleague *Harsh Prajapati* for working with me on Chapter 4 and all his contributions to the associated paper. The Center for Imaging Science at RIT has been a wonderful place for my growth and feels like my work family. I couldn't thank enough the amazing staff members especially *Cheryl Merell*, *Lori Hyde*, *Patty Lamb*, and *Dr. Karen Braun*, who have been so helpful to me. I sincerely thank all the great people I met along the way who were kind to me and helped me get where I am. The list is in chronological order of when I met them. *Dr. Nidhi, Girish Shinde, Siddhanth Shetty, Sheetal Chawla, Shelly Gupta, Reema Singhal, Rashida Mumin, Dr. Biswa Ranjan Swain, Dr. Kamal Rana, Harsh Prajapati, Kedar Patki, David Conran, Dr. Roshan Reddy, Dr. Prateek*

Srivastava, Dr. Lucy Chu, Faith Lambert, Ryan Crum, Ashwin Shukla, and, Amy Ross. I would like to thank *Faith* for being there for me when my health deteriorated. It meant a lot, so thank you. Furthermore, I want to acknowledge the contribution of my family. My sister *Divya Jamuar* for loving and accepting me unconditionally and my parents (*Manoj Kumar and Archana*) for sacrificing their needs to put mine ahead. I wouldn't be here if it wasn't for your efforts in providing me with the best you could do. Last but not least, a big thank you to *my doctors* and *therapists* who provided me with the support that I needed to go through the physical and mental health challenges during my PhD.

And of course, Misa!

Dedicated to....

'The humbling journey of starting to witness the extent of my ignorance'

I only know one thing, and that is I know nothing

- Socrates

Contents

List of Figures

List of Tables

Chapter 1

Introduction

1.1 SEM Story

Electron microscopes have been at the forefront of new scientific discoveries for almost a century now. Since the birth of quantum theory, it was theorized that electrons as an illumination source would produce far superior resolution compared to optical microscopes because of their smaller wavelengths. Both the transmission electron microscope (TEM) and the scanning electron microscope (SEM) were invented in the $1930s$. Since then, it was a dream for physicists to be able to see individual atoms under these powerful microscopes. However, there were too many bottlenecks that made it extremely challenging. Extremely aberrated optics, lack of nanometer-size electron gun tips, and poor mechanical and electrical stability were some of the main challenges. In the $1970s$, with the development of the cold field-emission gun (FEG) [10], imaging single atoms of heavy metals was finally demonstrated using a scanning transmission electron microscope (STEM) [11]. After decades of research in aberration correction, achieving $0.1\ nm$ resolution and therefore having the ability to see individual atoms became routinely possible for aberration-corrected TEM and STEM imaging [12, 13, 14]. However, it remained elusive in SEM for a long time. Throughout the 20^{th} century, SEM has

never been regarded as the cutting-edge of imaging resolution. It was only in 2009 that imaging single atoms was demonstrated using secondary electrons [15]. This was the first time that SEM could achieve a comparable resolution ($0.1 - 0.15\ nm$) to that of a TEM and STEM [15, 16].

In more than nine decades of its development, SEM has become an invaluable imaging instrument. Its ability to offer surface and sub-surface specific information coupled with relatively easier sample preparation compared to the TEM and STEM makes it a robust choice for many applications like material characterization, semiconductor device inspection, microchip assembly, geological sampling, forensic analysis, biomedical sciences, electron beam lithography, etc [17, 18, 19, 20, 21, 22, 23]. Despite its prowess as an imaging modality, the performance of the uncorrected SEM is orders of magnitude poorer compared to its theoretical limits. Although there are numerous factors like noise, charging, and deflection fields that affect its practical resolution; aberrations are the primary deteriorating factor [24].

In 1936, Scherzer proved that rotationally symmetric electron lenses suffer from positive chromatic and spherical aberration [25]. This started a quest for aberration correction in electron optics and after almost six decades of research, chromatic and spherical aberration correction was shown in low voltage SEM [26, 27]. This was a breakthrough in electron optics and *Zach et al.* [26, 27] were able to achieve a practical resolution of $< 2\ nm$ at a beam energy of $E = 1\ keV$ by implementing the multipole corrector design proposed by Rose [28]. Since then other aberration-corrected SEMs have been developed [29]. However, most of the research in SEM aberration correction has been focused on automating the aberration correction process [30, 29, 31] and improving the existing correctors.

Aberration diagnostics are a precursor to accurate aberration correction. For transmission electron microscope (TEM) and scanning transmission electron microscope

(STEM), the exit wave is imaged onto a pixelated detector. Hence, techniques for aberration diagnostics using ronchigrams and diffractograms are well established [32, 33]. In an SEM, as the focused electron probe scans the specimen, the beam information is lost. Therefore, no standardized aberration quantification methods exist for the SEM. The aberration correction reported by *Zach et al.* [26, 27] uses aberration contributions to the aberration eikonal which are theoretical estimates, it does not perform actual aberration sensing. In this implementation, the next development was to find linearity between the field strength and aberration coefficients by using approximate probe intensity [31] from SEM images to better estimate the aberrations and automate the correction. Researchers have also demonstrated aberration quantification using a STEM camera [34]. We would like to point out that currently most commercially available aberration correctors for SEM are still based on the original implementation [26, 27] with some upgrades and quantifying aberrations in an uncorrected SEM remains an unsolved problem.

Most of the research in aberration correction has been centered on perfecting the electron optics [35]. The idea is to combine the multipole elements with the lens field to mitigate the effect of lower-order aberrations as they limit the resolution. Although efficacious, multipole aberration correctors have some inherent drawbacks. They have to be controlled and tuned with extreme precision, the resolution is still limited by the higher order residual aberrations and most importantly, they are very expensive [36]. In many cases, the base aberration correctors are much more costly than the SEM itself! Over time there have been numerous designs proposed for aberration correction namely foil correctors [37], electron mirrors [38], electrostatic correctors [39, 40, 41], etc. but they are all still focused on correcting the optics.

Another approach to aberration correction is accepting the imperfections in the optics and adding a reconstruction step to correct the final output (ex: holography).

Motivated by the recent developments in dynamic electron beam shaping [42, 43, 44, 45, 46, 47] and the need for more efficient and accessible ways for aberration correction, in this dissertation we propose wavefront-sensing-based aberration correction in SEM [48, 49, 50]. Instead of tuning the multipole correctors to correct for individual aberrations, the idea is to have an accurate measurement of the aberrated wavefront itself to negate all aberrations and in principle form "aberration-free" probes.

1.2 Basics of SEM

What is an SEM?

An SEM is an ensemble of two sub-imaging systems: the probe-forming lenses and the beam-sample interaction. The interaction produces a variety of signals which are recorded by their corresponding detectors to generate outputs such as an image, X-ray map, spectrogram, etc. A general schematic diagram of an SEM is shown below in Figure 1.1. The purpose of the magnetic lenses is to form the smallest possible scanning probe by demagnifiying the spatial intensity distribution of electrons coming from the source. In general, multiple lenses (condenser, intermediate, objective) are required for this job. However, in the case of field-emission guns, the virtual source size already is of the order of $nm's$. So despite having multiple lenses, the probe formation is mainly done by the objective lens. There are apertures like the spray aperture and the final aperture whose primary job is to remove the off-axis electrons to make the beam narrow and coherent. When the beam scans the sample a whole range of electrons, photons, plasmons, etc. are released as shown in Figure 1.2. Each one of them carries different information about the sample and is sensed using a unique detector.

The commonly imaged electrons are the secondary electrons (SE) and backscattered electrons (BSE). SEs are electrons that can be released from different orbitals of the

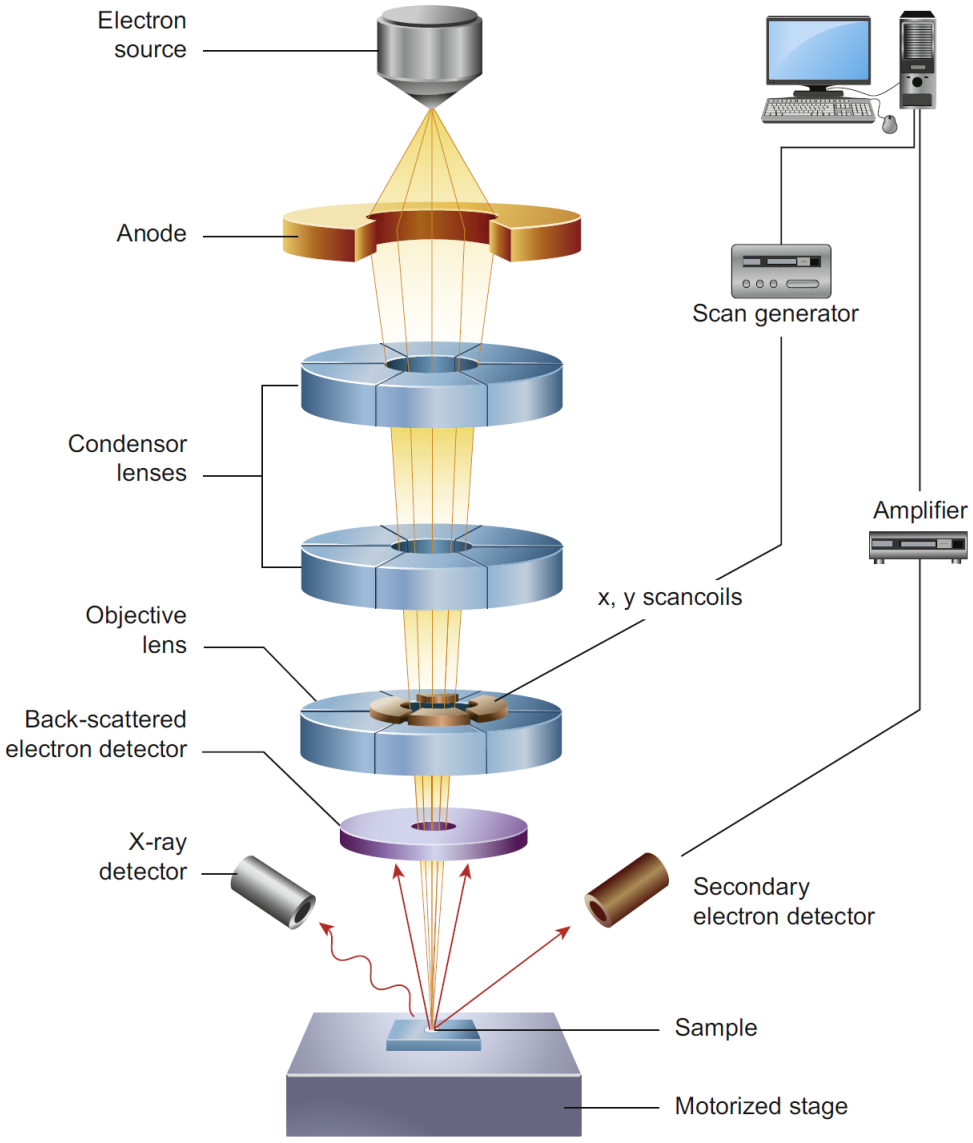

Figure 1.1: Schematic diagram of a scanning electron microscope [1]

atoms in the sample after they are removed by beam electrons and have energy $E \leq 50eV$. If they have enough energy, they can overcome the work function potential of the sample and escape into the SEM chamber to be sensed by the Everhart-Thornley (ET) detector. Generally, SEs come from within 5-50 nm of the sample surface. The ET detector has a $(+200V)$ voltage on a Faraday cage to attract the electrons and then a scintillator followed by a photomultiplier tube which amplifies the signal to record a gray level value coming from a single object pixel. BSEs are beam electrons having energy E $\gg 50eV$, which interact approximately elastically with the nuclei in the sample and are scattered back toward the sample surface. These are sensed by an annular ring detector placed just below the objective lens on the optical axis. BSEs can come from well below the surface of the material and provide information about both the topography and composition of the sample.

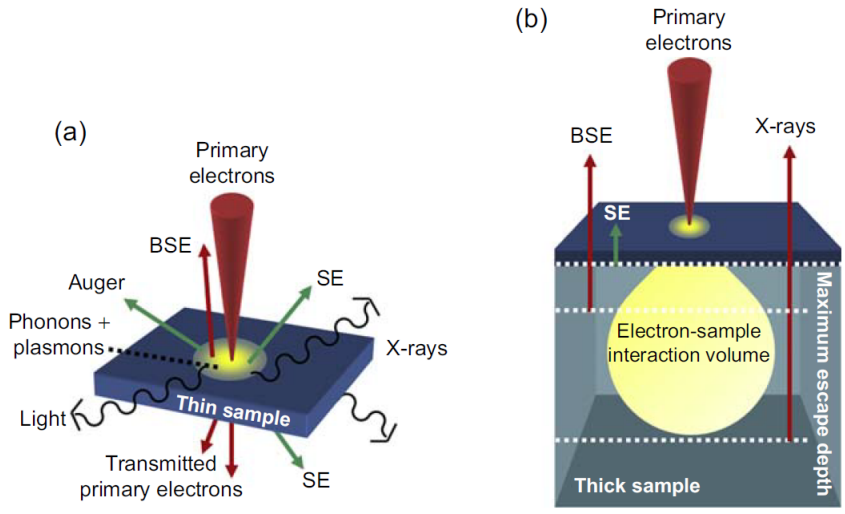

Figure 1.2: (a) Electron-matter interaction and various signals generated in SEM, (b) Interaction volume and signals from various depths in the sample. [1]

Electron sources

Electron guns are crucial to the performance of SEMs. One type of electron gun is favored over the other depending on the application. They are broadly of two types: thermionic (tungsten, Lanthanum hexaboride, or LaB6) and field emission (Schottky and cold field emission). In our work, we will consider only field emission SEMs where the virtual source size (spatial intensity distribution of the beam at the source) is already < 30 *nm*. Therefore, they use only the objective lens for beam demagnification and probe formation. The coherence of the electron source plays a huge role in the achievable resolution and final image quality. In general field emission guns have high spatial and temporal coherence compared to tungsten or LaB6.

Magnetic Lenses

SEM lenses are not made of glass as any material will interact with the electrons. Therefore, as the electrons are charged particles, their trajectory can be manipulated by a magnetic field. Lenses for electrons are constructed with ferromagnetic materials and wound with copper wire. These lenses produce a focal length that can be changed by varying the current through the coil. The magnetic field bends electron paths which can be described using the Lorentz force and classical electrodynamics.

Final image formation

The image displayed on the monitor using an SEM has a 1-to-1 correspondence between a sample pixel and an image pixel. A fraction of the electrons of a specific range of energy generated by the interaction when the beam is parked at a particular location are collected by the detector. They are then converted into a voltage value and then quantized on a grayscale as pixel intensities by the image acquisition system. The actual

processing is much more detailed and Figure 1.3 shows a simplified view of the process. In an SEM, the image is generated pixel-by-pixel by focusing an electron beam to a

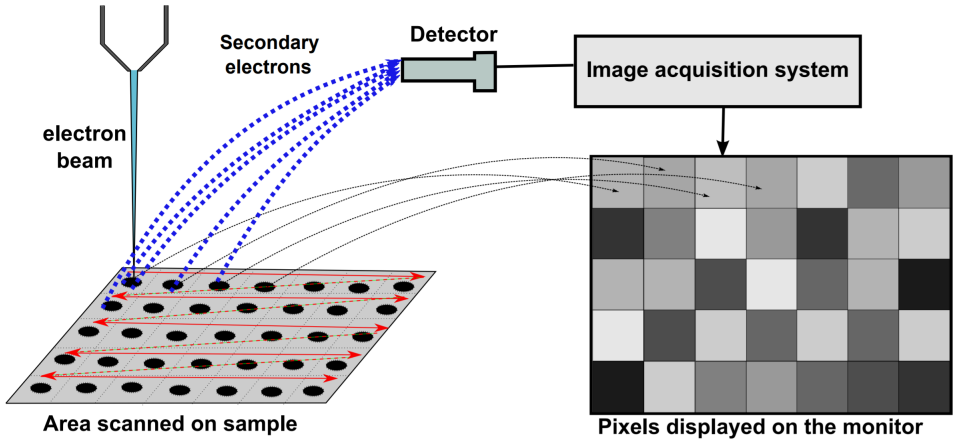

Figure 1.3: Image formation process in SEM. [2]

small area (determined by the demaginification) on a bulk sample and then rastering the beam over the sample. Magnification is determined by the ratio of the distance scanned on the display to the distance scanned on the sample (e.g., scanning a smaller area results in a larger magnification, if the display size is constant). However, the useful magnification is limited by the minimum electron probe size. As magnification is increased, eventually the step size between pixels will be smaller than the diameter of the electron probe.

Point spread function (PSF)

The PSF of a linear shift-invariant (LSI) imaging system describes how the image of a point source is changed by the system. If the imaging system were perfect, the image would be an exact representation of the point source being imaged. In reality, the image of the point source is altered by imperfect optics, mirrors, or other aspects of image formation for a particular system. The imperfections are captured in the PSF. Knowledge of the PSF can be utilized to improve the quality of the output image

using different deconvolution algorithms. In general, an inverse filter is designed using the PSF to approximately reverse the blur caused by the PSF during forward imaging described in Equation 1.2.1. An image can be described as the convolution of an imaging

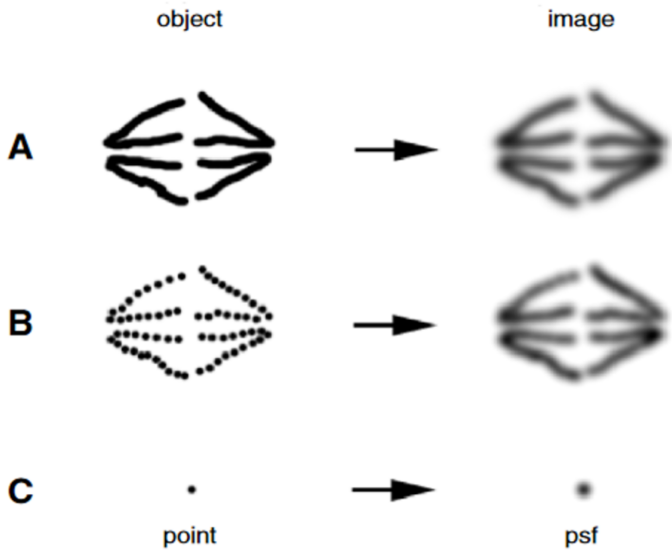

Figure 1.4: Visualization of a PSF and its effect on images. The ideal image of an object is shown in the left column. The output of the imaging system is shown in the right column. When a point source is imaged (C), the output image is the PSF. The output images of (A) and (B) are the convolutions of the true image and the PSF. [3]

system's PSF and the scene being imaged. The convolution is given by the following equation:

$$\mathcal{I}_{real}[x,y] = \mathcal{I}_{ideal}[x,y] \otimes h[x,y] + \eta[x,y] \tag{1.2.1}$$

where $\otimes$ is the convolution operator, $\mathcal{I}_{ideal}[x,y]$ is the ideal image of the scene, $h[x,y]$ is the PSF, $\eta[x,y]$ is the noise, and $\mathcal{I}_{real}[x,y]$ is the output image of the scene. A visualization of this process can be seen in Figure 1.4. These variables are given as a function of pixel coordinate location $[x,y]$. It is important to note that this is a lax description of a PSF. A more rigorous discussion of PSF includes the degree of coherence and its effects, which is provided in Chapter 2.

1.3 Imaging chain of the SEM

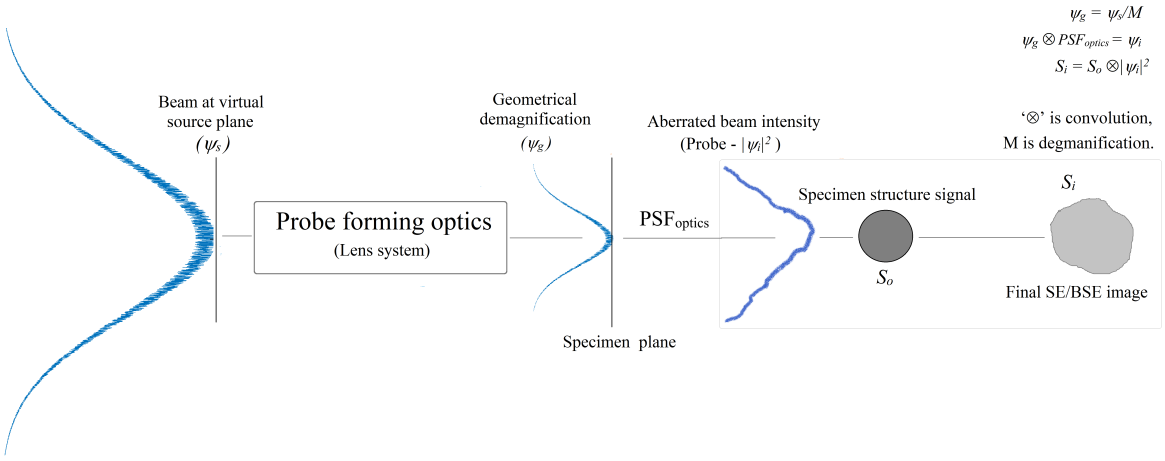

Figure 1.5: Imaging chain of an SEM [4]. A Gaussian beam at the virtual source plane is minimized by the probe-forming optics which interacts with the specimen to produce image signal.

As mentioned above, an SEM consists of two imaging systems; the probe-forming lenses and the beam-specimen interaction. An ideal lens system which forms the probe, is expected to just demagnify the probe. However, in practice, all lens systems introduce diffraction through multiple apertures and aberrations through multiple lenses. Therefore, at the specimen, the geometrical image of the beam (ψ_g) is convolved with the coherent point spread function (PSF$_{optics}$) to produce an aberrated beam as shown in Figure 1.5.

As the beam impacts the specimen, its phase is lost and the aberrated intensity ($|\psi_i|^2$) is convolved with the specimen structure signal (S_o) to produce the final image (S_i). This final image can be a SE or a BSE signal. S_o [51] refers to the signal generated by the electron-matter interaction when the beam was an ideal delta function beam ($\delta(x, y)$). It is interesting to notice in Figure 1.5, that we show S_i has been blurred, deformed, and has less contrast than the ideal signal S_o. The whole imaging chain can

be summarized in the equations below (ignoring noise for now):

$$\psi_i = \psi_g \otimes PSF_{optics} \tag{1.3.2}$$

$$S_i = S_o \otimes |\psi_i|^2 \tag{1.3.3}$$

where $\otimes$ shows convolution. As the aberrated beam intensity $|\psi_i|^2$ blurs the specimen structure signal S_o it is often referred to as the PSF for the SEM [51] and has been an interest of recent research [52, 6, 53, 54]. The squared modulus in Equation 1.3.3 indicates that we lose the phase and only the beam intensity is used for imaging the specimen. The whole imaging chain is explained in detail later in 2.

Probe Width in an SEM

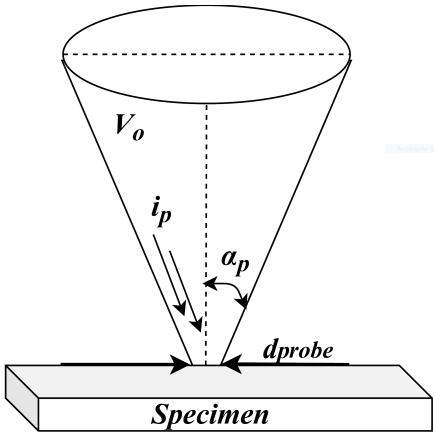

Figure 1.6: Probe parameters in a SEM

The geometrical picture of probe diameter calculation is dependent on the geometrical (Gaussian) image of the probe, diffraction, spherical, and chromatic aberrations. In practice, the PSF of an SEM (probe intensity) is often characterized using a single number; the probe diameter. An approximation of probe width can be found by using

the following expression:

$$d_{probe}^2 = d_{gaussian}^2 + d_{diffraction}^2 + d_{spher.\ aberr}^2 + d_{chrom.\ aberr}^2 \tag{1.3.4}$$

where d_{probe} is the effective probe width, $d_{diffraction}$ is the beam width (Full-width-at-half-max - FWHM) of the Airy disc corresponding to the diffraction limit, $d_{spher.\ aberr}$ is the size of the disk of least confusion caused by spherical aberration, $d_{chrom.\ aberr}$ is the size of the disk of least confusion due to chromatic aberration (more severe at low voltages), and $d_{gaussian}$ is the minimum Gaussian focus of the beam. Values of these parameters are dependent on the beam voltage (V_o), beam convergence angle (α_p), and probe current (i_p) which are shown in Figure 1.6 and the coefficients of aberrations. Often their contributions are added in quadrature as shown in equation 1.3.4, which is inconsistent as the relationship between the probe width and the probe current is ill-defined [55]. Another way of representing the probe width is to use the d_{59} value [56] which is 59% of the total probe intensity within the diameter d. A more accurate way is using the root power sum (RPS) method [55] shown in the equation 1.3.5 which uses only $FW50$ (full-width at 50% current value) diameters.

$$d_{probe}^2 = ((d_{diffraction}^4 + d_{spher.\ aberr}^4)^{\frac{1.3}{4}} + d_I^{1.3})^{\frac{2}{1.3}} + d_{chrom.\ aberr}^2 \tag{1.3.5}$$

Although these methods provide a reasonable account of the probe width, they are not enough. As we push the limits of resolution on the SEM, any minute features in the probe distribution will become relevant. Therefore, reducing the performance of an SEM to a probe width is unrealistic and simplistic. An accurate characterization of any optical system is pivotal to understanding and improving its performance. Therefore it becomes important to fully characterize the probe distribution (intensity and phase), which is one of the main focuses of this dissertation.

1.4 Probe Intensity Determination

As mentioned above, the probe information is lost in the process of imaging in an SEM. Many techniques exist for probe intensity determination/calculation [52, 6, 53, 54, 57]. We use the method proposed by Lifshin *et al.* [58] and Zotta, Nevins *et al.* [6] for reconstructing the probe intensity $|\psi_i|^2$. To calculate $|\psi_i|^2$, we solve the inverse problem in Equation 1.3.3. The experiments were done on a TESCAN MIRA3 SEM equipped with a Schottky field-emission source (virtual source size; $d_s = 20\ nm$) at a voltage of $V = 20\ kV$. The process begins by capturing secondary electron (SE) or back-scattered electron (BSE) images of well dispersed 28.5 nm gold (Au) nanoparticles (NPs) on a thin ($\sim 20\ nm$) carbon (C) film in a field-of-view (FOV) of 2048 $\mu m \times 2048\ \mu m$. Then all the individual NPs in the FOV are segmented and stacked together to get a high signal-to-noise ratio and generate a realistic image of a single NP ($S_i/\mathcal{I}_{real}$). Following that, an ideal image/object structure ($S_o/\mathcal{I}_{ideal}$) is generated using the Monte-Carlo simulation CASINO [59], based on the material composition, size, and shape of the object and ideal imaging conditions. The probe intensity is known to blur the object structure to produce a real image in the SEM $S_i = S_o \otimes |\psi_i|^2$ (See equation 1.3.3). Therefore, a simple Wiener-filter-based deconvolution shown in the last step of table 1.1 yields the probe intensity distribution ($\widetilde{psf} = |\psi_i|^2$). This is described in detail in section 2.2.6

1.5 Dissertation Overview

The work presented in this dissertation aims to lay a foundational ground based on the wave optical theory, simulation, and experiment that is required to take the initial steps towards "aberration-free" imaging in SEM without the use of multipole correctors.

Broadly the dissertation can be divided into two parts: (1) Representation of the

Step #	Mathematical description	Physical description
1	$\psi_g = (1/M)\psi_s$	Beam demagnification
2	$\psi_i = \psi_g \otimes PSF_{optics} = \sqrt{\psi_i}\, e^{i\phi_{true}}$	Aberrations introduced
3	$\lvert\psi_i\rvert^2 = \lvert\psi_g \otimes PSF_{optics}\rvert^2$	True phase lost
4	$S_i(x,y) = \lvert\psi_i\rvert^2 \otimes S_o(x_i, y_i)$	BSE or SE image signal
5	$S_i(x,y) = S_o(x,y) \otimes psf(x,y) + \eta(x,y)$	Noise added
6	$\widehat{S_I(f_x,f_y)} = \widehat{S_O(f_x,f_y)} \cdot OTF(f_x,f_y) + N(f_x,f_y)$	Fourier space representation
7	$\widetilde{psf} = F^{-1}\left[\left(\frac{\widehat{S_O}^*}{\lvert\widehat{S_O}\rvert^2+K}\right) \cdot \widehat{S_I}\right]$	Reconstruction of probe

Table 1.1: Summarizing the final probe formation, and imaging using the final probe in a step-wise description

SEM optics using wave optical methods and (2) its applications (probe phase retrieval, aberration diagnostics, and correction). The rest of the dissertation is arranged as follows: representation of the SEM column and probe formation using wave optical models (Chapter 2 and Chapter 3), developing an aberration diagnostic method for the SEM using deep learning (Chapter 4), experimental results of the phase retrieval of the electron probe using multiple probe intensities (Chapter 5), suggesting a technique to improve phase retrieval (Chapter 6), outlining the adaptive optics pipeline for aberration correction in SEM (Chapter 7), and finally a conclusion (Chapter 8) to tie everything together.

Chapter 2

SEM Optics - Wave Optical Model I

2.1 Background

The resolution of an SEM is theoretically limited by the electron probe which scans the specimen for imaging. In practice, there are multiple other factors [51] such as noise, specimen damage, charging, beam deflection blurring [60], etc. which further deteriorate resolution. In this chapter, we focus on probe formation and its effects on resolution in a field-emission SEM using a point-spread function-based imaging model. Field-emission guns (FEG) compared to thermionic guns (tungsten, LaB6) have high spatial and temporal coherence. The high spatial coherence can be attributed to the fact that the FEGs form a virtual image ($< 20\ nm$) of the source just below the tip of the gun. In our simulations Beam width/probe diameter/virtual source size (d_s) refers to ~ 0.4 times the full-width-at-half-max (FWHM) value.

High temporal coherence is related to the monochromaticity of the electron beam. FEGs have a relatively small spread in the energy of beam electrons ΔE as compared to thermionic guns which ensure high temporal coherence. It has been shown by theoretical modeling and experiments that the current density distribution at the electron gun is Gaussian [61, 62]. This holds for all electron guns [63, 64]. For instantaneous time,

this implies that the charge density (spatial intensity distribution of electrons) is also Gaussian.

The lens system in a SEM, which forms the electron probe, images the electron probe at the source and demagnifies it at the specimen thereby manipulating the spatial distribution of electrons. Older systems with thermionic guns have an initial beam width of the order of $\mu m's$ and therefore the condenser lenses are required in successive demagnification at all the beam crossovers. Although there are multiple lenses in the SEM column, for FEGs (Schottky, cold FEGs) the demagnification is performed mainly by the probe forming objective lens [65]. In the case of FEGs, the condenser lenses might be used to control the formation of cross-over points away or near the final aperture diaphragm, thus controlling the number of electrons passing through the aperture. For instance, the TESCAN MIRA3 SEM with a Schottky gun has intermediate lenses, but they are turned off in the resolution mode.

In quantum mechanics, the wave nature of matter is exhibited by the wave function ψ describing a system that satisfies Schrödinger's wave equation. In electron microscopes, $|\psi|^2$ is the probability density of the electron beam where the wave function ψ describes the electron beam as a function of space-time. We cannot measure ψ directly, instead, we can measure the physical properties like current, intensity, and momentum which can be described using the modulus squared - $|\psi|^2$. This means that the wave properties like superposition and interference can be applied only to the wave function ψ but not to their observable physical properties described by $|\psi|^2$.

There exists a very close analogy [66] between the description of imaging systems based on light optics and on electron optics. In electrodynamics, there is a flow of charge, and in quantum mechanics, there is a flow of probability density. This implies that the probability density is analogous to charge density and the current density is analogous to the probability of current density. The charge density of the beam is

Gaussian and we apply wave optics to the wave function ψ of the electron beam.

In recent years, research related to coherent manipulation of electron beams [67, 68] has become a growing field in the electron microscopy community. The idea is that free-space paraxial electrons obey a wave equation which is similar to the Helmholtz equation for wave dynamics in light optics. Therefore, we can apply the theory of Fourier optics to electron beams. Some of its recent applications are electron vortex beam generation [69], beam manipulation in any arbitrary shape [67], etc. However, these advances are primarily limited to transmission electron microscopes (TEM) and scanning transmission electron microscopes (STEM) with some very recent developments for the SEM [70].

Electron probes in probe-forming systems have been studied extensively using both geometrical and wave optics [65]. Exact and approximate theoretical calculations of the probe size, analytical solutions, probe current and practical brightness of the probe, the root-power-sum algorithm to calculate the probe diameter, and evaluation of the effect of the probe on the imaging performance of an SEM are some of the important advancements in the field [71, 72, 55, 73]. In practice, the electron probe width has a contribution from the probe brightness and can be broadened further by the effects of diffraction, aberrations, and coherence of the source. All of these studies talk about the probe size and the probe diameter which implies that the probe distribution is always circularly symmetric. Although modern electron microscopes with aberration correctors and astigmators have a good capability of keeping the probe symmetric, this is not always the case. The probe can suffer other aberrations which not only affect the size of the probe but its shape too and can make it asymmetric. This was recently demonstrated for astigmatism [74] in an electron probe for SEM. Wave optical modeling has been used for both STEM [75] and for SEM [65, 70] to explain probe formation.

However, none of these studies provide a practical tool for a microscopist to pic-

ture the electron probe under different scenarios. Image and probe simulation tools [76, 77, 78] have been quite beneficial for the electron microscopy community. A dedicated program for SEMs to visualize the effect of aberrations, coherence, and noise in combination with different operating conditions of the SEM would be perceptive. It is crucial to mention here that we do not model the beam-specimen interaction in our program. Although the implementation might be used to predict the behavior of other probe-forming systems like STEM and Focused Ion Beam (FIB), we insist it is designed for the SEM.

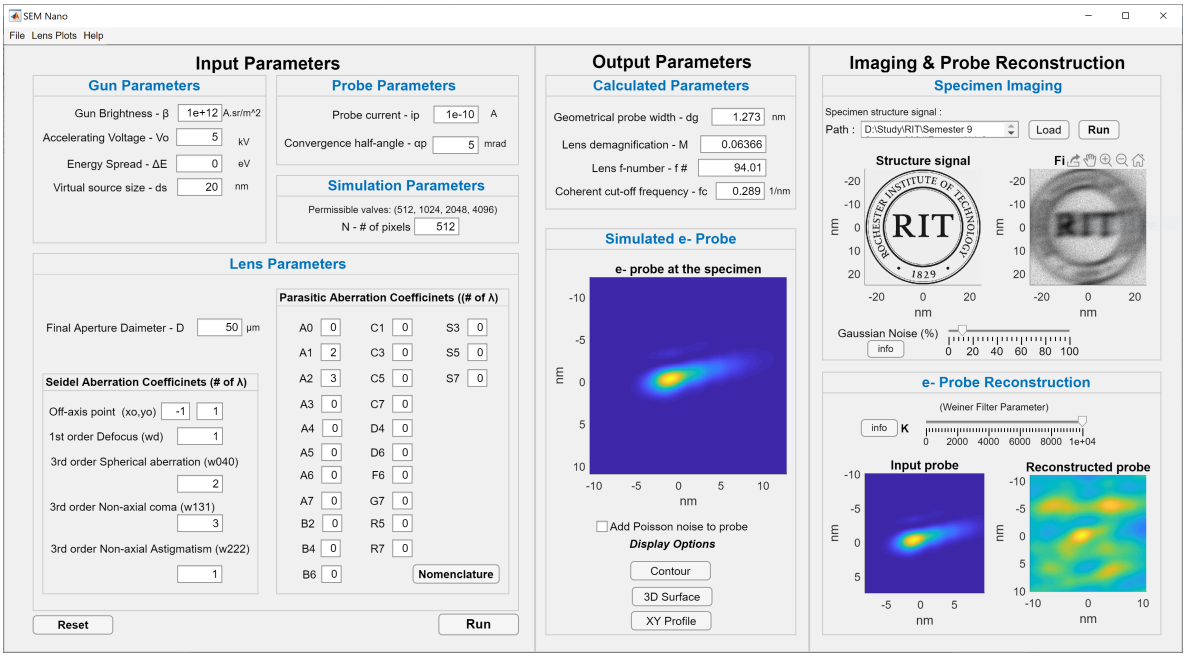

Figure 2.1: GUI for SEM Nano simulation program

Therefore, intending to apply the concepts of Fourier optics in SEMs, in this chapter we show the modeling, visualization, and reconstruction of the electron probe in field-emission SEMs using a point-spread function (PSF) model. We provide a detailed discussion about our simulation program '*SEM Nano*', with some results and its limitations. The software is focused on describing probe formation, and its reconstruction, given the structure signal (S_o). The graphical user interface (GUI) is designed in a sim-

ple layout shown in Figure 2.1. The user provides input parameters in Section 1 (Input Parameters) and the program calculates the shapes of the probe using electron wave optics in the 2^{nd} section (Output Parameters). In the 3^{rd} section (Imaging & Probe Reconstruction) this probe is used to image a specimen (simulated signal) and generate the final image. Noise can be added to the image and a Wiener-filter deconvolution can be done to reconstruct the electron probe.

2.2 SEM Nano - Point-spread function based model

This is the starting point for our implementation, where we consider the probability density of the beam at the gun to follow a Gaussian distribution whose width is defined by the virtual source size. The virtual source size of a gun is generally specified by the type of electron gun. Our discussion is focused on TESCAN MIRA3 SEM with a Schottky gun that uses a Denka TFE (thermal field emission gun) with an actual radius of 0.52 μm and a virtual source size of 20 nm. We also know from the instrument manual that while while imaging in resolution mode, the intermediate lenses are turned off and the condenser lens is used to control the beam crossover formation distance before the final aperture. The lens primarily responsible for source demagnification and probe formation is the objective lens.

Optical Setup

The electron beam wave function is described as

$$\psi_s(r_\perp, z) = \zeta(r_\perp, z) e^{i\phi(r_\perp, z)} \tag{2.2.1}$$

where amplitude function squared $\zeta(r_\perp, z)^2 = |\psi(r_\perp, z)|^2$ is Gaussian and can be written as $\zeta(r_\perp, z)^2 = |\psi(r_\perp, z = z_n)|^2 = e^{-(r_\perp/d_s)^2}$, where $r_\perp = (x, y)$ corresponds to the

transverse coordinates, z is the direction of the beam propagation, $z = z_n$ is a plane perpendicular to the $z - axis$ and d_s is the virtual source size, i.e., the electron beam width in the object plane $z = z_1$ in Figure 2.2. The beam width at the crossover just

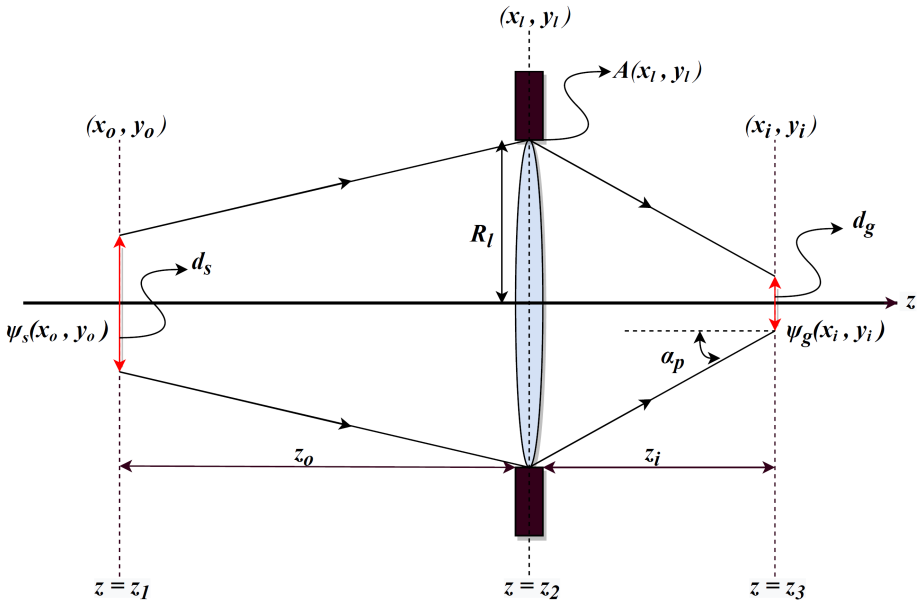

Figure 2.2: Optical Setup for field-emission SEM using only the objective lens for beam demagnification and probe formation.

before the objective lens is assumed to be the same as the beam width at the gun as the condenser lenses are not directly used for successive demagnification in FEGs. We use scalar diffraction theory to perform coherent diffraction-limited imaging of the electron beam by calculating the objective lens and imaging parameters from known information provided by the user.

2.2.1 Input Parameters

Gun Brightness, $\beta(A/sr \cdot m^2)$

Brightness is defined as the current density per unit solid angle at the emission source, which directly affects the emission current. Theoretically, if we have a bright source, we have more probe current which improves the final image quality. For our simulations

we use typical brightness values $\approx 10^{11}$ for Schottky guns and 10^{12} to 10^{13} for cold FEG [79].

Accelerating voltage, $V_o(volts)$

This is the extracting voltage applied to accelerate the electrons within the gun and provide them enough energy to overcome the metal work-function and escape into the column vacuum. It determines the kinetic energy of the electrons and thus directly affects the de Broglie wavelength λ associated with the beam electrons. We use values from $0.1keV$ to $30keV$ in our simulations. During our simulation experiments we found that for energies $> 15keV$, wave effects in probe formation are minimal.

Energy spread in the gun, $\Delta E(eV)$

There is a small spread in the emission energy associated with the gun which affects temporal coherence. In the case of cold FEG, the energy spread is around $0.2 - 0.3eV$ and it is $0.3 - 0.8eV$ for Schottky guns. Temporal coherence length $l_c^{temporal} = v_e h/\Delta E$, where v_e is the velocity of electrons and h is Planck's constant. For coherent imaging and coherent aberrations, we assume $\Delta E = 0$ in our simulations. In the case of partial coherence, typical values of $\Delta E \approx 0.2 - 0.8eV$ are used.

Virtual source size, $d_s(nm)$

The field just below the Wehnelt cap (electrode in the gun assembly) acts as a converging lens and forms a virtual image of the source in FEGs. This is the virtual source size which ensures very high spatial coherence. For Schottky guns, it is $10 - 20nm$ in width and $3 - 5nm$ for cold FEG. In our simulations, we use $d_s = 20nm$. An indicative measure of high spatial coherence is achieved when effective source size $d_s << \lambda/2\alpha_p$, where α_p is the half convergence angle in Figure 2.2. For a typical setup of values

$E = 20KeV \rightarrow \lambda \approx 8.5885\ pm, \alpha_p = 5\ mrad,\ and\ d_s = 20\ nm,\ \lambda/2\alpha_p \approx 85.885\ nm$ that is ~ 4 times greater than d_s. This indicates high spatial coherence.

Aberration coefficients

In this chapter, aberration coefficients are the weights of an aberration in terms of the number of wavelengths (λ) of error from the ideal wavefront. We are going to incorporate three types of aberrations in our program which are Seidel, parasitic, and incoherent aberrations. Later in Chapter 4, we have used a normalized representation where the aberration coefficients are not the number of wavelengths.

Probe current, $i_p(A)$

In practice, the probe current affects the visibility of the final image as it affects the signal-to-noise ratio (SNR). A higher probe current means more contrast in the image. Probe current also affects the geometrical size of the probe; a higher probe current makes the probe larger and hence reduces the highest achievable resolution. Typically for our simulations, we use a value of 10^{-11} to $10^{-12} amps$.

Half-convergence angle, $\alpha_p(radians)$ and final aperture diameter, $D(\mu m)$

The convergence angle determines the depth of focus in the image. It also is a factor which is inversely proportional to the geometrical probe size. The smaller the convergence angle, the larger the probe size and hence the lower the resolution. However, if we want a higher depth of focus, a smaller α_p serves the purpose. We use typical values of $5 - 20 mrad$ for α_p in our simulation. The values of α_p define the ratio of $D/2z_i$.

The final aperture diameter is used to trim the final beam which enters the objective lens. In terms of Fourier optics, it imposes a maximum limit on the frequencies that contribute to the image formation of the beam through the objective in the image plane $z = z_3$ described in Figure 2.2. Practical values of D are in $\mu m's$. For instance,

the TESCAN VEGA3 SEM has a final aperture diameter of $50\mu m$. However, in our simulations we don't change the value of D, instead we change α_p.

2.2.2 Output parameters

Using the brightness equation [65], we find the width d_g of the geometrical probe at the specimen. This is the ideal probe which is just the geometrical demagnification of the electron probe at the source without any diffraction or aberrations and is calculated by the equation:

$$d_g = \sqrt{\frac{(4i_p)}{(\beta\pi^2\alpha_p^2)}} \tag{2.2.2}$$

This is the width of the geometrical image of the probe in the image plane $z = z_3$ in Figure 2.2.

Once we have the width of the electron probe before and after demagnification, we can calculate the magnification $M = d_g/d_s$. Since we have the half-convergence angle α_p and the final aperture diameter D, we can calculate the image distance, $z_i = R_l/\alpha_p$ where $R_l = D/2$ is the radius of the aperture. Now, using the magnification M and image distance we find the object distance from the aperture, $z_o = z_i/M$. Then z_i and z_o are used to find the focal length of the lens by the lens formula, $1/f = 1/z_o + 1/z_i$. To define the action of the lens in the Fourier domain, we find the cut-off frequency of the aperture which is $f_c = \alpha_p/\lambda$ (small angle or paraxial approximation). The relativistic wavelength of the electrons, λ_{rel} is calculated using the equation:

$$\lambda_{rel} = \frac{hc}{\sqrt{2eV_o m_e c^2 + (eV_o)^2}} \tag{2.2.3}$$

where h is Planck's constant, c is the speed of light in vacuum, m_e is the rest mass of an electron, e is the charge of an electron and V_o is the accelerating voltage provided by the user. For voltages used in an SEM ($E = 0.5 - 20; keV$), relativistic effects are

negligible but we have used it for the sake of completeness.

2.2.3 Coherent imaging of the electron beam

The image formation of the probe in plane $z = z_3$ can be explained by defining the point-spread function (PSF) of the optics/lens system. We are restricting our discussion here only to coherent imaging of the beam for now. As FEGs have very high coherence, the effects of partial coherence are not central to this discussion. The coherent PSF [80, 81] of the lens system (PSF_{optics}) is the Fourier transform of the aperture function $A(x_l, y_l)$:

$$\begin{aligned} PSF_{optics} = h(x_i, y_i) = F[A(x_l, y_l)] \\ = \int_{-\infty}^{\infty}\int_{-\infty}^{\infty} A(x_l, y_l) exp[\frac{-i2\pi}{\lambda}(x_i x_l + y_i y_l)]dx_l dy_l \end{aligned} \tag{2.2.4}$$

where (x_l, y_l) is the lens plane ($z = z_2$) coordinate system, (x_i, y_i) is the image plane ($z = z_3$) coordinate system. The wave function in the image plane is calculated by the convolution of the PSF_{optics} and the geometrical wave function.

$$\begin{aligned} \psi_i(x_i, y_i) = \psi_g(x_i, y_i) \otimes h(x_i, y_i) \\ = \int_{-\infty}^{\infty}\int_{-\infty}^{\infty} \psi_g(x'_i, y'_i) h(x_i - x'_i, y_i - y'_i) dx'_i dy'_i \end{aligned} \tag{2.2.5}$$

where, $\psi_g(x_i, y_i) = (1/|M|)\psi_s(x_i/M, y_i/M)$ [80, 81, 9].

It is important to note that the PSF for incoherent imaging can be obtained by simply squaring the modulus of the coherent response, i.e. $|PSF_{optics}|^2 = |h(x_i, y_i)|^2$ and the incoherent imaging of the beam [80, 81] can be expressed as

$$|\psi_i(x_i, y_i)|^2 = |\psi_g(x_i, y_i)|^2 \otimes |h(x_i, y_i)|^2 \tag{2.2.6}$$

However, for FEGs, high coherence of the electron source ensures that the imaging of

the probe is never completely incoherent. The effects of partial coherence are discussed later.

If the geometrical wave function is real and positive then the phase factor $e^{i\phi(r_\perp,z)}$ must be equal to 1. Therefore $\psi_g(x_i,y_i) = |\psi_g(x_i,y_i)| = e^{-(r_{i\perp}/d_s)^2}$, where $r_{i\perp} = (x_i,y_i)$. However, there is always a phase error present because of aberrations and the diffraction caused by the aperture. If there is just diffraction because of a finite circular aperture without any aberrations, the phase oscillates between $-\pi$ and $+\pi$. For a simpler analysis here we considered a monochromatic system which means $\Delta E = 0$ and $\Delta\lambda = 0$. Magnetic lenses inherently induce wavefront aberrations which can be modeled as a phase function $W(x_l,y_l) = e^{i\phi(x_l,y_l)}$. In this case, when the lens system has aberrations, the aperture function becomes $[A(x_l,y_l)W(x_l,y_l)]$ and the coherent PSF then becomes,

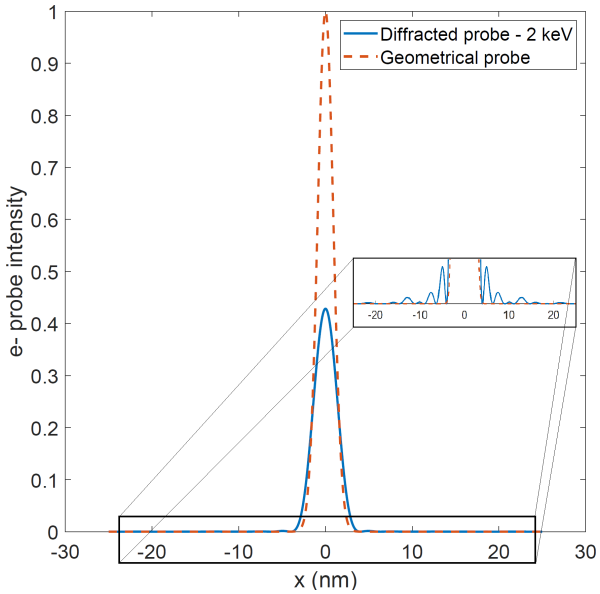

Figure 2.3: Simulation showing the wave nature of electron beam in an SEM column. The geometrical probe is the probe profile plotted just by using the brightness equation. The diffracted probe is the profile that shows the effect of $\lambda(V_o)$ and the zoomed-in ripples show diffraction through a finite aperture.

$$PSF_{optics} = h(x_i,y_i) = F[A(x_l,y_l)W(x_l,y_l)] \tag{2.2.7}$$

For a Gaussian geometrical image, when imaged through a circular aperture it will produce $J_1(x_i, y_i)$, a Bessel function of the first kind, and the probability density will be $|\psi_i(x_i, y_i)|^2 = |J_1(x_i, y_i)|^2$, which is shown above in Figure 2.3.

2.2.4 Aberrations

In an ideal situation, the description of the beam in Figure 2.3 is accurate. However, the beam intensity never has a perfect airy disk pattern because of aberrations. These aberrations can be broadly classified as coherent and incoherent aberrations which further can be classified as shown in Figure 2.4. The Seidel aberrations are third-order

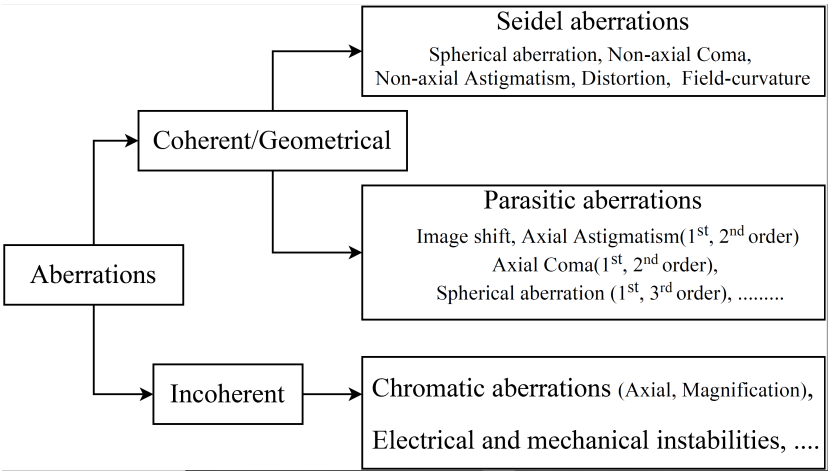

Figure 2.4: Classification of aberrations in electron microscopes and optical instruments.

inherent aberrations that are always present in monochromatic non-paraxial electron beams. In practice, if we are working at high magnifications and it is correct to assume the non-axial aberrations are small, only spherical aberration contributes significantly to the wavefront error. However, non-axial coma and astigmatism can also affect the probe. Therefore, we have included the first three Seidel aberrations and defocus in our implementation shown in Table 2.1.

For simulating Seidel aberrations we have modeled the aberrations in terms of a wavefront error function [9]. It expresses the optical path difference in terms of (x_o, y_o)

Aberrations	Coefficient(# of λ)	Wavefront error
Defocus	W_d	$W_d\ r^2$
Spherical	W_{040}	$W_{040}\ r^4$
Coma	W_{131}	$W_{131}\ u_o\ x\ r^2$
Astigmatism	W_{222}	$W_{222}\ u_o\ x^2$

Table 2.1: Defocus and Seidel aberrations (spherical aberration, non-axial coma and astigmatism). [9]

and u_o, which are normalized coordinates in the aperture plane and the normalized length in the image plane, respectively. The normalized aperture has a radius of 1 where the physical coordinates (x, y) are divided by the aperture radius to get normalized coordinates. u_o is a fractional image (probe) width or normalized image width. The fractional image length is the physical height of a given point in the image divided by the maximum image radius being considered. Here, $r = \sqrt{x^2 + y^2}$, $x = rcos\theta$ and W is the wavefront error function shown in Figure 2.5.

$$W(u_o; r, \theta) = \sum_{j,m,n} W_{klm} u_o^k r^l cos^m \theta \tag{2.2.8}$$

where $k = 2j + m$, $l = 2n + m$.

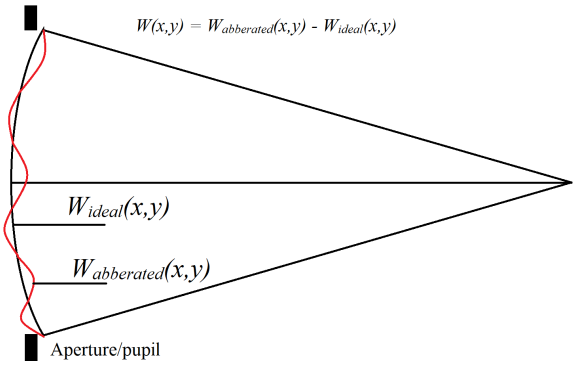

Figure 2.5: Wavefront aberration function schematic diagram. Deviation is shown from a perfectly spherical and converging wavefront.

Parasitic aberrations are aberrations that are not inherent to the system and are due to a non-uniform magnetic field, inaccurate shape of the pole pieces, and slight

misalignment of lens aperture from the optical axis. The axial coma, axial astigmatism, and image shift are some examples of this type of aberration. It is interesting to note that spherical aberrations can inherently be present in the system and can also be caused by system non-uniformity. There are different types of notations to represent axial aberrations [82, 56, 83]. For our simulation of parasitic aberrations, we use the notation used by Haider *et al.* [56] which is shown below as

$$W(\omega) = \frac{2\pi}{\lambda}\,\mathrm{Re}\,[A_0\omega' + \frac{1}{2}A_1\omega'^2 + \frac{1}{2}C_1\omega'\omega + \frac{1}{3}\omega'^3 + B_2\omega'^2\omega + \frac{1}{4}C_3\omega'^2\omega^2 + S_3\omega^3\omega' + ...] \tag{2.2.9}$$

where Re is the real part of the bracketed quantity, ω' is the complex conjugate, and in this version of the simulation, $\omega = \lambda k_x + i\lambda k_y$ are vectors of the Fourier space, and A_0 (beam/image shift), A_1 (two-fold axial astigmatism), B_1 (defocus), C_1 (three-fold axial astigmatism), etc. are the aberration coefficients. In our implementation, we have added higher-order aberrations (with the nomenclature) up to order 8. Both the Seidel and parasitic aberrations are multiplied by the aperture transfer function as a wavefront error represented by an exponential phase factor. In general, incoherent aberrations like chromatic aberration have the effect of broadening the focal spread and therefore degrading the spatial resolution.

2.2.5 Partial coherence simulation and the probe

2.2.5.1 Coherence of the source

Coherence is crucial in the rigorous description of any imaging system. It is defined as a measure of correlation between the phases at different points on a wave in space and time. Coherence is a very broad research area and we will restrict our discussion here only to its effects on probe formation in FEGs. In the context of electron microscopy,

highly coherent electron sources are desirable as they produce better-quality images because of their ability to form smaller probes with a very narrow spread in energy. FEGs have both high spatial and temporal coherence. But in practice, no source is completely coherent; rather it has partial coherence. There are many approaches to simulate both spatial and temporal partial coherence [9, 84, 85, 86, 87, 88]. For our implementation, we have used the method of 'explicit focal averaging' [89, 87] to simulate the effect of partial temporal coherence and the mutual coherence function [87, 75] to simulate partial spatial coherence.

2.2.5.2 Temporal coherence

Partial temporal (longitudinal) coherence in FEGs arises due to a small energy spread ΔE in the electron gun. This small energy spread is one of the primary contributors to chromatic aberration in the lenses (other factors like lens current fluctuations and unstable voltage also contribute to chromatic aberration). The spread in beam energy (ΔE) causes a small spread in the wavelengths of electrons ($\Delta\lambda$). Different wavelengths are focused at different focal points creating a longitudinal focal spread (Δf) shown in Figure 2.6. The focal spread caused only by the spread in beam energy is calculated as

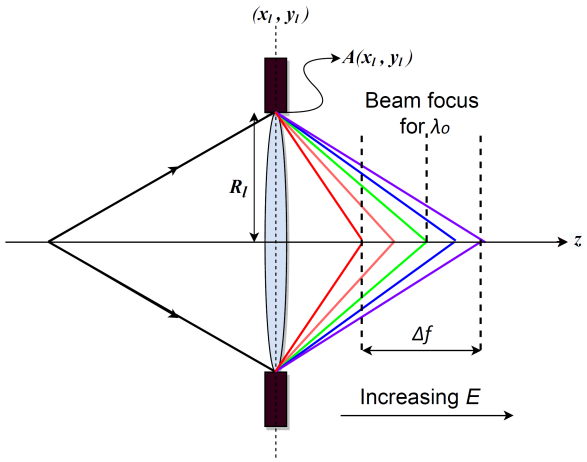

Figure 2.6: Diagram for axial chromatic aberration caused by partial temporal coherence (spread in beam energy)

$\Delta f \approx 2f_o\ (\Delta\lambda/\lambda_o)$ [90], where λ_o is the central wavelength and f_o is the focal distance corresponding to that wavelength. A more accurate calculation of Δf [91, 92] shown in Equation 2.2.10, requires the knowledge of the chromatic aberration coefficient (C_c, which is typically of the order of f_o), current instability in objective lens ($\Delta I/I$) and voltage instabilities ($\Delta V/V$).

$$\widetilde{\Delta f} = C_c\sqrt{\left(\frac{\Delta E}{E}\right)^2 + \left(\frac{\Delta V}{V}\right)^2 + \left(\frac{2\Delta I}{I}\right)^2} \tag{2.2.10}$$

It is worth mentioning that value of Δf and $\widetilde{\Delta f}$ for $f_o = C_c = 4.7007mm$, $\Delta I/I = 1 \times 10^{-6}$ and $\Delta V/V = 0.5 \times 10^{-6}$ [92] were found to be same up to two decimal places in $\mu m's$. Therefore, we use both formulae in our simulations interchangeably. To implement the effect of focal blur in probe broadening we use $\widetilde{\Delta f}$ and to show the variation in α_p we use Δf. In our simulations we have used $\Delta E = 0.2\ and\ 0.8\ eV$ for varying degree of temporal coherence (shown later in Figure 2.12).

2.2.5.3 Spatial coherence

Ideally, we would want a point source having a δ-distribution. However, in practice, all the sources have a finite width to them which gives rise to partial spatial (transverse) coherence. What this means is that every point on the source produces spherical waves, incoherent to each other, that are imaged through the lens as shown in Figure 2.7. The wave field in the specimen plane can be modeled as the summation of incoherent images weighted according to the source distribution. This is formulated in terms of the mutual coherence function [66]. The intensity of the wave field can be given by the convolution of the probe intensity with the geometrical image of the source in the specimen plane (ψ_g) [75].

$$\widetilde{\psi}_i(x_i, y_i) = |\psi_i(x_i, y_i)|^2 \otimes \psi_g(x_i, y_i) \tag{2.2.11}$$

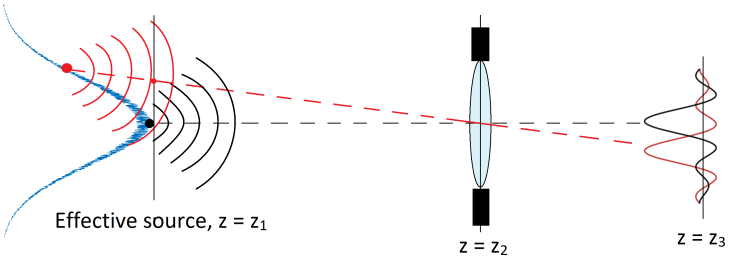

Figure 2.7: Diagram to explain the effect of finite source size which gives rise to partial spatial coherence. All the points in the effective source plane produce spherical waves. The off-axis point is also located in the plane ($z = z_1$). The Gaussian distribution shows the source intensity distribution in the plane.

where $\psi_g(x_i, y_i) = (1/|M|)\psi_s(x_i/M, y_i/M)$.

2.2.6 Specimen imaging and probe reconstruction

When the electron beam interacts with the specimen, the phase of the beam is lost. Therefore, the beam footprint is the intensity of the final wave function ψ_i in the specimen plane $z = z_3$, $|\psi_i(x_i, y_i)|^2$. The specimen structure signal (S_o) [51] is generated at every point on the specimen due to the interaction with primary beam electrons. According to this definition, the final SE/BSE image intensity is obtained by the convolution of the electron beam intensity with specimen structure signal S_o. This is the same equation mentioned earlier in Equation 1.3.3.

$$S_i(x, y) = |\psi_i(x_i, y_i)|^2 \otimes S_o(x_i, y_i) \tag{2.2.12}$$

So, if the structure signal is a delta function, *i.e.* $S_o = \delta(x, y)$ then the beam intensity can be thought of as the PSF of the structure signal imaging process, which blurs S_o. However, it must be stated that in practice the S_o will never actually be a delta function because the electrons are scattered within the specimen. It should be noted that, if we know S_o, then given the final image we can calculate the beam intensity using a Wiener deconvolution [6]. In our simulations, we assume that we have S_o which is shown in

Figure 2.8. The process of probe formation and imaging has been summarized in Table 1.1. In practice, noise ($\eta(x, y)$) is always present in the final image. The model for imaging with noise and then probe reconstruction through Wiener deconvolution is shown below.

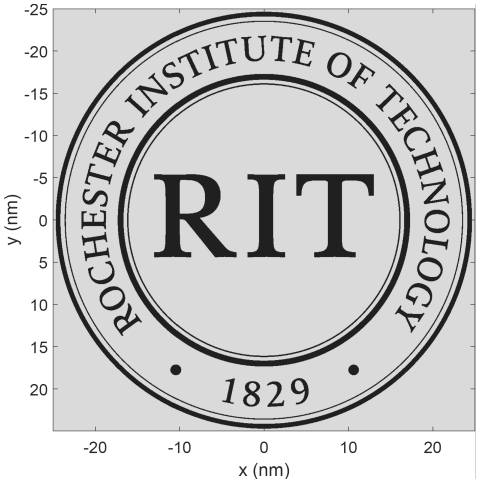

Figure 2.8: RIT object used as a specimen structure signal (S_o) in our simulations.

$$S_i(x, y) = S_o(x, y) \otimes psf(x, y) + \eta(x, y) \tag{2.2.13}$$

$$\widehat{S_I(f_x, f_y)} = \widehat{S_O(f_x, f_y)} \cdot OTF(f_x, f_y) + N(f_x, f_y) \tag{2.2.14}$$

$$\widetilde{psf} = F^{-1}\left[\left(\frac{\widehat{S_O}^*}{|\widehat{S_O}|^2 + K}\right) \cdot \widehat{S_I}\right] \tag{2.2.15}$$

where $psf(x, y)$ is the probe intensity and $OTF(f_x, f_y)$ is its Fourier transform, Equation 2.2.14 is the Fourier transform of Equation 2.2.13, $\widehat{S_O}^*$ is the complex conjugate of $\widehat{S_O(f_x, f_y)}$, $\widetilde{psf}$ is the reconstructed probe intensity and $K = \frac{|N|^2}{|OTF|^2}$.

2.2.7 Simulation parameters

Aliasing is one of the major factors which affects the accuracy of our simulation. To ensure that there is no aliasing error, we calculated the constraints on sampling and length on the image plane in consideration. Here, the image plane means the plane

$z = z_3$ in Figure 2.2, where the focused probe image is formed. The convolution between the specimen structure signal and the beam irradiance (probability density) gives us the final image of the specimen.

Let L be the length under consideration in the image plane ($z = z_3$) and Δx_i be the sampling interval. Therefore, the Nyquist frequency is the highest available spatial frequency in the signal $f_N = 1/2\Delta x_i$. The cut-off frequency $f_c = \alpha_p/\lambda = R_l/z_i\lambda$ sets an upper limit on the ψ_g in the image plane. However, we are concerned with $|\psi_g|^2$ and from the cut-off frequency f_c we know that the maximum possible frequency in the image (irradiance) is $2f_c$, [9]. Therefore, to prevent aliasing in the simulation, we must ensure that the Nyquist frequency is always greater than or equal to twice the cut-off frequency.

$$\begin{aligned} f_N \geq 2f_c; \;\; \Rightarrow \frac{1}{2\Delta x_i} &\geq \frac{2R_l}{z_i\lambda} \;\; ; \\ \Rightarrow \Delta x_i &\leq \frac{1}{4f_c} \end{aligned} \tag{2.2.16}$$

Multiplying both sides with N (# of samples), we arrive at a relationship between L and N.

$$\Rightarrow N\Delta x_i \leq \frac{N}{4f_c} \Rightarrow L \leq \frac{N}{4f_c} \tag{2.2.17}$$

So, in the simulation choice of L and N always must be such that it should comfortably satisfy the above-derived condition. For instance, using practical values $R_l = 50\mu m$, $V_o = 5kV$, $\alpha_p = 5mrad$ and satisfying all the conditions, we calculated some values presented in the Table 2.2. For all the results shown in this paper, we have always used $N = 4096$ and $L = 50nm$.

The other simulation parameter, which is pivotal to the beam intensity reconstruction is the noise. We can add noise in the simulation at two stages: Poisson noise to

# of Samples	L - length on plane $z = z_3$
4096	$\leq 3555.55\ nm$
2048	$\leq 1778.6\ nm$
1024	$\leq 889.3\ nm$
512	$\leq 444.6\ nm$

Table 2.2: Values to choose in order to avoid aliasing

the electron beam before interaction with the specimen and then a Gaussian noise to the final specimen image generated which represents the noise added by the detection system. Noise distribution in the final image helps us choose the value of K (the Wiener filter parameter) described above in Equation 2.2.15.

2.3 Simulation Results

2.3.1 Effect of diffraction

All imaging systems which have a finite aperture, are limited by diffraction. As we state in Equation 2.2.4 and 2.2.5, the objective aperture limits the higher frequencies to contribute to the probe formation. The coherent point-spread function (PSF_{lens}) is the Fourier transform of the aperture function which is defined in Equation 2.2.4 and is scaled by λ. As we go higher in beam energy (E), λ decreases and thus PSF_{lens} becomes smaller. Therefore, we get narrower probes and better resolution at higher voltages as demonstrated in Figure 2.9. The amplitude of the probe intensity also decreases as the probe broadens with the decrease in beam energy E. The energy within the probe is distributed at the sides causing the amplitude to go down as shown in Figure 2.10. Almost no probe broadening or amplitude reduction was found in our simulations for voltages $\geq 15kV$. Therefore, the effect of diffraction as probe broadening and reduction in probe amplitude is more noticeable at lower voltages.

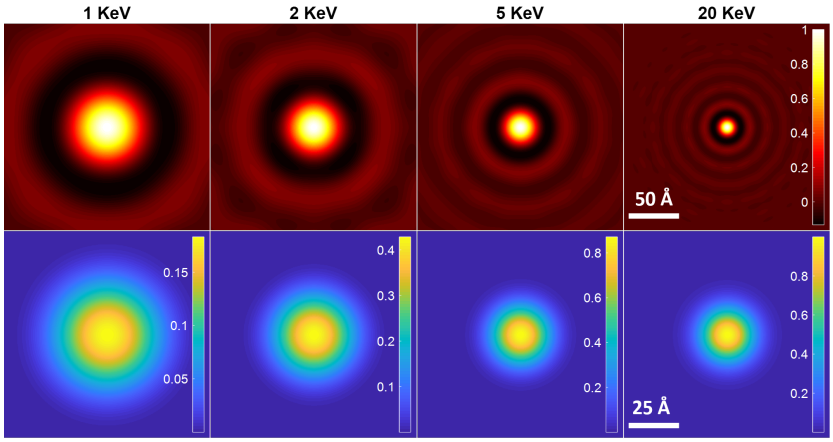

Figure 2.9: Normalized PSF of the electron lens system (top row) and probe intensity (bottom row) at the specimen variation w.r.t beam voltage (V_o).

2.3.2 Effect of partial coherence

Partially coherent illumination is another factor that affects probe formation in SEMs. We have examined the effects of partial coherence and explained them through Figure 2.11, Figure 2.12, Figure 2.13, and Table 2.3. We found in our simulations that for FEGs, spatial coherence has a more significant effect on the final probe than the temporal coherence of the source. However, at lower voltages the effect of partial coherence (chromatic aberration) is dominant. The probe profiles (without aberrations) are shown in Figure 2.11 for $V_o = 2$ and $20kV$ to demonstrate the effect of finite source width ($d_s = 20nm$). The fully coherent probe at $20keV$ has no effect of partial coherence and diffraction and is identical to the geometrical probe. It is interesting to note that the coherent probe at $2keV$ is narrower than the partially coherent probe at $20keV$. This result shows how crucial the virtual source size is to achieve smaller probes. In theory, better resolution can be achieved at lower voltages just by having a smaller virtual source size.

However, spatial coherence is not the only factor, as at lower voltages temporal coherence also has a major effect. We calculate the focal spread caused by the spread in

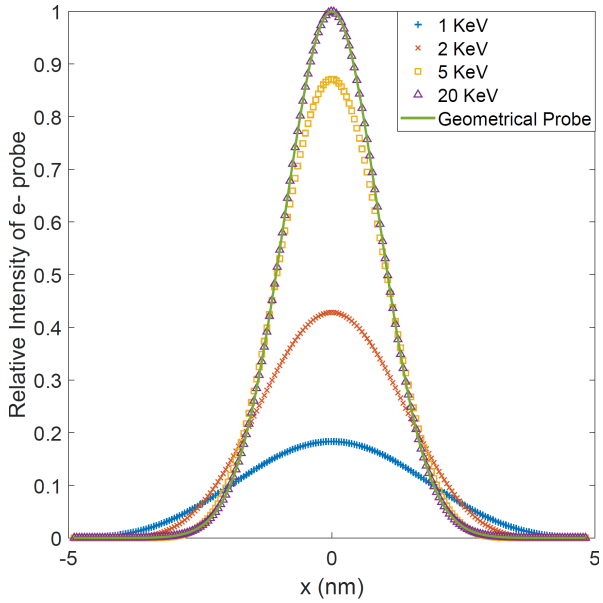

Figure 2.10: Relative intensity reduction and broadening of the probe profile because of diffraction and voltage (V_o) variation.

beam energy which is shown in Table 2.3. It can be observed that Δf has a monotonous relation with $\gamma = \Delta E/E$. As γ becomes smaller the focal spread decreases. Note that even for the largest value of $\gamma = 0.0004$, $\Delta f \approx 1.89\mu m$ which is 3 orders of magnitude smaller than the mean focal length f_o. Another visualisation is shown in Figure 2.12 where the variation in convergence angle (α_p) is shown for different values of $f \in [f_{min}, f_{max}]$ drawn from a Gaussian focal distribution with $\mu = f_o$, $f_{min} = f_o - \Delta f/2$ and $f_{max} = f_o + \Delta f/2$. The largest variation in α_p is for $\Delta E = 0.8eV$ at $E = 2kEV$ and the smallest variation is for $\Delta E = 0.2eV$ at $E = 20kEV$. Our simulations also demonstrate that cold-FEGs produce smaller probes and better resolution compared to Schottky FEGs. Typically cold FEGs have smaller virtual source size (d_s) and energy spread (ΔE) and therefore, better coherence properties than Schottky FEGs.

.

To show the effect of partial temporal coherence on probe broadening we calculate the focal spread ($\widetilde{\Delta f}$) using Equation 2.2.10. For this simulation we have used $C_c =$

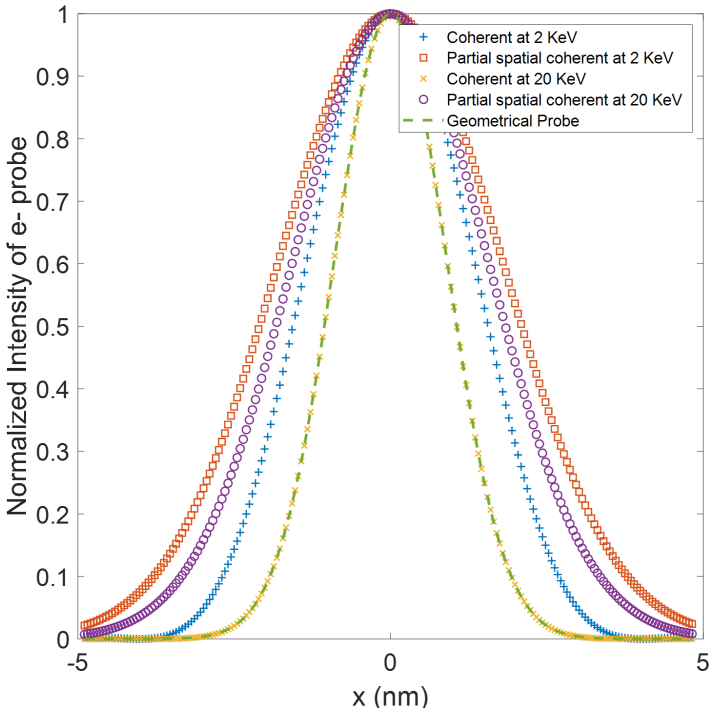

Figure 2.11: Probe broadening caused by the partial spatial coherence of the electron source (finite virtual source size $d_s = 20nm$)

$\Delta E\ (eV)$	$E\ (keV)$	γ	$\Delta f\ (m)$
0.8	2	0.0004	1.8845×10^{-6}
0.2	2	0.0001	4.7103×10^{-7}
0.8	20	0.00004	1.9164×10^{-7}
0.2	20	0.00001	4.7910×10^{-8}

Table 2.3: Focal variation caused by energy spread (ΔE) in the beam with the mean focal length $f_o = 4.7007mm$ corresponding to the central wavelength λ_o.

$6mm$, $\Delta I/I = 1 \times 10^{-6}$ and $\Delta V/V = 0.5 \times 10^{-6}$. Using the spread in focal length ($\widetilde{\Delta f}$) around f_o the change in z_i is calculated as Δz_i. Following that, we select multiple values from $z_i \in [(z_i)_{min}, (z_i)_{max}]$ at equal intervals. Then for all values of selected $z_i's$ we propagate the probe intensity from the central plane ($\Delta z_i = 0$) to the defocused plane ($\Delta z_i \neq 0$) using a Fresnel propagator, $e^{-i\pi\lambda_o z_i(f_x^2+f_y^2)}$. Finally, all the generated probe images at different z-planes are summed together and normalized. The result shown in Figure 2.13 corroborates the known fact that at lower voltages chromatic

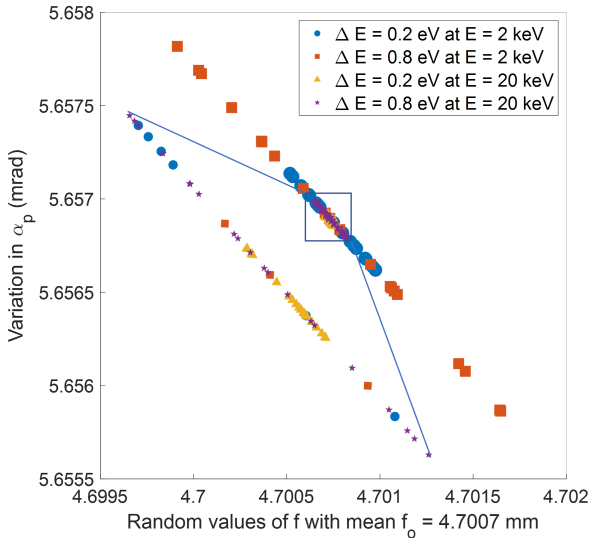

Figure 2.12: Spread in convergence angle of the probe (α_p) is shown. Energy spread in the beam leads to spread in the wavelength. Different wavelengths are focused at different points on the z-axis changing the convergence angle and hence the cut-off frequency $f_c = \alpha_p/\lambda$. Zoomed-in region of the graph shows the focal distribution for $E = 20keV$.

aberration degrades the resolution in SEM.

2.3.3 Effect of aberrations

Aberrations can not only affect the size but also the shape of the probe. Aberrations like defocus and spherical aberration broaden the probe but keep the probe symmetric. But, aberrations like coma and astigmatism can make the probe asymmetric. In Figure 2.14, we show that as we change the coefficient of spherical aberration (W_{040}), the probe broadens and the imaging resolution degrades. It is important to note that the effect of negative and positive coefficients is the same as spherical aberration is an even function.

However, Figure 2.15 shows the effect of aberrations where the probe no longer remains symmetric. This simulation experiment was done with the following values of input parameters; $\beta = 10^{12}\ A \cdot sr/m^2$, $i_p = 10^{-11}\ amps$, $\alpha_p = 5\ mrad$, $D = 50\ \mu m$,

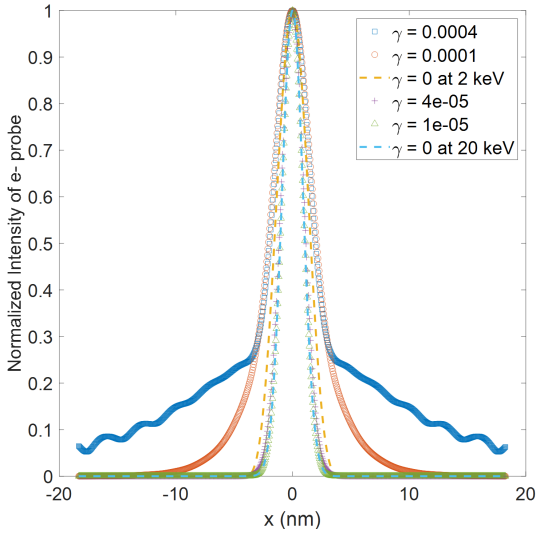

Figure 2.13: Probe broadening shown because of partial temporal coherence. The probe profiles are shown for $E = 2$ and $20keV$ and $\Delta E = 0.2$ and $0.8eV$. $\gamma = \Delta E/E$. $\gamma = 0$ represents the completely coherent case with $\Delta E = 0$.

$V_o = 5\ kV$, $d_s = 20\ nm$. The aberration coefficients; $W_d = 2.5\lambda$, $W_{040} = 3\lambda$, $W_{131} = 4\lambda$, $W_{222} = 2\lambda$. The arbitrary wavefront error function was constructed by adding two aberration functions; the first was the aberration function calculated by the input Seidel aberration coefficients with $x_o = 1$, $y_o = -2$, and the second was obtained by rotating the first by 90^o in the counter-clockwise direction.

Any arbitrary probe distribution can be constructed by introducing different permutations and combinations of Seidel and parasitic aberrations in the aperture function. Imaging using this aberrated probe is shown in Figure 2.16. There is a drastic degradation in the resolution of the final image. Although aberrations present inside a well-aligned SEM are parasitic, this shows the final resolution is very sensitive to changes in the probe.

Software description and use instructions

The software can be downloaded at (`https://github.com/suryaphysics`) and requires MATLAB compiler runtime library to run. The software comes with an executable

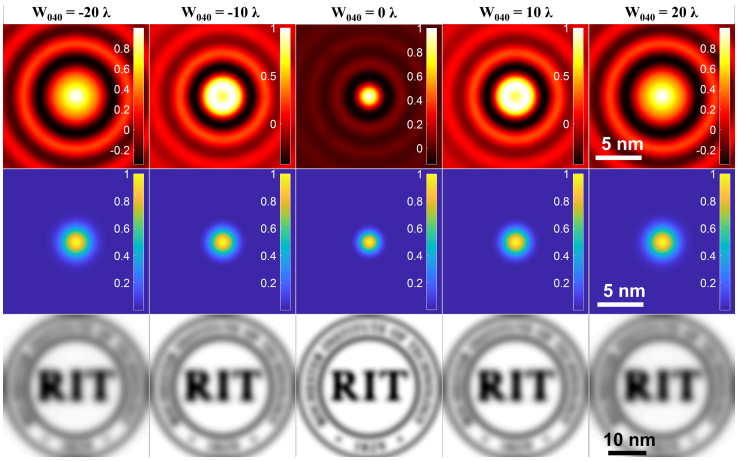

Figure 2.14: Effect of spherical aberration coefficient (W_{040}) variation on PSF of the electron lens (1^{st} row), the probe intensity (2^{nd} row), and the final image (3^{rd} row).

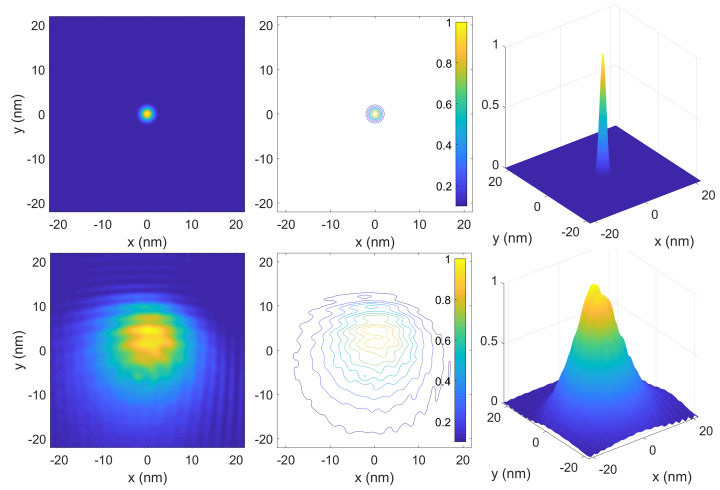

Figure 2.15: Normalized probe intensity visualization in top view (left column), contour view (middle column), and 3D surface view (right column). Effect of only diffraction through the aperture (top row), Diffraction coupled with an arbitrarily constructed wavefront aberration function included in the aperture function of the lens (bottom row).

(.exe) file which will automatically install all the dependencies including the runtime library, the first time you install it. This is the first release of the software as *'SEM Nano, Version 1.0'*. Only coherent imaging of the probe is included in this release. It is open source and is freely available for use under the MIT License of the open source initiative. The software is more suited for academic use and is not designed with detailed

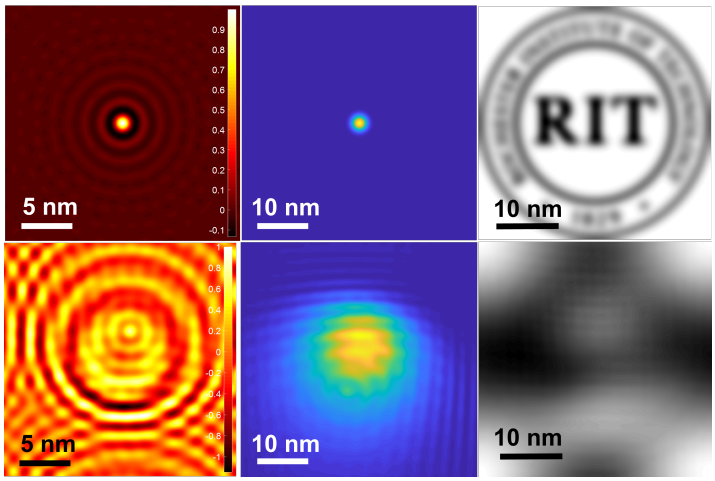

Figure 2.16: Effect of aberrations shown on lens PSF, probe formation and imaging. Normalized PSF of electron lens (left column), normalized probe intensity (middle column), final specimen image (right column). Effect of only diffraction through aperture (top row). Diffraction coupled with an arbitrarily constructed wavefront aberration function included in the aperture function of the lens (bottom row).

attention to software engineering standards. Listed below is a step-wise description of using the software.

Step 1: Provide all the input parameters (gun parameters, probe parameters, simulation parameters, and lens parameters) and click on **Run** button.

Step 2: Wait for the calculations until the probe intensity is displayed in *Simulated* e^- *probe* tab. Here, we can visualize the probe with different display options.

Step 3: Then in the *Imaging and Probe Reconstruction* tab, load an image file and click on **Run**. The structure signal and its image using the simulated probe will be displayed.

Step 4: Next, Gaussian noise can be added to the final image using the noise percentage slider.

Step 5: To reconstruct the probe using the structure signal and the noisy image, use the slider for the Wiener filter parameter - **K**.

The **Reset** button restarts the software with all values set to default. PSF_{lens} and the

coherent transfer function can be displayed using the *Lens plots* menu.

This software is designed for microscopists to understand the optics of field-emission SEMs intuitively. Ideally, a more complete discussion for partial coherence would include a degree of coherence. This would be a subject for future research and will potentially be included in our future versions.

In this chapter, we presented the simulation program *'SEM Nano'*. We explained and demonstrated the process of probe formation in field-emission SEMs using the PSF model. Coherent imaging of the probe based on the objective lens action was explained and implemented. Different factors like aberrations, partial coherence, accelerating voltage, etc. were explored to analyze their effects on the probe and the final image. It was found in our simulations that the effect of diffraction through a finite aperture is negligible for $V_o \geq 15keV$ and is much more evident at $V_o \leq 10keV$. One of the most interesting observations was to note that a partial spatial coherent probe at $20keV$ was broader than a coherent probe at $2keV$. We also argued that temporal coherence has a scarce effect on probe broadening compared to spatial coherence of the source. However, at lower voltages partial temporal coherence which manifests as chromatic aberration is the limiting factor. Lastly, an arbitrary aberration function was constructed to demonstrate the potential degradation in resolution when aberrations are present.

Chapter 3

SEM Optics - Wave Optical Model II

We saw in the previous chapter that probe formation in scanning electron microscopes (SEM) is often reduced to the objective lens action modeling based on a point spread function or Fourier transforms. In this chapter, we present wave optical modeling of the complete SEM column based on plane-by-plane propagation of the electron beam wavefunction without simplifying the optical system. We establish the challenges in plane-by-plane beam propagation and show how sampling limitations produce aliased results. Through careful selection and combination of propagators, we have developed a general wave optical propagation method that can overcome the aliasing problem to achieve the appropriate probe widths. Using a two-step propagator, we show that it is possible to know the electron beam distribution throughout the column from the virtual source plane to the specimen plane. We also show that our results from the wave optical simulations converge with the geometrical theory of probe formation. Finally, as a direct application of this method, we were able to demonstrate the effect of aberrations in the condenser lens not just the probe forming objective lens. Designing beam shaping experiments, and studying the effect of partial coherence can be some of the novel applications of this work.

3.1 Background

Electron microscopes have been an excellent tool for probing nature at the nanoscale for many decades. Since the birth of quantum theory, it was theorized that electrons as an illumination source would produce far superior resolution compared to optical microscopes because of their smaller wavelengths. Scanning electron microscopes (SEM) were developed in the 1930s and became commercially available in the 1960s. The SEM contains two sub-imaging systems: a probe-forming lens system and beam-specimen interaction. The electron beam propagates through the SEM column from the electron gun to the specimen. The lens system of the SEM is designed to produce a focused electron probe at the specimen. The electron probe scans the specimen and produces different kinds of signals from the beam-specimen interaction. These signals are then recorded by the detectors to produce the final image.

Our work in this chapter is focused on the lens system of the SEM and probe formation. Optimizing the optics of the column is of prime importance in designing an SEM with the best achievable resolution. As the resolution of an SEM is fundamentally limited by the electron probe, modeling beam evolution through the column and probe formation is critical. Electron probe formation has been historically modeled by the geometrical-optical theory of probe formation [65]. This theory predicts a probe diameter that takes account of the Gaussian (geometrical) image of the beam, spherical aberration, chromatic aberration, and diffraction. There are many notable works to improve this theory that provide better measures of probe diameter calculations and insightful analyses based on it [72, 55, 73].

However, this theory inherently assumes that the probe is symmetric, which is not always the case [74]. Furthermore, the geometric description of lens aberrations is only appropriate for older SEMs with thermionic guns as they produce incoherent illumina-

tion. For modern SEMs with Schottky and cold field emission guns, the illumination is highly coherent, and therefore a wave optical treatment of lens and aberrations becomes necessary [65]. The standard approach for modeling electron beam propagation in the SEM column is based on classical electrodynamics, where electrons are treated as charged point-like particles being manipulated by electromagnetic fields. Researchers both in industry and academia primarily depend on electrodynamics-based simulation software like Simion, Munro's Electron Beam Software [93, 94] (MEBS), COMSOL, EOD [95], etc. to model SEM columns. These software use different numerical methods like finite difference method (FDM), finite element method (FEM), charge simulation method (CSM), etc. to calculate fields and classical perturbation theory or geometric ray tracing to compute electron trajectories [96, 24, 97, 98].

However, electrons are also quantum mechanical objects that exhibit wave nature. The more accurate treatment of the electron beams comes from quantum mechanics where the beam wave function follows the theory of wave optics [67]. As the world moves towards quantum technologies, a rigorous understanding of electron beam propagation and probe formation in SEMs using wave optics becomes increasingly relevant. For instance, it has direct importance for aberration-corrected systems [36](Haider Müller, 2016; Hirose et al., 2011; Inada et al., 2009; Joy, 2005) where diffraction becomes the most significant factor that limits the achievable resolution in a SEM. Electron beam shaping has become a very active area of research in the past decade [67, 99, 70]. Knowledge of the beam wavefunction throughout the SEM column would be extremely helpful to design effective experiments with phase masks.

Modeling of electron beams using wave optics is not new to the field of SEM. The wave optical theory of probe formation treats lens action and aberrations as phase shifts that manipulate the beam wavefunction [100, 65, 95]. However, often the SEM column is simplified using a single objective lens system [76, 4, 70] based on a point-

spread function (PSF) approach [24]. The existing simulations like SEM Nano [101, 4], etc. which model probe formation, define all the parameters including the PSF on the specimen plane. A Gaussian (geometrical) image is calculated that is blurred by this PSF to produce the final probe distribution.

Although for modern SEMs, the objective lens is the only lens that produces demagnification [65], there are multiple drawbacks to the single-lens PSF approach. First, SEMs have multiple lenses in the column that manipulate the beam. All these lenses have their aberrations and actions which are lost in the simplified picture. Second, there is no actual beam propagation being modeled as all the parameters are defined on the specimen plane. Third, in theory, a PSF can only be defined for optical systems that are linear and shift-invariant (LSI) [80]. SEMs have multiple lenses and apertures that are all in different planes. This means that the system in theory is not strictly LSI and might suffer vignetting [102, 80]. Therefore, to obtain an electron probe distribution that is a function of diffraction through apertures, wavefront aberrations of lenses, and source coherence, the wave optical description of beam propagation through the column is essential. But even with the exact column measurements and dimensions, a plane-by-plane wave propagation of the electron beam wave function from source to specimen is not straightforward, as shown later in the chapter.

3.2 Plane-by-plane propagation model

3.2.1 Optical Setup

In older SEMs with thermionic electron guns, the beam was demagnified multiple times through the column to produce a small probe. The condenser lens and the other lenses throughout the column successively minimized the beam. Modern SEMs with field-emission electron guns don't need successive demagnification to produce a probe size

of 1-5 nm. Our optical design has two lenses: a condenser lens and an objective lens. As field emission guns (FEGs) have a virtual source size ranging from 3-5 nm for cold FEGs and 15-20 nm for Schottky guns [65], probe formation is mostly done by the objective lens. For instance, in our setup of a hypothetical SEM column (Figure 3.1), the condenser lens is placed in the column in such a way that the object distance (virtual source) is just smaller than the focal length of the lens. Therefore, it does not minimize the beam but instead focuses it marginally. This action forms an enlarged virtual image of the beam that is then minimized by the objective lens. Typically, the condenser lens is a weak lens with a longer focal length and the objective lens is a strong lens with a smaller focal length. One fact that is also important to note is that the apertures used in the column are not in the lens plane. Based on these requirements we have used the optical design shown in Figure 3.1 as a model for all the simulations shown in this chapter.

In this chapter, we aim to give a clear description of how to model a given SEM column design using wave optical propagation and produce a demagnified probe distribution. We start by choosing an optimal wave propagation function that produces the least artifacts and aliasing. Then we show that a plane-by-plane wave propagation in SEM suffers aliasing due to under-sampling with traditional propagators. There are two approaches we have used to solve the under-sampling problem; lens action modeled as an optical Fourier transform and plane-by-plane propagation assisted with a two-step propagator [9, 103]. We show the first successful implementation of plane-by-plane wave propagation using a two-step propagator function in SEM that does not suffer from under-sampling and produces a demagnified probe distribution at the specimen. Finally, we provide a comparison of different methods to corroborate our results. It should be noted that all the wave simulations shown in this paper are implemented for coherent illumination. Although this work concentrates on SEMs specifically, the

concepts and simulations developed in the paper can easily be extended to any probe-forming system like focused ion beam (FIB) microscopes, or lithography systems.

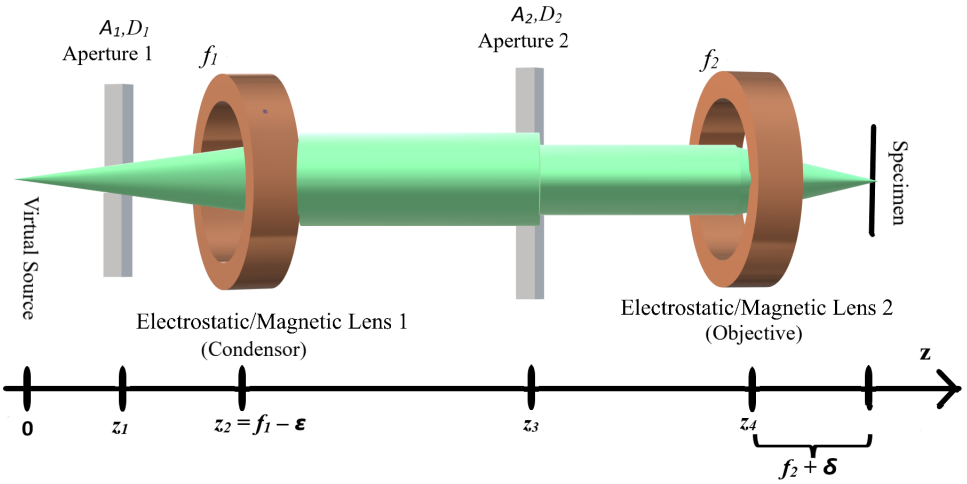

Figure 3.1: Optical setup used for the simulations shown in this manuscript. '$f_1' = f_{condensor}$ and '$f_2' = f_{objective}$ are the focal lengths of the lenses. A_1 and A_2 are the amplitude transmission of the apertures, D_1 and D_2 are the diameters of the apertures. $'\epsilon'$ is a small number to ensure that the virtual source is placed at a distance less than the f_1, and $'\delta'$ is a small number that shows that the beam is not focused on the focal distance but the Gaussian (geometrical) image plane.

3.2.2 Optics

3.2.2.1 Plane-by-plane wave propagation

A plane-by-plane propagation can be defined as follows: All physical apertures act as an amplitude transmission function. For instance, an aperture can be defined as in Equation 3.2.1

$$A\left(r_\perp, z = z_i\right) = 1 \quad \forall \quad r_\perp \leq \frac{D}{2} \; ; \quad 0 \; else \; where \tag{3.2.1}$$

where, $r_\perp = \sqrt{x^2 + y^2}$, and D is the aperture diameter. All lenses are modeled as phase transmission functions where an ideal lens that produces a perfectly converging/-diverging wavefront can be represented using a quadratic phase function $e^{\pm ik(r_\perp)^2/2f}$. Any deviation from an ideal quadratic phase generated by the lenses are wavefront

aberrations that themselves are phase functions. All propagations from one plane to another are modeled using propagator functions that relate the wavefunctions in the input and output plane.

3.2.2.2 Propagator functions and sampling

Wave optical propagation of optical fields is based on a propagator function that relates the input wavefunction in the object plane (virtual source plane) and the output wavefunction in the image plane (specimen plane). Realistic wave optical modeling of propagation relies heavily on the numerical calculations of diffraction. There are many existing techniques to calculate diffraction numerically [80, 5] which vary in accuracy and computational complexity. Most of these techniques are based on FFT methods or convolution-based propagators. For our problem, convolution-based propagators are the obvious choice as they offer us more flexibility to choose propagation between any two planes. Four most used convolution propagators are shown in Table 3.1, where $r = \sqrt{x^2 + y^2 + z^2}$. As shown in Table 3.1, the Fres-IR and RSC functions are

Propagator function	Mathematical formulation
Fresnel Impulse response (Fres-IR)	$h(x,y) = \frac{e^{ikz}}{i\lambda z} e^{\frac{ik(x^2+y^2)}{2z}}$
Fresnel Transfer function (Fres-TF)	$H(f_x,\ f_y) = e^{ikz} e^{-i\pi\lambda z(f_x^2 + f_y^2)}$
Angular Spectrum Method (ASM)	$H_{ASM}(f_x,\ f_y) = e^{ikz\sqrt{1-(\lambda f_x)^2-(\lambda f_y)^2}}$
Rayleigh Sommerfeld Convolution (RSC)	$h_{RSC}(x,y) = \frac{1}{2\pi}\frac{z}{r}\left(\frac{1}{r} - ik\right)\frac{e^{ikr}}{r}$

Table 3.1: Convolution-based propagator functions

spatial domain propagators, and Fres-TF and ASM are Fourier domain propagators. Also, (Fres-IR, Fres-TF) and (ASM, RSC) are conjugate pairs and are related to each other by a Fourier transform relationship. All these propagators have different propagation distance ranges and bandwidth ranges for which they are preferred. This is summarized in Figure 3.2. Although mathematically the spatial domain and Fourier domain propagators are Fourier transform pairs, their propagation ranges are compli-

mentary because of discrete sampling. In Figure 3.2, $z_1 = \frac{2N(\triangle x)^2}{\lambda}\sqrt{1-(\frac{\lambda}{2\triangle x})^2}$ and $z_2 = \frac{2N(\triangle x)^2}{\lambda}$, $\Gamma = \lambda f_x$. For a plane length of L and N pixels, the sample size is $\triangle x = \frac{L}{N}$ and the maximum spatial frequency is $f_x = \frac{1}{2\triangle x}$. It is interesting to note that when $\triangle x \gg \lambda$, ASM and RSC degenerate into Fres-TF and Fres-IR respectively and z_1 becomes equal to z_2. Therefore, for our simulations we are going to use the more general propagator functions ASM and RSC as they offer more bandwidth support and there is no paraxial approximation used for the electron beam. We show results in the next section to compare and choose the optimal propagator between ASM and RSC.

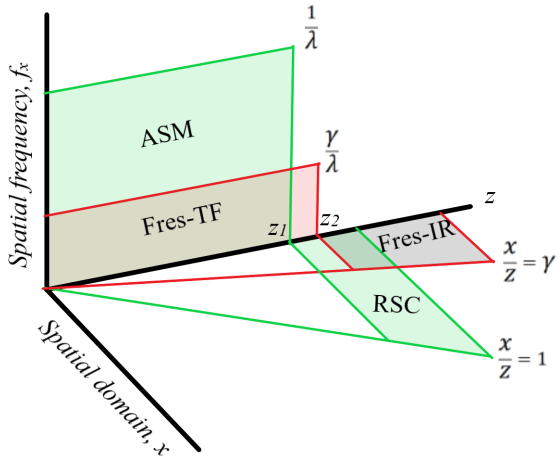

Figure 3.2: Schematic diagram for propagation and bandwidth ranges for convolution-based propagator functions [5]. ASM - Angular spectrum method, Fres-TF - Fresnel transfer function, RSC - Rayleigh-Sommerfeld convolution, Fres-IR - Fresnel impulse response.

3.2.2.3 Modeling Lens

Lens as a phase transmission

A lens as an optical element is a device that converges/diverges a beam. The action of a lens can be modeled in different ways. In theory, for an incoming plane wave an ideal lens modifies the planar wavefront into a spherical wavefront which can be approximated as a quadratic phase. Therefore, a lens can be represented as a quadratic

phase object, $T(x,y) = e^{\pm ik(x^2+y^2)/2f}$ that manipulates the incident beam phase, f is the focal length of the lens and k is the wavenumber. For our implementation, $\varphi_{condensor}(x,y) = \varphi_{objective}(x,y) = T(x,y)$ where the condenser lens and the objective lens have different focal lengths.

Lens action as an Optical Fourier transform

The Fourier transforming property of a lens states that for a plane wave illumination, the field at the front focal plane is related to the field at the back focal plane by an exact Fourier transform [80] as shown in Figure 3.3. This property can be very useful for cases where a complete wave-propagation through the lens is not necessary. Field distribution at the back-focal plane can be obtained without performing propagation through the lens as described in equation 3.2.2. Here, $u = \lambda f f_x$ and $v = \lambda f f_y$ are the spatial coordinates in the back-focal plane.

$$\psi_{(f)}(u,v) = \iint_{-\infty}^{\infty} \psi_{(-f)}(x,y)\, e^{-i\frac{2\pi}{\lambda f}(ux+vy)} dxdy \tag{3.2.2}$$

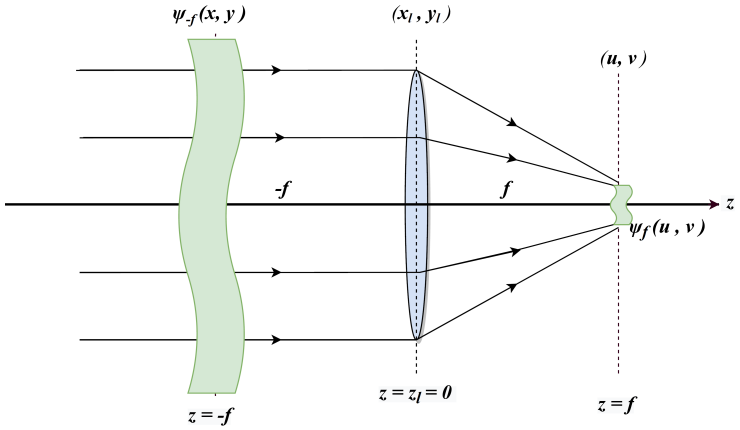

Figure 3.3: Fourier transforming property of lens.

Lens action using a wave propagation with two-step propagator

As we had mentioned in the previous section, the SEM optics is designed to demagnify the beam to produce a focused probe. Most of this demagnification is done by the objective lens. All lengths on the geometrical (Gaussian) image plane are demagnified therefore, it is difficult to use a straight-forward propagator function approach between the objective lens plane and the specimen plane. This is because all propagators assume the same plane length in the input and the output plane and hence suffer under-sampling as shown in the next section. To handle the case of different input-output plane lengths we propose the use of a two-step Fresnel propagator [103] which is described in Figure 3.4. The two-step Fresnel propagator propagates the wavefunction to an intermediate dummy frequency plane from both the input and the output plane. The wavefunction in this dummy plane $\psi_d\,(x_d, y_d)$ is calculated in terms of the input plane parameters (x_l, y_l) and output plane parameters (x_g, y_g) separately using a single step Fresnel propagator function. Then they are equated to each other, and the output plane wavefunction $\psi_g\,(x_g, y_g)$ is expressed as a combination of three chirp functions in (x_g, y_g), (x_d, y_d), and (x_l, y_l) as shown in Equation 3.2.3.

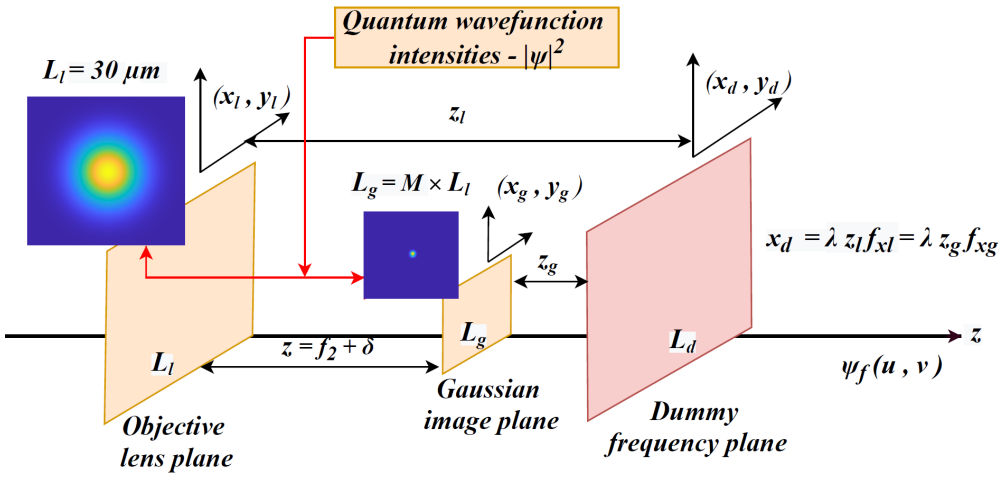

Figure 3.4: : Two-step Fresnel propagator setup between the objective lens plane and the geometrical (Gaussian) image plane. M is the demagnification factor.

$$\psi_g\left(x_g, y_g\right) = \frac{z_g}{z_l}\left[e^{ik(z_l - z_g)} e^{\frac{-ik\left({x_g}^2 + {y_g}^2\right)}{2z_g}}\right] \times$$
$$F^{-1}\left[e^{ik\left\{\frac{(z_g - z_l)\left({x_d}^2 + {y_d}^2\right)}{2z_l z_g}\right\}} F\left\{\psi_l\left(x_l, y_l\right) e^{\frac{ik\left({x_l}^2 + {y_l}^2\right)}{2z_l}}\right\}\right] \tag{3.2.3}$$

The next step is to relate the dummy plane parameters to the input plane parameters. The goal is to express the output wavefunction completely in terms of the known parameters. This is achieved by further simplifying equation 3.2.3 using equation 3.2.4 and 3.2.5.

$$z = z_l - z_g;\ \Delta x_l = L_l/N, \Delta x_g = L_g/N;$$
$$x_d = \lambda z_l f_{xl|max} = \lambda z_g f_{xg|max} \quad ,\ f_{xl|max} = 1/2\Delta x_l \tag{3.2.4}$$

$$\frac{z_l}{z_g} = \frac{L_l}{L_g} = \frac{\Delta x_l}{\Delta x_g} \tag{3.2.5}$$

Finally, we get an output function that is not dependent on the dummy plane parameters, and it is completely characterized using input and output plane chirp functions as shown in equation 3.2.6.

$$\psi_g\left(x_g, y_g\right) = \frac{L_g}{L_l}\left[e^{ikz} e^{\frac{-ik(L_l - L_g)\left({x_g}^2 + {y_g}^2\right)}{2zL_g}}\right] \times$$
$$F^{-1}\left[e^{-i\pi\lambda z\left\{\frac{L_l\left({f_{xl}}^2 + {f_{yl}}^2\right)}{L_g}\right\}} F\left\{\psi_l\left(x_l, y_l\right) e^{\frac{ik(L_l - L_g)\left({x_l}^2 + {y_l}^2\right)}{2zL_l}}\right\}\right] \tag{3.2.6}$$

3.2.2.4 Applications of plane-by-plane wave propagation

Lens Aberrations and Beam Shaping masks

The geometrical aberration coefficient provides the effect of aberrations on the image plane. In the wave optical picture, lens aberrations distort an ideal wavefront [104, 105]. These aberration functions can be treated as pure phase objects that are present in the

lens plane and can be just added to the quadratic phase that is produced by an ideal lens. This can be very useful to see the effect of aberrations on the probe for each lens which is not possible in the single lens PSF approach. Nano-structuring [67] of electron beams is done by using amplitude and phase masks to manipulate the beam wavefunction. Any arbitrary beam shape can be achieved using these masks. We have used a simple two-fold astigmatism aberration mask [106] as defined in Equation 3.2.7 to demonstrate the effect of aberration on the probe.

$$t_{aberration}\,(x,y) = \pi \; mod \left[\left\{ (x^2 - y^2) + \; \frac{1}{2} \right\} \; , \; 1 \right] \tag{3.2.7}$$

where (x, y) are spatial coordinates in the lens plane normalized with mask radius, and the factor π is used just to rescale the values from $[0, \pi]$.

Phase object approximation

It is important to explain that although all focusing elements like a lens, Fresnel zone plate, and magnetic lens do produce a quadratic phase, their physics is entirely different from one another. In this simulation, we are showing the effect of a lens using a quadratic phase object. In practice to model electron lenses (electrostatic lens/ magnetic lens/ compound immersion lens), a phase object approximation (POA) [107, 67] can be used. Any electromagnetic field existing between planes z_i and z_{i+1} along the direction of propagation can be treated as a thin phase object placed at plane z_i. The phase transmission function $T(x, y)$ for this phase object can be calculated using the equation

$$T\,(x,y,z=z_i) = \; e^{i\phi} = \; e^{i\pi \left[\frac{1}{\lambda E} \int_{z_i}^{z_{i+1}} V(x,y,z)dz \;\; - \;\; \frac{2e}{h} \int_{z_i}^{z_{i+1}} A_z(x,y,z)dz \right]} \tag{3.2.8}$$

where A_z is the z-component of the magnetic vector potential, V is the electrostatic scalar potential, e is the electron charge, E is the kinetic energy of electrons, h is the Planck's constant, and λ is the wavelength. So, whichever lens is being used the unwrapped phase calculated using Equation 3.2.8 should be close to quadratic in behavior.

3.2.2.5 Simulation Details

It is crucial to mention here that the beam in the SEM column is never parallel to the optical axis and does not have a planar wavefront. This implies that the beam is not focused on the back-focal plane but rather on the geometrical (Gaussian) image plane. The image plane distance can be easily found using an ABCD matrix-based ray tracing. For our optical setup shown in Figure 3.1, the geometrical (Gaussian) image plane is at $z = f_2 + \delta$ where $\delta \approx 0.01089\ mm$ and the demagnification was $M \approx 0.1038$. This means for a virtual source size of $d_s = 20\ nm$, the geometrical (Gaussian) image will be $\sim 2.076\ nm$. Here, d_s represents ~ 0.4 FWHM value of the beam wavefunction. So, for our simulations, the beam wavefunction is propagated from the virtual source at $z = 0$ to the specimen plane $z = z_{sp}$ to get the probe distribution. The last ray that passes through the second aperture A_2 and contributes to image formation makes an angle of $\alpha \approx 9.537\ mrad$ with the optical axis. All the simulations in the chapter are for beam energy $E = 10\ keV$, which corresponds to $\lambda \approx 1.22 \times 10^{-11}\ m$. The virtual source size parameter $d_s = 20\ nm$, the plane length/observation window $L_s = 30\ \mu m$ and $N = 4096$ pixels.

3.3 Simulation Experiments

3.3.1 *How to choose a propagator function ?*

The central idea to calculate the correct diffraction result is to sample in a way that we achieve a nonaliased propagator function. We mentioned earlier that the ASM propagator ($H_{ASM}(f_x,\ f_y)$) is a Fourier domain propagator and the RSC propagator ($h_{RSC}(x,y)$) is a spatial domain propagator. To get a more intuitive understanding of the propagator choice we need to understand sampling constraints on the phase function of these propagators. Spatial frequency is the rate of change of the phase. Nonaliasing is guaranteed when the sampling frequency is greater than or equal to twice the maximum spatial frequency. Mathematically that means, $|\frac{\partial\varphi(\Gamma)}{2\pi\partial\Gamma}|_{max} \leq \frac{1}{2\triangle\Gamma}$, where φ is the phase function and Γ is the independent variable. For H_{ASM} and h_{RSC}, φ would be $\varphi(f_x) = kz\sqrt{1-(\lambda f_x)^2}$ and $\varphi(x) = k\sqrt{x^2+z^2}$, respectively. We are using 1-D functions just for simplicity as they have the same behavior in x *and* y. For H_{ASM} if we satisfy the sampling inequality, we get $|\frac{\partial\varphi(f_x)}{2\pi\partial f_x}|_{max} \leq \frac{1}{2\triangle f}$, where $\triangle f = \frac{1}{2N\triangle x}$ is the pixel size in the Fourier domain. If we solve this inequality, we arrive at the condition for nonaliased propagation using H_{ASM} as $z \leq \frac{2N(\triangle x)^2}{\lambda}\sqrt{1-(\frac{\lambda}{2\triangle x})^2}$. Similarly, for h_{RSC} we get $|\frac{\partial\varphi(x)}{2\pi\partial x}|_{max} \leq \frac{1}{2\triangle x}$, where $\triangle x = \frac{L}{N}$ is the size of one pixel in the spatial domain. Solving this inequality, we get the condition for nonaliased propagation using h_{RSC} as $z \geq \frac{2N(\triangle x)^2}{\lambda}\sqrt{1-(\frac{\lambda}{2\triangle x})^2}$.

To ensure optimization of our choice for the propagator function we repeated the simulation experiment using three different scenarios. We implemented all the propagations using the ASM propagator, then the RSC propagator, and finally the combination of both (ASM + RSC). For (ASM + RSC) we used a cut-off distance $z_c = \frac{2N(\triangle x)^2}{\lambda}\sqrt{1-(\frac{\lambda}{2\triangle x})^2}$ discussed above for each propagation to choose between the two. For all propagation distance $z \leq z_c$ we used the ASM propagator and for $z > z_c$

we used the RSC propagator. Figure 3.5 shows that the ASM propagator was able to outperform the other two propagators. One way to understand this behavior would be the following: ASM is a Fourier domain propagator, and our object function is a Gaussian beam that doesn't have much high-frequency information because of its smooth nature and lack of sharp edges. Therefore, even with sampling that doesn't match the nonaliasing constraints, the ASM propagator performs relatively well. For the other two methods, the beam wavefunction phase at the specimen severally suffers under-sampling and retains poor phase accuracy compared to ASM propagator that can show the quadratic phase. This was also reflected in the wavefunction intensity, and it showed aliased peaks for RSC and (ASM + RSC) propagators. Therefore, for all our propagations in the simulations, we use the ASM propagator.

Simulation Experiment 1

Step 1: Initialize the beam wavefunction as a Gaussian function in the virtual source plane where d_s is the virtual source size $\rightarrow \psi = \psi_s(x_s, y_s) = \sqrt{e^{\frac{-({x_s}^2+{y_s}^2)}{{d_s}^2}}}$.

Step 2: Propagate ψ to the first aperture using a propagator function (ASM / RSC /ASM + RSC) and multiply the amplitude transmission $\rightarrow \psi_s(x_s, y_s)\ A_1(x_s, y_s)$.

Step 3: Propagate ψ to the condenser lens using a propagator function (ASM / RSC /ASM + RSC) and multiply the phase transmission $\rightarrow \psi_s(x_s, y_s)\ A_1(x_s, y_s)\ \varphi_{condensor}(x_s, y_s)$.

Step 4: Propagate ψ to the second aperture using a propagator function (ASM / RSC /ASM + RSC) and multiply the amplitude transmission $\rightarrow \psi_s(x_s, y_s)\ A_1(x_s, y_s)\ \varphi_{condensor}(x_s, y_s)$ $A_2(x_s, y_s)$.

Step 5: Propagate ψ to the front-focal plane of the objective lens using a propagator function (ASM / RSC /ASM + RSC) and take a Fourier transform to get ψ at the back-focal of the objective lens $\rightarrow \psi_f = FT(\psi_{-f})$.

Step 6: Rescale the spatial coordinates in back-focal plane $\rightarrow x_f = \lambda f_{objective} f_{xs}$,

$y_f = \lambda f_{objective} f_{ys}$.

Step 7: Finally propagate $\psi = \psi_f(x_f, y_f)$, δ distance to the geometrical (Gaussian) image plane using a propagator function (ASM / RSC /ASM + RSC) and rescale the coordinates $\rightarrow \psi = \psi_g(x_g, y_g)$ where, $x_g = y_f$, $y_g = y_f$.

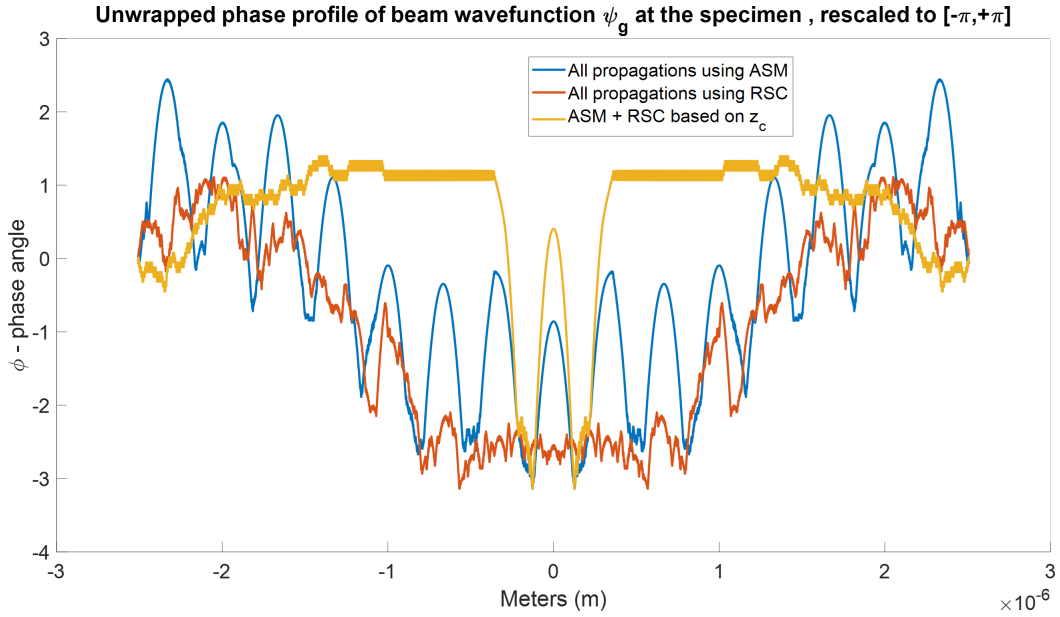

Figure 3.5: Electron beam wavefunction ψ_g phase profile at the geometrical (Gaussian) image plane. Phase profile compared for three propagators to model beam propagation in the SEM column

3.3.2 Plane-by-plane propagation: Objective lens as a phase transmission

Simulation Experiment 2

Step 1: Initialize the beam wavefunction as a Gaussian function in the virtual source plane where d_s is the virtual source size $\rightarrow \psi = \psi_s(x_s, y_s) = \sqrt{e^{\frac{-({x_s}^2+{y_s}^2)}{{d_s}^2}}}$.

Step 2: Propagate ψ to the first aperture using ASM propagator and multiply the amplitude transmission $\rightarrow \psi_s(x_s, y_s)\ A_1(x_s, y_s)$.

Step 3: Propagate ψ to the condenser lens using ASM propagator and multiply the

phase transmission $\rightarrow \psi_s(x_s, y_s)\ A_1(x_s, y_s)\ \varphi_{condensor}(x_s, y_s)$.

Step 4: Propagate ψ to the second aperture using ASM propagator and multiply the amplitude transmission $\rightarrow \psi_s(x_s, y_s)\ A_1(x_s, y_s)\ \varphi_{condensor}(x_s, y_s)\ A_2(x_s, y_s)$.

Step 5: Propagate ψ to the of objective lens using ASM propagator and multiply the phase transmission $\rightarrow \psi_s(x_s, y_s)\ A_1(x_s, y_s)\ \varphi_{condensor}(x_s, y_s)\ A_2(x_s, y_s)\ \varphi_{objective}(x_s, y_s)$.

Step 6: Finally propagate ψ , ($f_{objective} + \delta$) distance from the objective lens plane to the geometrical (Gaussian) image plane using ASM propagator to get $\psi = \psi_g(x_s, y_s)$.

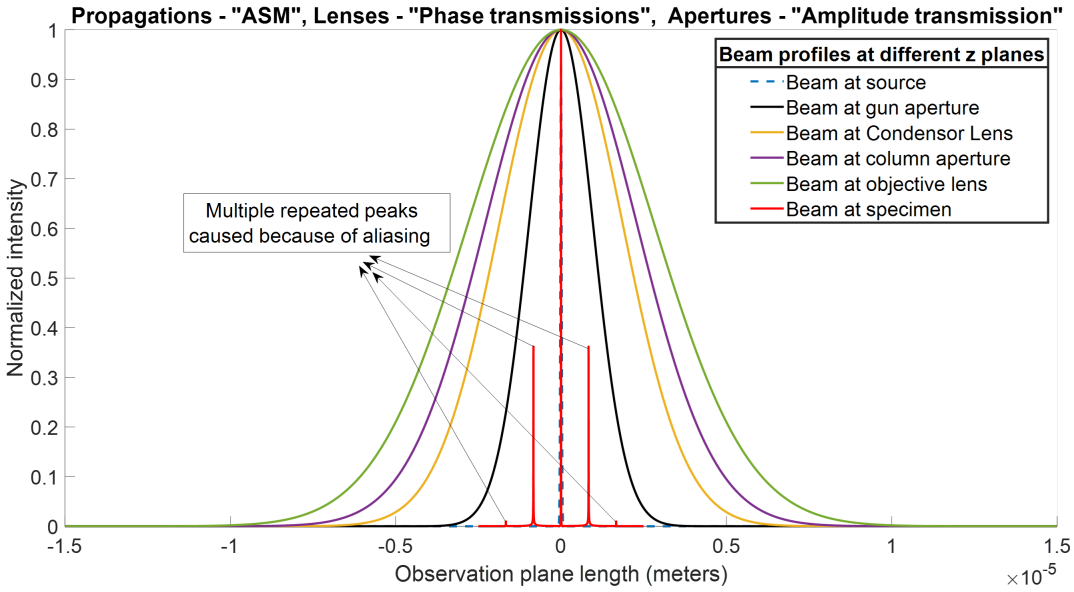

Figure 3.6: Profile plots of electron beam wavefunction intensity $|\psi|^2$ throughout the SEM column. It shows how beam width changes as it propagates from the virtual source plane to the specimen plane. The objective lens has been modeled as a phase transmission function. Ideally, the beam width should be the smallest at the specimen however, because of under-sampling we get an aliased beam image with multiple intensity artifact peaks.

Plane-by-plane propagation seems straightforward but is constrained by the digital nature of numerical diffraction calculation. Figure 3.6 shows that the beam slowly expands throughout the SEM column until the objective lens. The plane length/observation window for the beam is set in the virtual source plane to be $L_s = 30\ \mu m$. The value for L_s is chosen to be at least greater than the largest aperture diameter.

After the objective lens, the beam is focused on the specimen plane. Our optical setup has a geometrical demagnification of $M \approx 0.1038$, which means that all lengths in the virtual source plane are demagnified in the specimen plane. However, the conventional propagator functions do not allow a different plane length on the input and the output plane. This implies that simulation starts with $L_s = 30\ \mu m$ in the virtual source plane that is sampled by $N \times N = 4096 \times 4096$ pixels in x *and* y. One pixel size in the virtual source plane is $\triangle x = \triangle y = \frac{L_s}{N} = \frac{30\ \mu m}{4096} \approx 7.33\ nm$. The value of plane length and pixel size remains the same in the specimen plane, but the beam and all lengths are demagnified M times. This means that a 20 nm beam becomes $\sim 2.076\ nm$ in the specimen plane being represented by pixels that are larger than the beam. This under-sampling in the specimen plane gives rise to the aliased result shown in Figure 3.6, demonstrating why a plane-by-plane simulation fails. It is important to point out here that the bottleneck in the simulation was the objective lens modeling. The aliasing happens after the objective lens on the specimen plane because of the difference in plane lengths. The next two methods discussed solve this problem by modeling the optics of the objective lens and the propagation following it in different ways.

3.3.3 Plane-by-plane propagation: Objective lens as an optical Fourier transform

Simulation Experiment 3

Step 1: Initialize the beam wavefunction as a Gaussian function in the virtual source plane where d_s is the virtual source size $\rightarrow \psi = \psi_s(x_s, y_s) = \sqrt{e^{\frac{-({x_s}^2+{y_s}^2)}{{d_s}^2}}}$.

Step 2: Propagate ψ to the first aperture using ASM propagator and multiply the amplitude transmission $\rightarrow \psi_s(x_s, y_s)\ A_1(x_s, y_s)$.

Step 3: Propagate ψ to the condenser lens using ASM propagator and multiply the phase transmission $\rightarrow \psi_s(x_s, y_s)\ A_1(x_s, y_s)\ \varphi_{condensor}(x_s, y_s)$.

Step 4: Propagate ψ to the second aperture using ASM propagator and multiply the amplitude transmission $\rightarrow \psi_s(x_s, y_s)\ A_1(x_s, y_s)\ \varphi_{condensor}(x_s, y_s)\ A_2(x_s, y_s)$.

Step 5: Propagate ψ to the front-focal plane of the objective lens using ASM propagator and take a Fourier transform to get ψ at the back-focal of objective lens $\rightarrow \psi_f = FT(\psi_{-f})$.

Step 6: Rescale the spatial coordinates in back-focal plane $\rightarrow x_f = \lambda f_{objective} f_{xs}$, $y_f = \lambda f_{objective} f_{ys}$.

Step 7: Finally propagate $\psi = \psi_f(x_f, y_f)$ distance $'\delta'$ to the geometrical (Gaussian) image plane using ASM propagator $\rightarrow \psi = \psi_g(x_g, y_g)$ where, $x_g = \lambda(f_{objective}+\delta) f_{xs}$, $y_g = \lambda(f_{objective}+\delta) f_{ys}$.

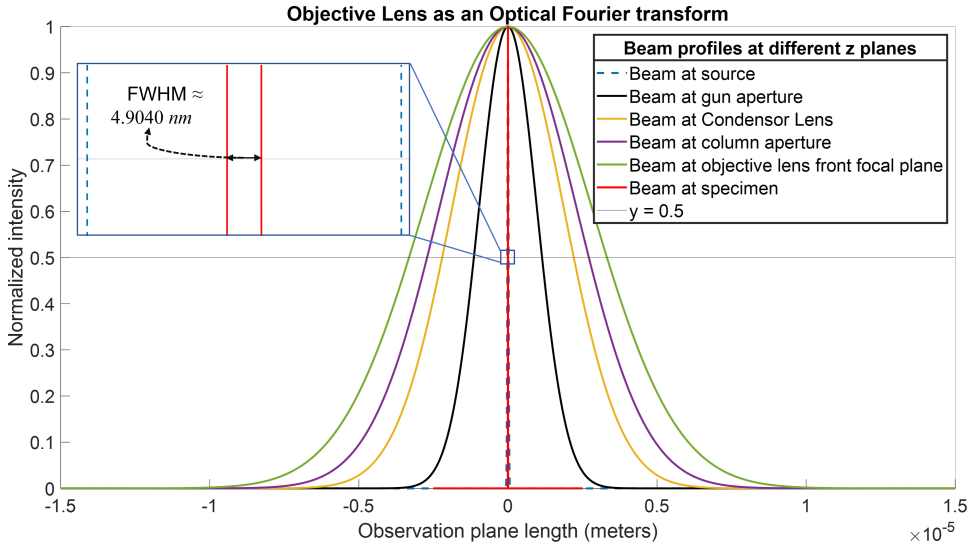

Figure 3.7: Profile plots of electron beam wavefunction intensity $|\psi|^2$ throughout the SEM column. It shows how beam width changes as it propagates from the virtual source plane to the specimen plane. The objective lens has been modeled as an Optical Fourier transform.

Exploiting the Fourier transforming action of a lens is one way to get around the aliasing problem we discussed in the previous simulation. For this simulation experiment, the wavefunction is propagated to the front-focal plane of the objective lens. Then we calculate the wavefunction in the back-focal plane using a Fourier transform

and rescale the coordinates in the focal plane. It is because of this rescaling and the Fourier property of the lens that we can get around propagating the field through the lens. Although this gives us a more reasonable spot size of the beam on the specimen plane, it is not ideal from a plane-by-plane implementation point of view. It would be difficult to add lens aberration as a phase transmission function in this implementation as the beam is not being propagated through the lens. Also, in scenarios where we want to place a phase mask for beam shaping at some z-plane, knowing the wavefunction throughout the column at all planes would be convenient. For this implementation, the Full-width-at-half-max (FWHM) value for the wavefunction intensity or the probe diameter is $\sim 4.9040\ nm$ as shown in Figure 3.7.

3.3.4 Plane-by-plane propagation: Objective Lens as Phase transmission followed by two-step Fresnel propagation

Simulation Experiment 4

Step 1: Initialize the beam wavefunction as a Gaussian function in the virtual source plane where d_s is the virtual source size $\rightarrow \psi = \psi_s(x_s, y_s) = \sqrt{e^{\frac{-({x_s}^2+{y_s}^2)}{{d_s}^2}}}$.

Step 2: Propagate ψ to the first aperture using ASM propagator and multiply the amplitude transmission $\rightarrow \psi_s(x_s, y_s)\ A_1(x_s, y_s)$.

Step 3: Propagate ψ to the condenser lens using ASM propagator and multiply the phase transmission $\rightarrow \psi_s(x_s, y_s)\ A_1(x_s, y_s)\ \varphi_{condensor}(x_s, y_s)$.

Step 4: Propagate ψ to the second aperture using ASM propagator and multiply the amplitude transmission $\rightarrow \psi_s(x_s, y_s)\ A_1(x_s, y_s)\ \varphi_{condensor}(x_s, y_s)\ A_2(x_s, y_s)$.

Step 5: Propagate ψ to the of objective lens using ASM propagator and multiply the phase transmission $\rightarrow \psi_s(x_s, y_s)\ A_1(x_s, y_s)\ \varphi_{condensor}(x_s, y_s)\ A_2(x_s, y_s)\ \varphi_{objective}(x_s, y_s)$.

Step 6: Finally propagate ψ, distance ($f_{objective} + \delta$) from the objective lens plane to the geometrical (Gaussian) image plane using two-step Fresnel propagator to get

$\psi = \psi_g(x_g, y_g)$ where, $x_g = My_s$, $y_g = My_s$ and $M \approx 0.1038$ is the geometrical demagnification.

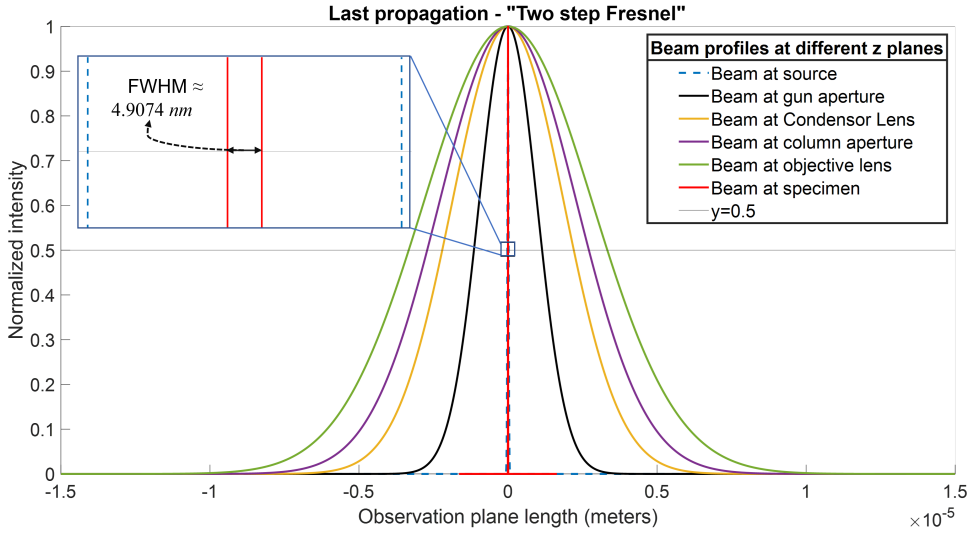

Figure 3.8: Profile plots of electron beam wavefunction intensity $|\psi|^2$ throughout the SEM column. It shows how beam width changes as it propagates from the virtual source plane to the specimen plane. The objective lens is modeled as a phase transmission followed by a two-step Fresnel propagation.

As mentioned above, a propagator function inherently assumes the same plane length (observation window) on the source and specimen plane. The flexibility of choosing different plane lengths is achieved using the two-step Fresnel propagator after the objective lens. This method enables plane-by-plane propagation that overcomes the under-sampling problem in the specimen plane without using the lens as Fourier transforms and produces a realistic result. It would be possible to place any phase object like an aberration function or beam-shaping mask anywhere in the column and observe the effect of it on the probe distribution in the specimen plane. The probe diameter from this method is $\sim 4.9074\ nm$ as shown in Figure 3.8.

3.3.5 Comparison and analysis of results

The geometrical picture of probe diameter calculation is dependent on the geometrical (Gaussian) image of the probe, diffraction, spherical, and chromatic aberrations. We use the root power sum (RPS) method [55] shown in the equation 3.3.9 which uses only $FW50$ (full-width at 50 % current value) diameters. For our simulations, all distributions are normalized so we consider $FWHM \approx FW50$. Other factors like coherence [4] and higher-order parasitic aberrations also affect the probe distribution.

$$d_{probe}^2 = \left\{ \left(d_{diffraction}^4 + d_{spher.\ \ aberr}^4 \right)^{\frac{1.3}{4}} + d_I^{1.3} \right\}^{\frac{2}{1.3}} + d_{chrom.\ \ aberr}^2 \qquad (3.3.9)$$

where $d_{diffraction} = \frac{0.66 \times 10^{-9}}{\sqrt{V}\,\alpha}$, with $V = 10\ KV$ *and* $\alpha \approx 9.537\ mrad$. For this analysis we have compared the results with the diffraction contribution $d_{diffraction}$ in the probe diameter without introducing any aberrations in the lenses. We treat the FWHM value as the beam diameter. For the virtual source size parameter $d_s = 20\ nm$, the wavefunction is $\psi = \psi_s(x_s, y_s) = \sqrt{e^{\frac{-({x_s}^2+{y_s}^2)}{{d_s}^2}}}$ and has a FWHM value of $d_{s|FWHM} \approx 47.2\ nm$. For $M \approx 0.1038$, the Gaussian probe diameter would be $d_{gaussian} = M d_{s|FWHM} \approx 4.9074\ nm$. The diffraction contribution is calculated as $d_{diffraction} = \frac{0.66 \times 10^{-9}}{\sqrt{10\times10^3}\,(9.537\times10^{-3})} \approx 0.692\ nm$

$$d_{probe|geometrical} = \sqrt{d_{gaussian}^2 + d_{diffraction}^2} \approx 4.956\ nm \qquad (3.3.10)$$

Therefore, both the wave methods produce a result very comparable to what was

Wave simulation Method	FWHM	$\triangle d_{probe}$
Lens using Optical Fourier Transform	$\sim 4.9040\ nm$	$\sim 0.051\ nm$
Two-step Fresnel propagator	$\sim 4.9074\ nm$	$\sim 0.048\ nm$

Table 3.2: Comparison of probe diameter of the wave simulation using different methods and their difference (Δd_{probe}) from the geometrical calculations.

expected from the geometrical picture. The small deviation might be an effect of the digital nature of the simulation. Figure 3.9 shows the convergence of both the wave methods with the geometrical theory. N was changed by keeping the L fixed and hence the highest spatial frequency changes. It is important to note that results from both wave methods start converging around the same spatial frequency which supports the equivalency of both methods. The outlier on the two-step propagator curve is a result of aliasing. In this case, there were multiple peaks formed in the specimen plane and the FWHM value is that of the central lobe. We have used the sampling frequency corresponding to $N = 4096$ in all our simulations as shown in Figure 3.9.

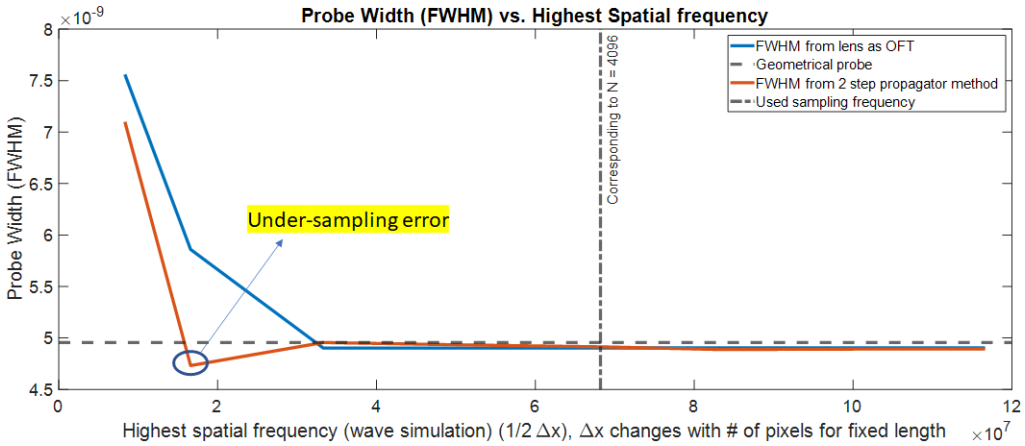

Figure 3.9: Convergence of the two wave methods. Both the wave methods produce similar probe widths and converge to the geometrical calculations. The highlighted point on the two-step propagator curve is an erroneous result caused because of aliasing. OFT stands for optical Fourier transform.

3.3.6 Plane-by-plane propagation Application: Effect of Aberration

Simulation Experiment 5

Step 1: Initialize the beam wavefunction as a Gaussian function in the virtual source plane where d_s is the virtual source size $\rightarrow \psi = \psi_s(x_s, y_s) = \sqrt{e^{\frac{-({x_s}^2+{y_s}^2)}{{d_s}^2}}}$.

Step 2: Propagate ψ to the first aperture using ASM propagator and multiply the amplitude transmission $\rightarrow \psi_s(x_s, y_s)\ A_1(x_s, y_s)$.

Step 3: Propagate *function* to the condenser lens using ASM propagator and multiply the phase transmission and the aberration mask function $\rightarrow \psi_s(x_s, y_s)\ A_1(x_s, y_s) \times \varphi_{condensor}(x_s, y_s)$ $t^{condensor}_{aberratoin}(x_s/r, y_s/r)$, where r is mask radius.

Step 4: Propagate ψ to the second aperture using ASM propagator and multiply the amplitude transmission $\rightarrow \psi_s(x_s, y_s)\ A_1(x_s, y_s)\ \varphi_{condensor}(x_s, y_s)\ \times$ $t^{condensor}_{aberratoin}(x_s/r, y_s/r)\ A_2(x_s, y_s)$.

Step 5: Propagate ψ to the of objective lens using ASM propagator and multiply the phase transmission and the aberration mask function $\rightarrow\ \varphi_{objective}(x_s, y_s)\ \times$ $t^{objective}_{aberratoin}(x_s/r, y_s/r)$.

Step 6: Finally propagate ψ, distance ($f_{objective} + \delta$) from the objective lens plane to the geometrical (Gaussian) image plane using two-step Fresnel propagator to get $\psi = \psi_g(x_g, y_g)$ where, $x_g = My_s$, $y_g = My_s$ and $M \approx 0.1038$ is the geometrical demagnification.

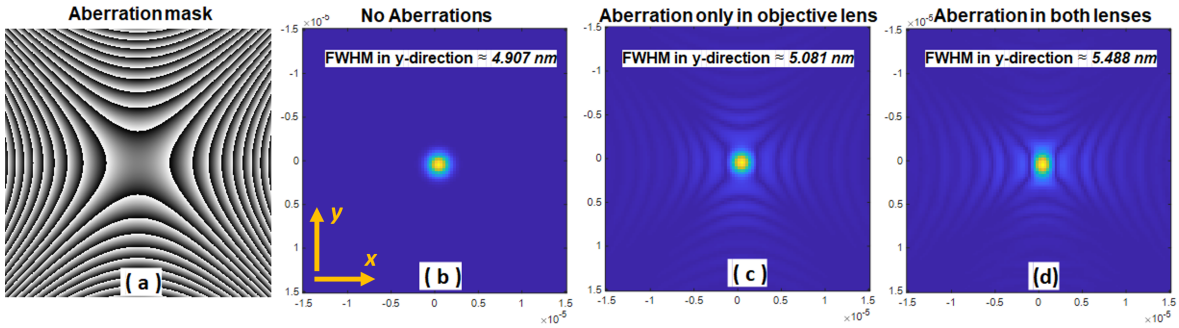

Figure 3.10: Visualizing the effect of aberration on the probe intensity. (a) Two-fold axial astigmatism aberration function, (b) Probe intensity with no aberrations in both the lenses, (c) Aberrated probe intensity with aberration present only in the objective lens, (d) Aberrated probe intensity with aberration present in the condenser lens and the objective lens.

Aberrations are present in all real lenses. We have chosen a simple two-fold astigmatism function to demonstrate how they affect the probe in SEM. The simulation experiment was run in three configurations: no aberration in both lenses, aberration only in the objective lens, and aberration present in both lenses. Astigmatism causes the beam to become elliptical and have more spread along a certain axis. Our choice of aberration function causes the beam to spread along the y-axis. Figure 3.10 shows the importance of having the capability of performing a plane-by-plane propagation through the lenses. In practice, the whole SEM column is reduced to the probe-forming objective lens. However, aberrations present in the condenser lens also affect the final probe. The probe in Figure 3.10 (d) has $FWHM \approx 5.488\ nm$ along the y-direction and the probe in Figure 3.10 (c) has $FWHM \approx 5.081\ nm$. These results support the fact that the combination of condenser and objective lens aberrations is the more accurate way of modeling probe formation. Such an approach can capture the effect of both the lenses and their aberrations. It also shows how aberrations can make the probe broader and hence deteriorate the final resolution.

In this chapter, we showed the modeling of an SEM optical column by establishing a step-by-step propagation method. We presented the first successful plane-by-plane propagation of the electron beam wavefunction from the source to the specimen assisted by the two-step Fresnel propagator method. The under-sampling problem arising in the specimen plane due to the objective lens demagnification was discussed and two wave optical methods were implemented to overcome it. We also showed that the wave optical methods produced similar probe diameters as predicted by the geometrical theory. Finally, we demonstrated one of the applications of our plane-by-plane propagation by studying the effect of the two-fold astigmatism on the final probe. This plane-by-plane propagation method can be applied to any probe-forming system to model propagation and probe formation. Adding more lenses, apertures, aberrations, phase

masks, etc. along the column will be very convenient using our implementation. This study can be used to explore other factors that affect the probe like partial coherence and noise. Another potential application worth exploring using our method could be the understanding of compound/electrostatic immersion lenses using wave optics.

Chapter 4

Aberration Diagnostics using Deep Learning

In Chapter 2 and Chapter 3 we discussed two wave optical models to represent the optics and probe formation in an SEM. In Chapter 2, we treated probe formation due to the action of an objective lens. In Chapter 3 we did not approximate the optical setup in anyway and used a *plane-by-plane* propagation model. In this chapter [1], we refine our definition of the optical setup by relying on the concept of an exit pupil. This chapter is a direct application of SEM-Nano. We have slightly modified the SEM-Nano program such that the equations are expressed in terms of a normalized coordinate system (Equations 4.1.2 and 4.1.3) described in the next section. This change gives us the ability to input the aberration coefficients in dimensions of length instead of $'number\ of\ \lambda s$'.

Aberration diagnostics in an uncorrected SEM is crucial to move towards an alternative way of aberration correction which is independent of the multipole correctors. Currently, there are no standard methods to quantify aberrations in an uncorrected SEM. Instead of trying to perfect the optics, another approach could be adaptive aber-

[1] The work shown in this chapter was done in collaboration with Harshkumar Prajapati

ration correction. The idea is to work with the imperfect optics and add a reconstruction step to shape the beam wavefront and negate aberrations. Even with the developments in dynamic shaping of electron beams [42, 43, 44, 45, 46, 47], we still require the ability to quantify aberrations in uncorrected SEMs. In this context, this work is focused on estimating aberrations using a neural network trained on modeled probe intensities [4] and testing its performance on test probe intensities.

4.1 Optical Setup

The SEM optical column is designed to form the smallest possible probe at the specimen plane. The final probe distribution depends on several factors like source distribution, diffraction from multiple apertures, aberrations from lenses, coherence, etc. In Schottky field-emission SEMs, the virtual source size is already much smaller than thermionic sources ($d_s \leq 20 - 25\ nm$) [79]. Therefore, to get a small probe the demagnification is performed mostly performed by the objective lens. However, this doesn't mean that the aberrations in other lenses don't affect the probe distribution which is often assumed. In cases where there are multiple lenses and apertures present (all in different planes), the system can be described using the action of an exit pupil. An exit pupil is an image of the limiting aperture in the column when viewed from the specimen plane into the optics. For paraxial beams, under the assumption of linearity and shift-invariance, probe formation can be described as the coherent imaging of the electron beam [4] as shown in equation Equation 4.1.1

$$\psi_{sp}(x_i, y_i) \ = h(x_i, y_i) \ \otimes \psi_g(x_i, y_i) \tag{4.1.1}$$

where (x_i, y_i) are the coordinates in the specimen plane, $\otimes$is the convolution operator, ψ_{sp} is the final probe wavefunction, ψ_g is the geometrical demagnification of the

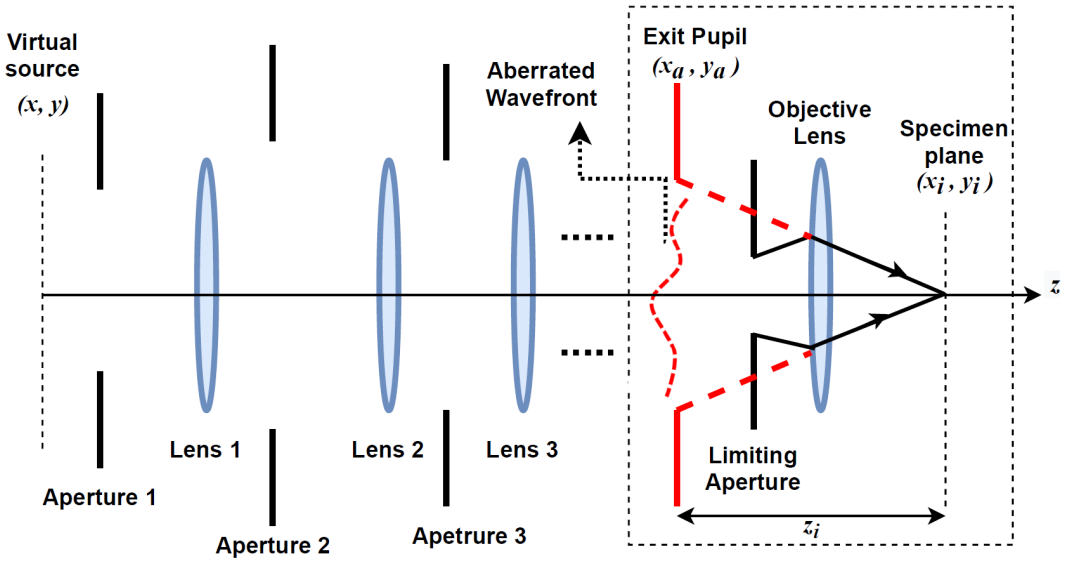

Figure 4.1: Schematic diagram of an arbitrary SEM column with multiple lenses and apertures. For linear and shift-invariant optical systems, their behavior can be modeled using the action of an exit pupil (projection of the smallest aperture in the column) as shown above.

source wavefunction, and $\psi_s(x,y) = e^{\frac{-(x^2+y^2)}{d_s}}$ is the coherent point spread function (h) defined in Equation (4.1.2) as the Fraunhoffer Diffraction of the exit pupil [80]

$$h(x_i, y_i) = \mathcal{F}\{ A(\frac{x_a}{z_i}, \frac{y_a}{z_i}) e^{-i\frac{2\pi}{\lambda}\varphi(\frac{x_a}{z_i}, \frac{y_a}{z_i})}\} \tag{4.1.2}$$

where $\mathcal{F}$ represents Fraunhofer diffraction, A is the image (projection) of the limiting aperture in the exit pupil plane (x_a, y_a), λ is the electron wavelength, and z_i is the distance between the specimen plane and the exit pupil. The specimen plane coordinates are related by the exit plane coordinates as $x_a = (\lambda z_i) f_x$, where f_x is the spatial frequency coordinate in the specimen plane.

For an ideal system, at the exit pupil, a spherical wavefront can be observed. However, for real SEM optics, aberrations present in the optical components make the wavefront deviate from a spherical shape at the exit pupil and hence the aperture function acquires a phase φ as shown in Equation 4.1.2. There are multiple existing

notations in the literature to represent wavefront aberrations in the exit pupil. We will use the notations [56, 108] shown in Equation (4.1.3)

$$\begin{aligned}\varphi(\omega) \;=\; \Re[\; \frac{1}{2}\,\omega\varpi\; C_1 \;+\; \frac{1}{4}\,(\omega\varpi)^2\; C_3 \;+\frac{1}{2}\,(\varpi)^2\; A_1 \;+\; \frac{1}{3}\,(\varpi)^3\; A_2 \\ +\omega^2\varpi\; B_2 \;+\frac{1}{4}\,(\varpi)^4\; A_3 \;+\; \omega^3\varpi\; S_3 \;+\; .....\;]\end{aligned} \tag{4.1.3}$$

where $\Re$ represents the real part, $\omega \;= \frac{x_a}{z_i} + i\frac{y_a}{z_i}$, $\varpi \;= \frac{x_a}{z_i} - i\frac{y_a}{z_i}$,
and $C_1,\; C_3/C_s,\; A_1,\; A_2,\; B_2,\; A_3, S_3$ are the aberration coefficients.

4.2 Machine Learning Elements

We use machine learning to predict aberration coefficients from a pair of probe intensity images by modeling it as a nonlinear regression problem. Machine learning models learn a functional mapping between the input and the output spaces and hence can be used for regression problems to learn a functional mapping between the dependent and independent variables. In our case, the input space is the set of all pairs of probe intensity images and the output space is the corresponding aberration coefficients. This functional map between the output and input spaces is learned by a training procedure. During the training process, the model is fed a set of known pairs of input and output data known as the training dataset. The model updates its parameters within an optimization framework to best fit this training dataset. Its performance is then evaluated on a set of unseen pairs of input and output data known as the test dataset. A machine learning model is said to be good if its performance on the test dataset is comparable to the performance on the training dataset.

4.2.1 Range of aberration coefficients

Standard methods for aberration diagnostics are available in transmission electron microscopes (TEM) and scanning transmission electron microscopes (STEM) [32, 82] and the range of aberration coefficients are well-known [56, 108]. Some methods do exist for the measurement of aberrations in aberration-corrected SEM [34, 109]. There also have been studies about the values of individual coefficient ranges (C_3/C_s, C_c) [110, 65]. As far as we know, no standard range of aberration coefficients for the uncorrected SEM is reported in the literature.

We use the aberration coefficient range for SEMs based on the SEM Nano simulation [4] shown in Table 4.1. The set of these values would form a superset of the actual values, which makes them pivotal for broader training of CNN. The actual values in a well-aligned SEM might have a smaller range.

Aberration Coefficients	Min. value	Max. value
$C_1 - \ Defocus$	$-2\ \mu m$	$2\ \mu m$
$C_3/C_s\ -\ 3^{rd}\ order\ spherical$	$0\ mm$	$600\ mm$
$A_1\ -\ 2\ fold\ axial\ astigmatism$	$-3\ \mu m$	$3\ \mu m$
$A_2\ -\ 3\ fold\ axial\ astigmatism$	$-2.3\ mm$	$2.3\ mm$
$B_2\ -\ 2^{nd}\ order\ axial\ coma$	$-2\ mm$	$2\ mm$
$A_3\ -\ 4\ fold\ axial\ astigmatism$	$-400\ mm$	$400\ mm$
$S_3\ -\ 2\ fold\ astigmatism\ of\ C_s$	$-300\ mm$	$300\ mm$

Table 4.1: Range of aberration coefficients used for training the CNN.

For instance, in Table 4.1 the upper limit for the value of C_3/C_s is 600 mm which seems rather large. But the resolution limit for C_3/C_s is $r(C_s) = \sqrt[4]{0.12\ C_s\ \lambda^3}$. So for a typical value of like $\lambda = 8.5\ pm$, $r(C_s)$ is still just $\sim 2.5\ nm$. For weak lenses that are used in SEMs when coupled with larger working distances, $C_3/C_s = 20 - 100\ mm$ [65], which is still a subset of the range used for training.

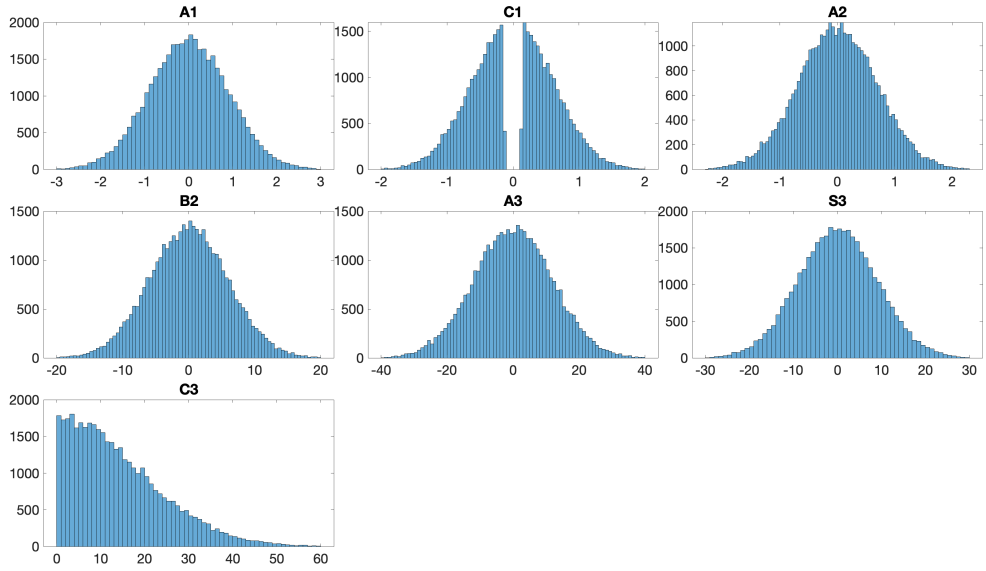

Figure 4.2: Distribution functions of individual coefficients used in training.

4.2.2 Training and Test Data

We use SEM Nano to simulate $40,000$ pairs of parasitic aberration coefficients and the corresponding probe intensity image pair (in-focus and defocused). The defocused image is generated by adding $C_1 = 2\ \mu m$ to the aperture phase function. The aberration function is a linear combination of even and odd functions. Therefore, the problem of predicting the coefficients using a single probe intensity image is ill-posed. For instance, the effect of negative and positive defocus on the probe diameter is the same as the basis function for defocus ($\omega\varpi$) is even. This means, that given just a single probe intensity image with defocus, it is impossible to accurately predict whether the probe was produced with negative or positive defocus. That is the reason we use the image pair (in-focus and defocused) in the pipeline to train and test the network.

60% of the $40,000$ data samples were used to train the CNN, and were 15% used for validation during training. The remaining 25% was used as the test data. For each aberration coefficient, the values were sampled from a Gaussian distribution with

mean value $\mu = 0$; and standard deviation $\sigma = 0.3$ of their maximum value shown in Table 4.1. Distributions used for generating the individual aberration coefficients. As there is always some unavoidable amount of defocus present in the probe, we have only considered non-zero values of C_1. Furthermore, it is known that electron lenses have positive spherical aberration so the distribution corresponding to only has C_3 non-negative values. The distribution for all coefficients are shown in Figure 4.2.

4.2.3 Convolutional Neural Network

We have used a convolutional neural network (CNN) as our machine learning model to predict the aberration coefficients from a pair of probe intensity images. CNNs are a class of artificial neural networks that have been widely used by the computer vision community. Their ability to learn spatial hierarchical features from raw data and use parameter sharing to reduce the number of learnable parameters make them highly successful on image-based tasks. Due to their proven success on image data, they have also been used to address imaging problems in both optical [111] and electron microscopy[112, 113, 114, 115].

Over the years several CNN architectures have been proposed with varying complexity. The choice of architecture depends upon the type and complexity of the task at hand, the size of the dataset, and computational resources. Typical computer vision datasets have millions of training samples and hence use complex CNN architectures. Since we have only training samples we use a vanilla CNN with 9 blocks (see Figure 4.3).

Out of the 9 blocks, the first 6 blocks are convolutional. Each block consists of a *2-D* convolutional layer followed by a *Leaky ReLU* activation layer. The *2-D* convolutional layer consists of many kernels or filters that are convolved with the input image or the output of the previous layers (depending upon the position of the block). The output

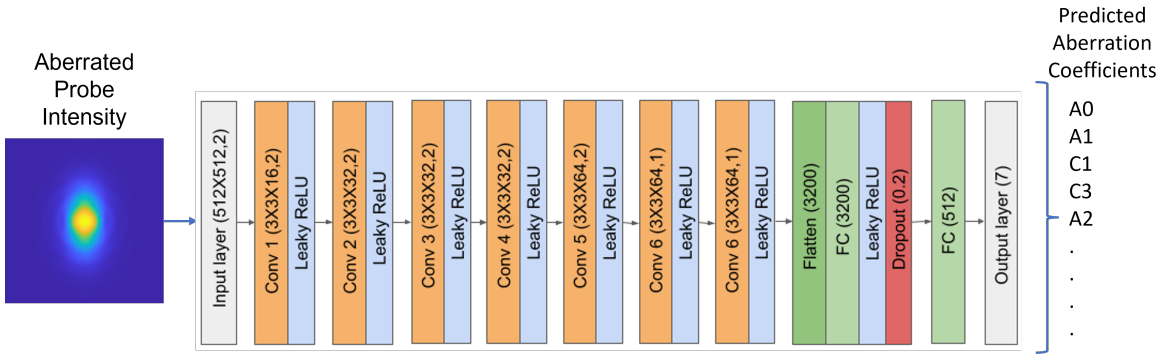

Figure 4.3: Convolutional neural network (CNN) architecture used for training on the generated dataset of aberrated probe intensities.

after the application of each of these kernels is known as a feature map as it represents the features extracted by the kernels. The weights of these kernels are updated during the training process, and they determine the types of features learned by these kernels. The feature maps are passed through a *ReLU* activation layer. *ReLU* activation keeps the positive values in the feature map as it is and clips the negative values to zero. This introduces non-linearity in the training process. The features extracted by the kernels keep getting more complex with each block. In the initial block, the feature maps consist of simple features such as edges and textures as the kernels are directly convolved with the input image. In the later blocks they consist of complex hierarchical features as the kernels here are convolved with the feature maps obtained from the previous block. The output of the last convolutional block is flattened to a vector and passed to the penultimate block. The penultimate block consists of a fully connected layer followed by a *Leaky ReLU* and dropout layer. The last block consists of a fully connected layer whose output is a vector representing the aberration coefficients. Since, we want the network to predict only non-negative values for C_s/C_3, we have a *ReLU* activation for the last element of our output vector. In a fully connected layer, each neuron is connected to all the neurons of the previous layer. Thus, the output of each neuron is the weighted average of all the neurons in the previous layer. The weights in this weighted

average are updated during the training process. Due to these dense connections, a fully connected layer greatly increases the complexity (number of parameters of the model) of the CNN. This can lead to the CNN overfitting the training data and performing poorly on the test data. Hence, we use a dropout layer after the first fully connected layer. The dropout layer drops the neurons in the previous layer with a probability p. Thus, it acts as a regularizer and prevents overfitting.

4.2.4 Training

Each iteration of training can be divided into two phases - forward pass and backward pass. During the forward pass, a set of input images from the training data (batch of training data) is fed to the CNN. For each input image in the batch, the convolutional blocks extract features from the image. The fully connected blocks regress over these features and predict the corresponding aberration coefficients. The predicted coefficients are compared with the ground truth coefficients and an error also known as loss in machine learning is computed. This is done in parallel for all the images in the batch and a mean batch loss is computed. Now during the backward pass, this mean batch loss is backpropagated and the weights in each layer are updated. The magnitude of the weight updates is proportional to the learning rate. The greater the learning rate, the greater the change in weights. In each iteration, a different batch of training data is fed to the CNN. When all the training data is covered it is known as an end of an epoch. The CNN is trained for many epochs and the loss is expected to go down with each epoch. The training is stopped when the loss is reasonably low and the change in loss with epoch has stagnated. The batch size, number of epochs, and the learning rate are called hyperparameters and are fine-tuned by us. We train our CNN for 200 epochs with a batch size of 128. We change our learning rate with each epoch and hence use OneCycleLR [116] as our learning rate scheduler. The learning rate begins with 0.001

and increases with each epoch until it reaches 0.01 and then it starts decreasing with each epoch and reaches 0.0001 at the end of 200 epochs. We use the normalized mean square error ($nMSE$) between the predicted and the ground truth aberration coefficients as the error metric. The average of this $nMSE$ over the entire training data is used as the loss function. Since the order of magnitude and range of each aberration coefficient is different, we re-scale all the aberration coefficients between -1 to 1 before computing the $nMSE$. Figure 4.4 shows the training and validation loss after $30k$ iterations.

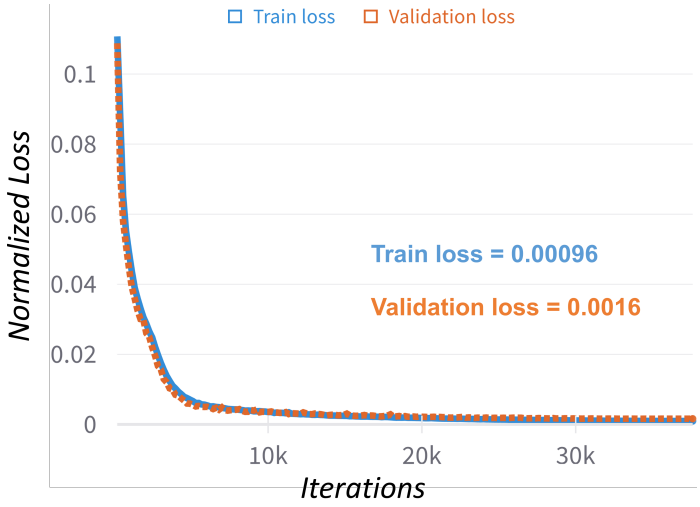

Figure 4.4: Training and validation loss minimization after $30k$ iterations.

4.3 Results

The goal for this work is to lay down and explain a step-by-step method of aberration diagnostic based on deep learning. To evaluate the performance of the trained network we show the distribution of the predicted coefficients and the prediction error (root mean square error - $RMSE$) of individual coefficients (see Figure 4.5). The network performed well on the test data and the final loss ($nMSE$) on the test dataset was ~ 0.001693.

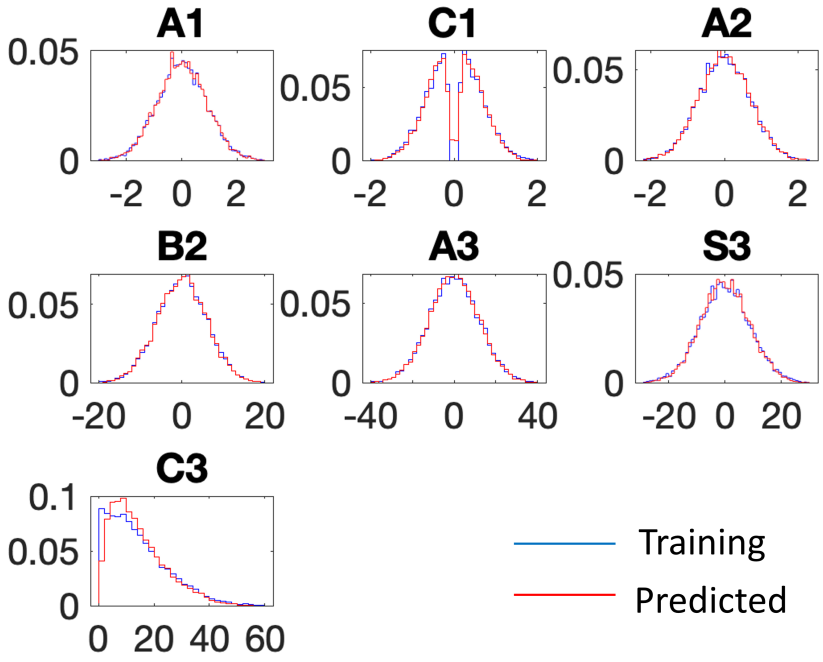

Figure 4.5: Distribution of the predicted aberration coefficients on the test dataset compared to the distribution used for training. The prediction error ($RMSE$) for all the coefficients is shown in Table 4.2.

Aberration Coefficients	Min. value	Max. value	Prediction Error
$C_1 - Defocus$	$-2\ \mu m$	$2\ \mu m$	$0.1164\ \mu m$
$C_3/C_s - 3^{rd}\ order\ spherical$	$0\ mm$	$600\ mm$	$31.8\ mm$
$A_1 - 2\ fold\ axial\ astigmatism$	$-3\ \mu m$	$3\ \mu m$	$0.06766\ \mu m$
$A_2 - 3\ fold\ axial\ astigmatism$	$-2.3\ mm$	$2.3\ mm$	$0.065686\ mm$
$B_2 - 2^{nd}\ order\ axial\ coma$	$-2\ mm$	$2\ mm$	$0.037455\ mm$
$A_3 - 4\ fold\ axial\ astigmatism$	$-400\ mm$	$400\ mm$	$10.4\ mm$
$S_3 - 2\ fold\ astigmatism\ of\ C_s$	$-300\ mm$	$300\ mm$	$13.8\ mm$

Table 4.2: Table to show prediction error of the trained network for individual coefficients on the test dataset.

Apart from the prediction error and test loss, it is equally important to evaluate the efficacy of the method on its final goal, which is aberration correction. We have discussed two main results in this section — (1) probe aberration correction and as a result of that, (2) the resolution enhancement in the final image.

4.3.1 Aberration Correction

Aberrations in the optics cause the probe to deviate from circular symmetry and broaden in size, to reduce in peak value, and gain irregularities on the surface. All these changes degrade the quality of imaging. To present a juxtaposition, we evaluate the correction based on three metrics which are size, peak value, and smoothness.

To compare size we compare the profiles before and after the correction of the probe. At first we show the comparison for an example image (see Figure 4.6) and then report the results for the test dataset. The aberrated probe might not be symmetric in all directions, therefore we compare the profiles for four different directions (0°, 45°, 90°, 135°). For the example image, comparison of profile widths (d_{59}) [56] in all directions before and after correction is shown in Table 4.3.

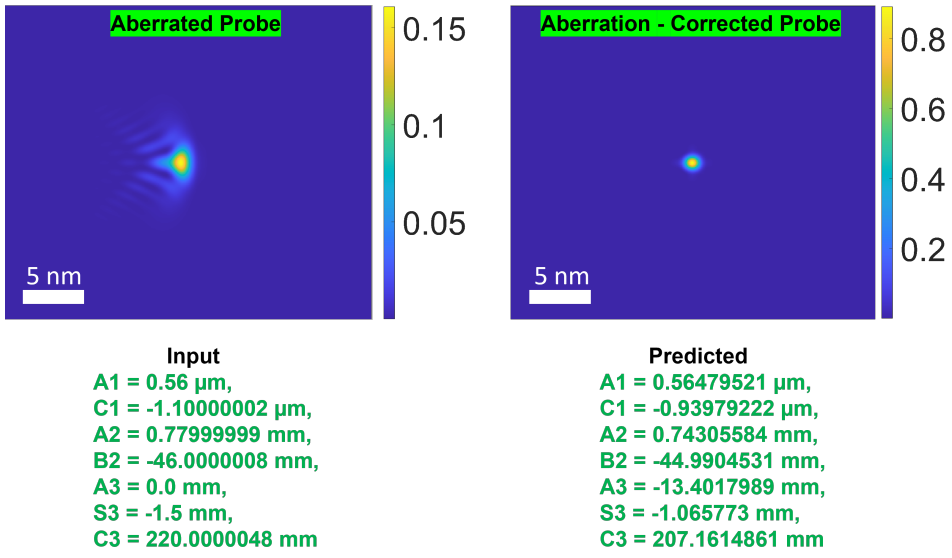

Figure 4.6: (left) Aberrated probe intensity shown with the aberration values present in the exit pupil, (right) Corrected probe intensity shown with the predicted aberration coefficients used to construct the inverse wavefront function. Reduction in probe width is shown in Table 4.3. The corrected probe peak value was ~ 0.8 compared to ~ 0.18 in the aberrated probe, showing an improvement of $\sim 4.46\times$. The asymmetry in the probe was also corrected and there was a $2.68\times$ reduction in total variation, which implies that the corrected probe was much smoother. Here $\lambda = 8.5\ pm$ for beam energy $20\ keV$.

Direction	Before (d_{59})	After (d_{59})
0°	3.125 nm	1.1719 nm
45°	1.935 nm	0.7812 nm
90°	3.125 nm	1.1719 nm
135°	1.757 nm	0.7812 nm

Table 4.3: Probe width comparison in four directions for aberrated and aberration corrected probe example.

Here we have defined d_{59} as the diameter which contains 59% of the total probe intensity that has been re-scaled to $[0, 1]$. For peak and smoothness comparison we compare the peak value and the total variation (TV) in the unnormalized probe images respectively. Total variation is the sum of absolute value of the derivative of an image X and is defined as the $L_1 - norm$ of the gradient: $TV(X) = ||\nabla I||_i = \sum |\nabla I_i|$.

Aberration correction on the test data

On average, the network was able to correct the effects of aberrations in the probe effectively. The peak value ratio was $\frac{peak_{corrected}}{peak_{aberrated}}|_{avg.} = 5.0125$, which implies that corrected probe was $\sim 5\times$ more intense than the aberrated probe. The corrected probe was $3.6974\times$ smoother than the aberrated probe as shown by the ratio of total variation; $\frac{TV_{aberrated}}{TV_{corrected}}|_{avg.} = 3.6974$. Similarly with probe width, there was an overall reduction observed in d_{59} in all four directions. The average reduction ($\frac{d_{59-aberrated}}{d_{59-corrected}}|_{avg.}$) in 0°, 45°, 90°, 135° profiles were $2.5512\times$, $2.5360\times$, $3.4171\times$, $2.5281\times$ respectively.

4.3.2 Image resolution enhancement

For the image resolution comparison, we have used a reference BSE image of a gold-nanoparticle ($Au\text{-}NP$) with a diameter of 28.5 nm. The reference image represents the ideal object structure which is blurred by the aberrated probe intensity. It was generated in CASINO [78, 59] with no noise, no aberrations, and probe diameter set to 0.1 nm ($\sim \delta - function$). Comparison of the images and profiles for the reference

image (object), the aberrated image, and the aberration-corrected image are shown as an example in Figures 4.7 and 4.8 respectively. The metric used for comparing resolution enhancement is the full-width-at-haltf-max (FWHM) comparison of the particle profile.

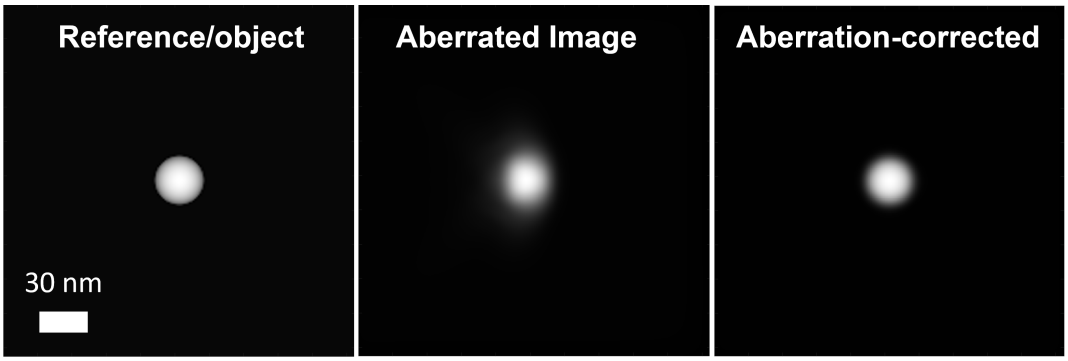

Figure 4.7: Effect of aberration correction on image resolution. (left) Ideal/reference BSE image of a single *Au-NP* generated in CASINO and rescaled to $[0, 1]$, (center) Image of a *Au-NP* when captured using a aberrated probe intensity, (right) Image of a *Au-NP* when captured using a aberration-corrected probe. The probes (aberrated and corrected) used for this demonstration were shown in Figure 4.6.

.

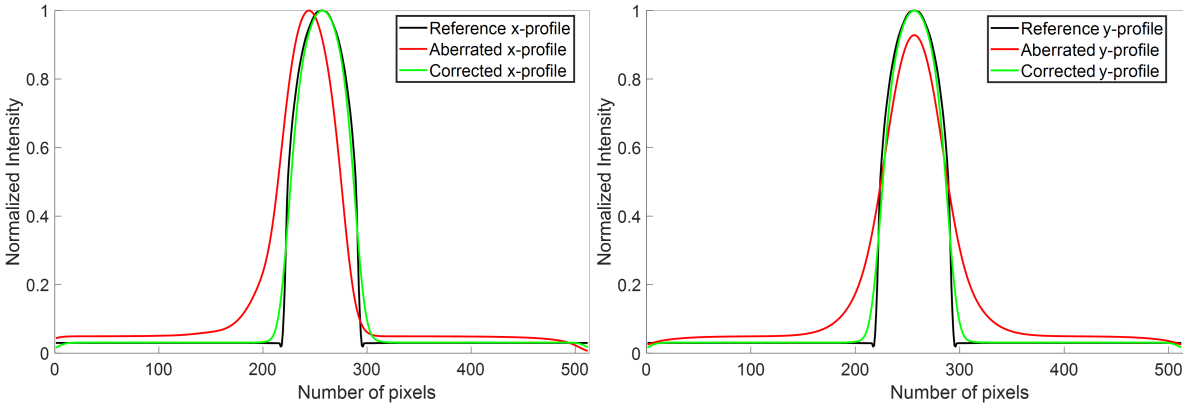

Figure 4.8: Profile comparison to show the change in resolution. (left) x-profile, (right) y-profile.

In Figure 4.8, the x-profile shows that the aberrated image was slightly shifted but the peak and width values are still comparable to the reference x-profile. Therefore the corrected x-profile is more close to the reference x-profile and the shift was corrected. For the y-profile, a reduction in peak value (0.928) and increase in FWHM value was

	x_{FWHM}	y_{FWHM}
Reference/Object	25.5176 nm	25.5176 nm
Aberrated	23.8185 nm	26.6953 nm
Aberration-corrected	23.5547 nm	23.447 nm

Table 4.4: FWHM comparison for *Au-NP* profiles.

observed. Both the effects were diminished during the correction process which can be seen in the corrected y-profile. A comparison of the FWHM values for the profiles is shown in Table 4.4.

In this chapter, we presented a machine learning technique for fast and simple aberration diagnostics in an uncorrected SEM using just two aberrated probe intensity images. A convolutional neural network was trained on a dataset of $24,000$ aberrated probe intensity images, generated using the SEM Nano simulation [4]. The network was trained to predict the first seven aberration coefficients ($C_1,\ C_3/C_s,\ A_1,\ A_2,\ B_2,\ S_3,\ A_3$) present in the probe, given the probe intensity and its defocused version. The performance of the trained network was shown for simulated unseen data. An average $\sim\ 3-fold$ reduction in the probe width, $\sim 5\times$ gain in the peak value, and ~ 3.7 reduction in total variation was observed on the simulated test data set. A quantifiable gain in image resolution was also demonstrated on a test image. This method will be greatly beneficial for real-time aberration diagnostics and automation of the aberration correction process.

Chapter 5

Electron Probe Phase Retrieval

Chapter 2 and Chapter 3 were dedicated to the wave-optical modeling of the SEM column and Chapter 4 was a direct application of SEM-Nano [4] (Chapter 2). This chapter is focused on the experimental part of the dissertation, where the importance of the wave-optical description is experimentally realized.

5.1 Phase Retrieval

Phase retrieval is one of the most interesting problems in physics and optics. It has found fundamental applications in a wide number of areas like X-ray crystallography [117], astronomical imaging [118, 119], microscopy [120], etc. In the field of electron microscopy, the study of phase retrieval methods and the phase information itself have been extensively exploited to produce excellent results over several decades in TEM and STEM [121, 122, 123, 124, 125].

Statement: For a complex function $\psi(\alpha) = |\psi(\alpha)|e^{i\phi(\alpha)}$, given only its magnitude $|\psi(\alpha)|$, can we recover its phase $\phi(\alpha)$?

Here α can be a variable of the real domain or the conjugate (Fourier) domain depending on the problem definition. This is an ill-posed inverse problem as multiple solutions can exist. Typically, there are various known constraints applied to the data in both

domains to guide the solution to a close approximation of the actual phase.

Broadly speaking phase retrieval can be performed using interferometric techniques like digital holography [126, 127], pytchography [128, 129, 130], etc., or non-interferometric techniques [131]. The work discussed in this chapter focuses on phase retrieval based on non-interferometric phase retrieval only.

5.1.1 Non-interferometric phase retrieval

Non-interferometric phase retrieval refers to recovering the lost phase of an object using single or multiple-intensity measurements [131]. Some techniques can recover phase using a single intensity measurement such as the Gerchberg-Saxton algorithm [80, 131], the hybrid input-output algorithm [80, 131], etc. Often with single-intensity-based phase retrieval, the magnitude measurement is done in the Fourier space. So the problem is defined as the reconstruction of an object function given the magnitude of its Fourier transform.

However, that is not the case with multiple-intensity measurements-based phase retrieval. The goal is to capture the phase information diversity between the measurements. What is being captured is the phase difference required to match the measured ground-truth intensities. Controlled defocus [121, 7] near a focal plane is one of the most popular techniques for multiple-intensity-measurement phase retrieval because of its simplicity. We choose to use the defocus diversity-based phase retrieval method because it is relatively easier to perform in an SEM. We describe the experiment in Section 5.3.

5.2 Phase retrieval problem for the SEM

Modern field-emission SEMs are equipped with highly coherent electron sources therefore a wave optical description of probe formation becomes essential [65]. Figure 5.1

shows a typical lens setup for an SEM. Probe-forming optics consist of the electron gun, multiple apertures, and multiple lenses. The probe wavefunction at the specimen can be expressed as a function of the virtual source distribution, coherence, aperture diffraction, and the wavefront aberrations [4]. For the coherent case,

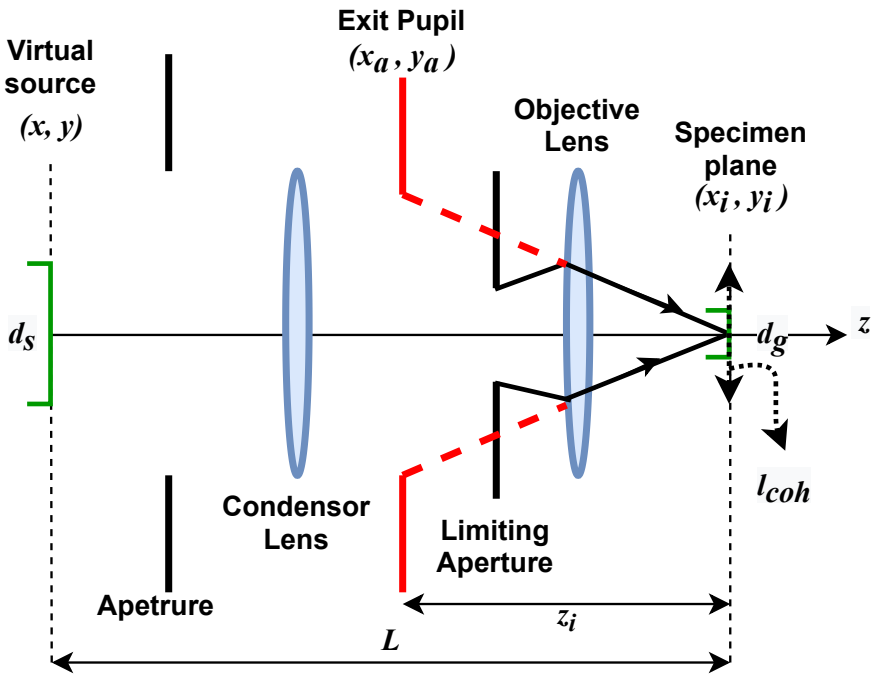

Figure 5.1: Optical setup for an arbitrary SEM column showing probe formation. The linearity and shift-invariance property allows the system to be represented using the exit pupil. The exit pupil is the image of the limiting aperture viewed from the specimen plane into the optics.

$$\psi_{sp}(x_i, y_i) \ = h(x_i, y_i) \ \otimes \psi_g(x_i, y_i) \tag{5.2.1}$$

where $\otimes$ represents convolution, (x_i, y_i) are the coordinates in the specimen plane, $\psi_g(x_i, y_i)$ is the geometrical demagnification of the virtual source wave function $\psi_s(x, y) = e^{\frac{-(x^2+y^2)}{d_s}}$ in the specimen plane, $h(x_i, y_i)$ is the coherent point spread function of the optics ($PSF^{\ coh}_{optics}$) in the specimen plane, and d_s is the width parameter of the virtual

source. The PSF_{optics}^{coh} is defined as,

$$h(x_i, y_i) \;=\; \mathcal{F}\,\{\, A(\frac{x_a}{z_i}, \frac{y_a}{z_i})\; e^{-i\frac{2\pi}{\lambda}\,\varphi(\frac{x_a}{z_i},\,\frac{y_a}{z_i})}\} \tag{5.2.2}$$

where $\mathcal{F}$ represents Fraunhofer diffraction [80], A is the image (projection) of the limiting aperture in the exit pupil plane, (x_a, y_a) are the coordinates in the exit pupil plane, z_i is the distance between the exit pupil and the specimen, λ is the relativistic electron wavelength. The exit pupil plane coordinates are related to the specimen plane coordinates as $x_a = (\lambda z_i) f_x$, where f_x is the spatial frequency coordinate in the specimen plane and similarly for y_a. The phase φ in Equation (5.2.2) represents the wavefront aberrations present in the exit pupil which causes the final probe wavefunction to acquire a complex phase. For the incoherent case,

$$|\psi_{sp}(x_i, y_i)|^2 \;= |h(x_i, y_i)|^2 \;\otimes |\psi_g(x_i, y_i)|^2 \tag{5.2.3}$$

where $PSF_{optics}^{incoh} = \;|h(x_i, y_i)|^2$ is the incoherent point spread function of the optics.

As the beam information (intensity and phase) is lost in the imaging process, estimating the aberrated wavefront becomes a challenging task. Information about the aberrated wavefront can be derived from the accurate measurement of the point-spread function of the probe-forming optics. Secondly, SEM performance is often described in terms of probe diameter which is unrealistic and simplistic. An accurate characterization of any optical system is pivotal to understanding and improving its performance. Hence, another crucial application of measuring the PSF_{optics}^{coh} is establishing a resolution metric for the SEM optics in the Fourier space using a transfer function. Therefore recovering the electron beam phase is crucial. Again, the phase problem for SEM images seems absurd because the image formation process doesn't involve imaging the transmitted exit wave. However, the phase we are concerned about is the optical phase

of the quantum wavefunction which describes the electron beam. Therefore, for phase retrieval, our object is the electron beam itself.

5.2.1 Coherence

Coherence is one of the most fundamental concepts of physics. General discussions on the topic are widely available in the literature [132, 133, 105]. In electron optics, realistically all field-emission sources have partial coherence [134, 135, 136]. Even thermionic electron sources, which were thought to be incoherent, exhibit partial coherence [137]. So all the point-spread functions for the probe forming optics can be thought to be on a spectrum between the $PSF\ {}^{coh}_{optics}$ and $PSF\ {}^{incoh}_{optics}$, depending on their varying degree of source coherence. There are numerous approaches to incorporate the effects of partial coherence on the electron probe [75, 138, 139]. For partially coherent sources, the fields vibrate in unison at a distance over a finite length, defined as the coherence length l_{coh}. Over this length, waves originating from different points on the source or waves of slightly different wavelengths, show interference. Spatial/transverse coherence length at a distance L is $l_{coh}^{spatial} = \frac{\lambda L}{\sqrt{2d_s\pi}}$ and the temporal/longitudinal coherence length is $l_{coh}^{temporal} = \frac{2\lambda E}{\triangle \mathrm{E}}$ where, $\triangle E$ is the spread in beam energy in eV. For $E = 20\ keV$ ($\lambda \approx 8.5\ pm$), $d_s = 20\ nm$, $\triangle E = 0.7\ eV$ and SEM column length $L \approx 300\ mm\ to\ 400\ mm$; $l_{coh}^{spatial} \approx 4.0585\ nm\ to\ 5.4113\ nm$ and $l_{coh}^{temporal} \approx 485.71\ nm$. Typically, SEM optics easily have a theoretical demagnification of $\sim 10\times$, and for all Schottky field-emission sources $d_s \leq 20\ nm\ to\ 25\ nm$. This corresponds to a geometrical image of the probe with width $d_g \leq 2\ nm\ to\ 2.5\ nm$ which is smaller than the $l_{coh}^{spatial}$. Therefore, our treatment of probe formation based on the coherent point-spread function $h(x_i, y_i)$ is well within reason.

5.2.2 Probe intensity determination

This process was already explained in Chapter 1 but is repeated here for continuity. To calculate $h(x_i, y_i)$, we solve the inverse problem in Equation 5.2.1, and hence the complete description of probe wavefunction ψ_{sp} is needed. We use the AURA software [58] as described by Zotta, Nevins *et al.* [6] for reconstructing the probe intensity $|\psi_{sp}|^2$. The experiments were done on a TESCAN MIRA3 SEM equipped with a Schottky field-emission source (virtual source size; $d_s = 20\ nm$). The process begins by capturing back-scattered electron (BSE) images of well-dispersed 28.5 nm gold (Au) nanoparticles (NPs) on a thin ($\sim$ 20 nm) carbon (C) film in a field-of-view (FOV) of 2048 nm $\times$ 2048 nm. Then all the individual NPs in the FOV are segmented and stacked together to get a high signal-to-noise ratio and generate a realistic image of a single NP ($\mathcal{I}_{real}$). Following that an ideal image/object structure ($\mathcal{I}_{ideal}$) is generated using the Monte-Carlo simulation CASINO, based on the material composition, size, and shape of the object and ideal imaging conditions; that is no aberrations and no noise. The probe intensity is known to blur the object structure to produce a real image in the SEM; $\mathcal{I}_{real} = \mathcal{I}_{ideal} \otimes |\psi_{sp}|^2$. Therefore, a simple Wiener-filter-based deconvolution ($K = 3162$) [140] yields the probe intensity. This whole process is summarized in Figure 5.2.

5.3 Defocus diversity experiment

As mentioned above, we have used the TESCAN MIRA3 SEM with a beam energy of 20 keV to perform this experiment. The electron probe was focused on a $z - plane$ to record an in-focus ($\Delta z = 0$) backscattered electron (BSE) image of 28.5 nm Au-NP. Then the specimen was moved with a z step size of $\sim$ 1 μm to record under-focused and over-focused images, as shown in Figures 5.3 and 5.4. Then the probe intensity distributions for each of these images were reconstructed using the method described in

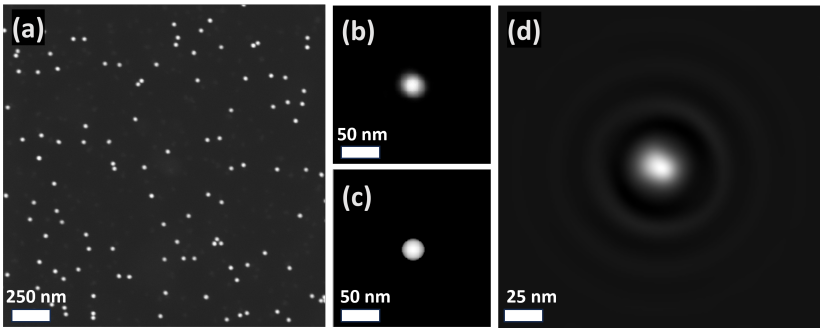

Figure 5.2: Probe intensity $|\psi_{sp}(x_i, y_i)|^2$ reconstruction process [6]. (a) Defocused ($\triangle z \approx -2\ \mu m$) BSE image of Au-NPs with multiple isolated NPs in the FOV, (b) Experimental image of a single NP captured after stacking to improve SNR, (c) Simulated image of a single NP using CASINO, (d) Reconstructed probe intensity (blurring function) using Wiener-filter-based deconvolution.

Figure 5.2. Just by qualitative analysis of the images and the respective probe intensities associated with them (see Figure 5.4), we can tell that the beam is astigmatic. As we go through the focal point, we can see that the image blur and the probe intensities rotate in the orthogonal direction. This also confirms the presence of the Gouy phase anomaly in an SEM as an astigmatic electron beam is tightly focused [141]. This was achieved by a controlled variation of the stigmators on the SEM to introduce astigmatism in the electron probe.

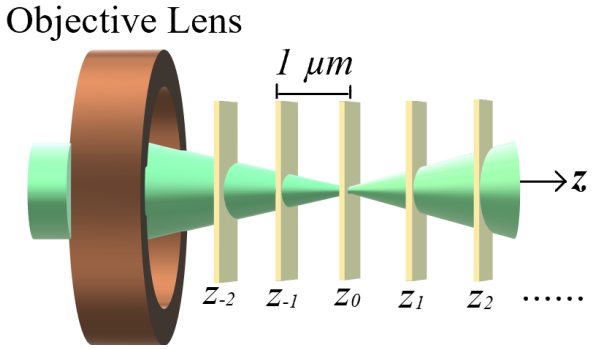

Figure 5.3: Schematic diagram for the imaging process for the experiment. The electron beam is focused in a $z-plane$ (z_0) and the specimen is moved with a step size of $1\mu m$ to get images in the different $z-planes$.

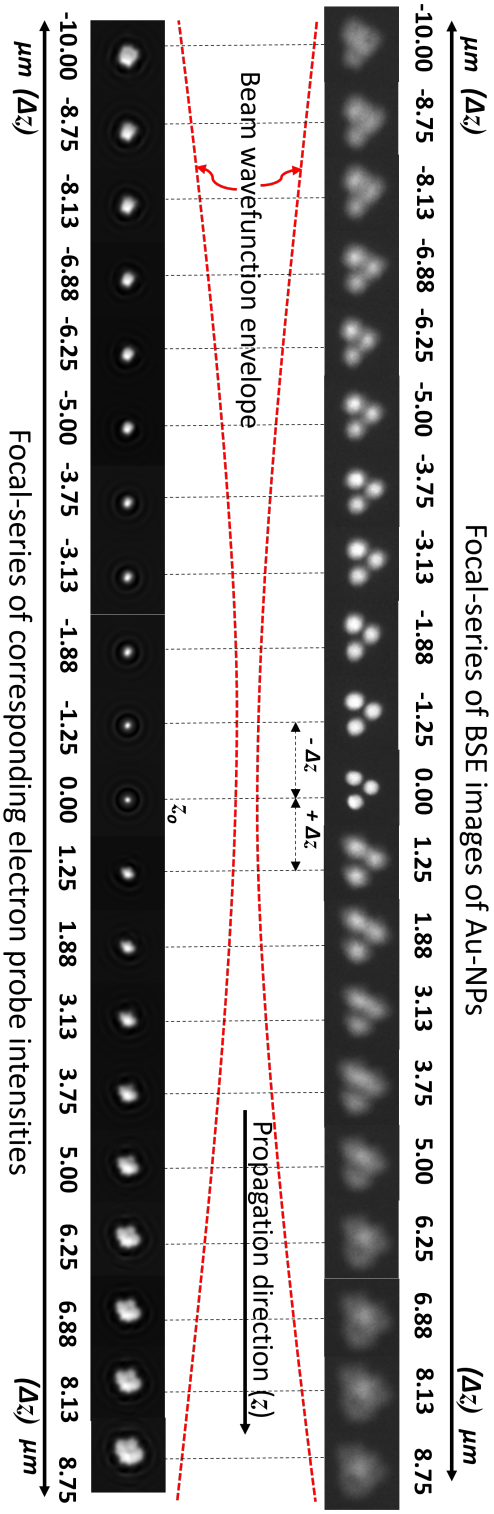

Figure 5.4: Experiment for generating data for phase retrieval of the electron probe. Focal series of gold nanoparticles (Au-NPs) BSE images (right), and their corresponding probe intensities reconstructed using AURA (left).

5.4 Iterative algorithm

We recover the probe phase using the defocus diversity-based non-interferometric phase retrieval [7]. As described above, the beam is focused on a central plane ($z = z_o$), and the specimen is moved along the *z-axis* by $\triangle z \approx 1\ \mu m$ step. At every $z = z_o + n \cdot \triangle z$, $\forall\, n \in [-9, +9]$ an SE/BSE image of the Au-nanoparticles is captured to create a through-focal-series of the specimen. Then for every SE/BSE image, the probe intensity is reconstructed using the method described above to get a focal series of probe intensities $\psi_{sp}|_{z_o \pm n\triangle z}$. This focal series of probe intensities shown in Figure 5.4 is the input to the iterative phase retrieval algorithm (see Figure 5.5). The algorithm starts

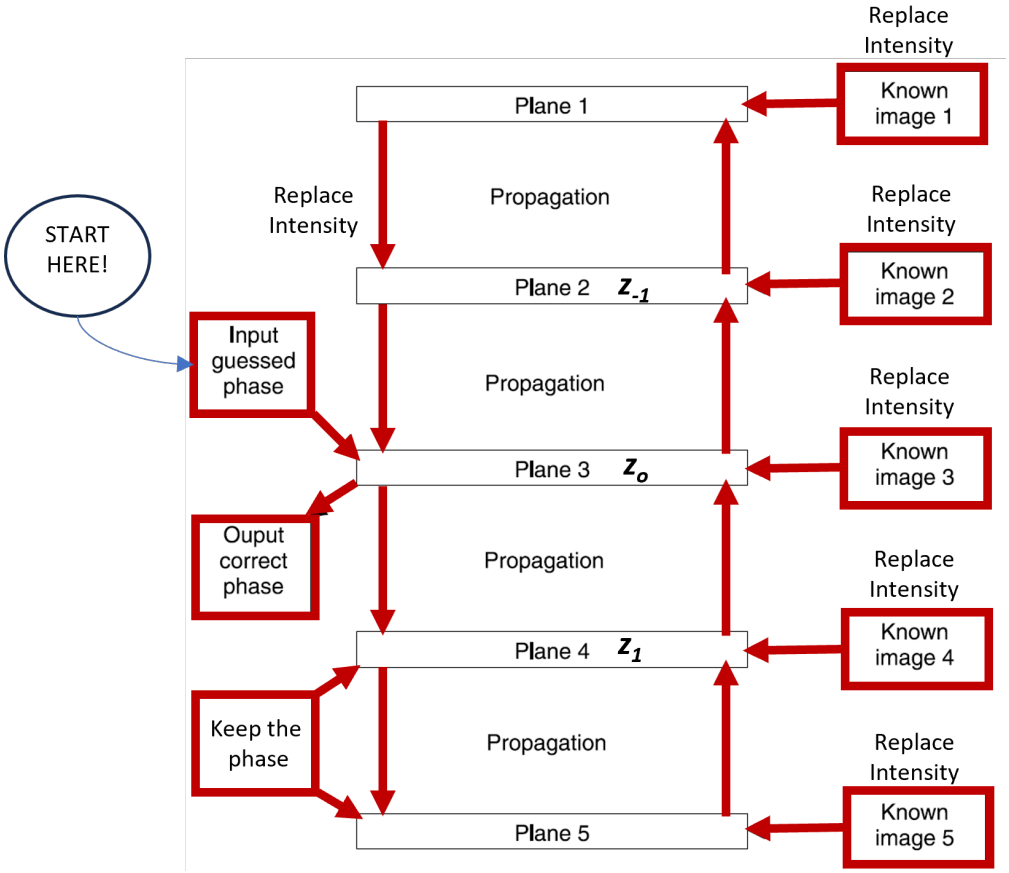

Figure 5.5: Iterative phase retrieval algorithm [7]. All propagations were done using the ASM propagator. Known images are the probe intensities recovered using AURA.

by initializing the probe wavefunction at the in-focus plane (z_o) as $\psi_{z_o} = |\psi_{z_o}|e^{i\phi_o}$, where $|\psi_{z_o}| = \sqrt{|\psi_{sp}|^2}$ is the reconstructed magnitude and ϕ_o is constant. ψ_{z_o} is then propagated to the next plane $z = z_1$ using the angular spectrum method (ASM) and we get $\psi_{z_1} = |\widetilde{\psi}_{z_1}|e^{i\phi_1}$. Here we keep the acquired phase ϕ_1 and replace the predicted magnitude $|\widetilde{\psi}_{z_1}|$with the ground truth $|\psi_{z_1}|$ and propagate to the next plane. This is repeated for all planes with the reconstructed probe intensities ($\psi_{sp}|_{z_o \pm n\triangle z}$) serving as the ground truth until we circle back to the central plane z_o, which completes one iteration. At the end of each iteration, we calculate the normalized sum-squared error ($n - SSE$) between the ground truth and predicted magnitude of the in-focus wavefunction shown in Equation (5.4.4). The whole process is repeated until a stable solution is reached with a sufficiently low $n - SSE$.

$$n - SSE = \frac{\sum_{pixels}(|\psi_{ground-truth}| - |\psi_{reconstruction}|)^2}{\sum_{pixels}|\psi_{ground-truth}|^2} \tag{5.4.4}$$

5.5 Reconstructed phase results

In this section, we present the first visualization of the electron probe phase reported in the SEM literature for three different datasets as shown in Figure 5.6. All probe intensity images were $N \times N = 256 \times 256$ pixels with a pixel size of $\Delta x = \Delta y = 1\ nm$. No padding was done for any of the probe intensity images. All the phase maps shown are wrapped in the interval $[-\pi, +\pi]$. All the reconstructed probe intensities serve as the ground truth constraint in each plane. Therefore, the phase recovered simultaneously in all the planes is the phase that would produce the probe intensities upon propagation starting at the central plane (z_o). Its important to note that the true probe phases (ϕ_{true}) are lost and the retrieved phase maps shown in Figure 5.6 are the estimated phases ($\phi_{estimated}$).

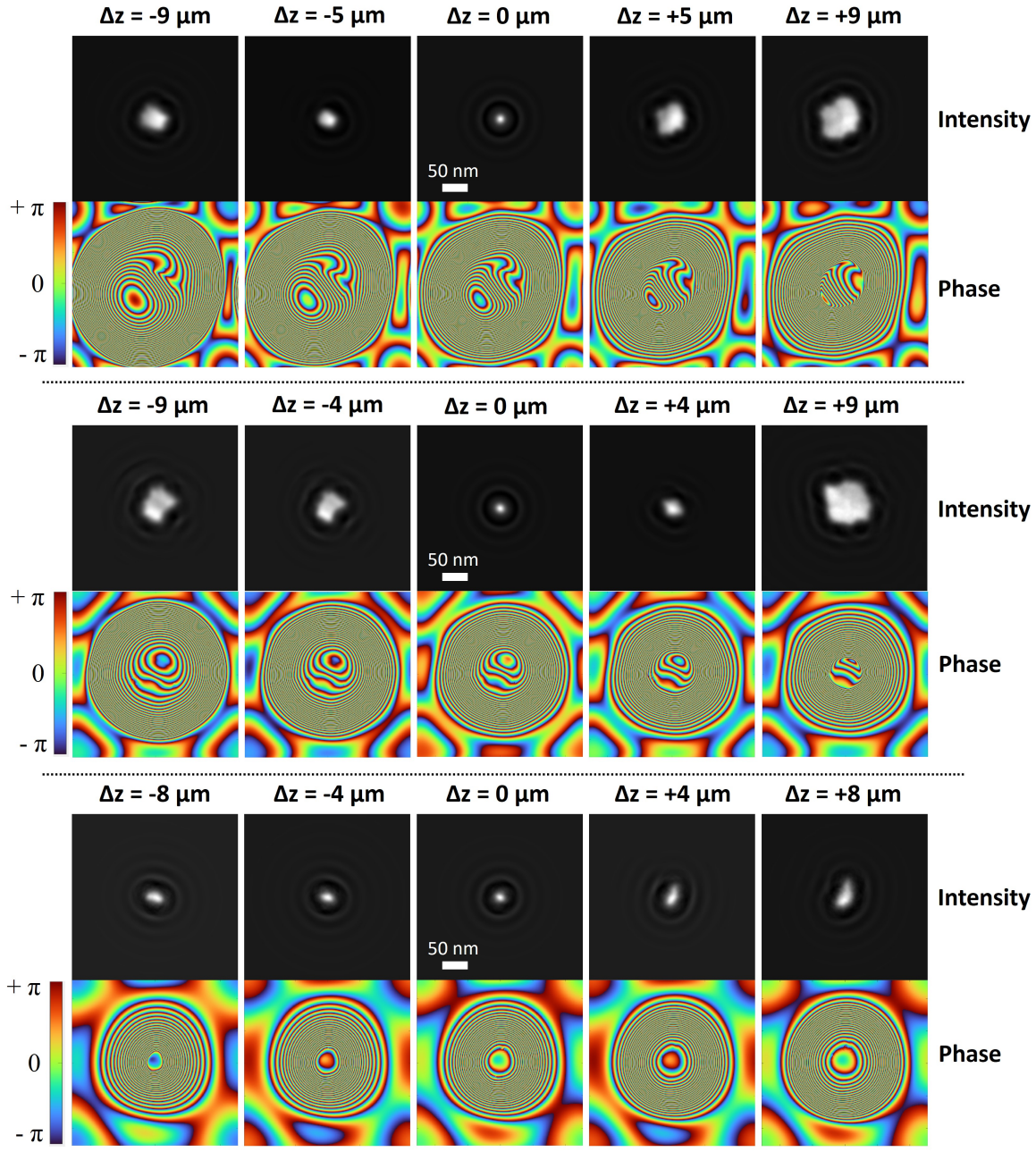

Figure 5.6: Phase retrieval of the electron probe using defocus. Probe intensity at different defocused planes and their corresponding recovered phases are shown. The phase is recovered for all $z-planes$ simultaneously. Results are shown for three different datasets with various degrees of astigamtism (all $E = 20\ keV$); Dataset 1: top, Dataset 2: middle, and Dataset 3:bottom. The recovered phase of the in-focus probe ($\Delta z = 0$) - Dataset 1: 19 images, ($x_{stig} = 0.4\%, y_{stig} = 0.8\%$), $n - SSE = 0.0052$ after $23.4k$ iterations, Dataset 2: 17 images, ($x_{stig} = 0.3\%$, $y_{stig} = 1.0\%$), $n - SSE = 0.03$ after $15.7k$iterations, Dataset 3: 17 images, ($x_{stig} = -0.1\%$, $y_{stig} = 0.7\%$), $n - SSE = 0.0034$ after $73.3k$ iterations.

5.6 Point-spread function of the SEM Optics

Once we have the phase of the beam after performing phase retrieval, what can we do with it? Let's go back to the imaging of the beam. We saw in chapter 2 that the PSF of the lens system with aberrations is defined as Step 1 in Table 5.1. Now, after

Step #	Mathematical description	Physical description
1	$PSF_{optics} = h(x_i, y_i) = \mathscr{F}[A(x_l, y_l)W(x_l, y_l)]$	Aperture PSF
2	$\psi_g = (1/M)\psi_{gun}$	Beam demagnification
3	$\psi_{sp} = \psi_g \otimes PSF_{optics} = \lvert\psi_{sp}\rvert\, e^{i\phi_{true}}$	Diffraction & aberrations
4	$\lvert\psi_{sp}\rvert^2 = \lvert\psi_g \otimes PSF_{optics}\rvert^2$	True phase lost

Table 5.1: Coherent imaging of the beam and the final probe formation process in a step-wise description

performing phase retrieval, we have an estimate of the phase $\phi_{estimated}$. Therefore, we have the complete description of the beam as we already have measured/estimated the probe intensity ($|\psi_{sp}|^2$).

$$\psi_{sp}^{reconstructed} = |\psi_{sp}|^2\, e^{i\phi_{estimated}} \qquad \text{complete probe reconstructed} \tag{5.6.5}$$

Once we have the complete probe distribution we can use the equation in Step 3 of Table 5.1, to calculate the PSF_{optics} as:

$$PSF_{optics} = \psi_{sp}^{reconstructed} \otimes \psi_g^{inverse} \tag{5.6.6}$$

where, $\psi_g^{inverse}$ is the inverse filter corresponding to ψ_g. This is very easily implemented in the Fourier domain where the convolution operation is transformed to a multiplication. A magnification of $M =\sim 10$ was used to show the results for the TESCAN MIRA3 SEM in Figure 5.7.

It is known that aberrations are the primary cause of poor resolution in uncorrected scanning electron microscopes (SEM). Here, we have shown the point-spread function

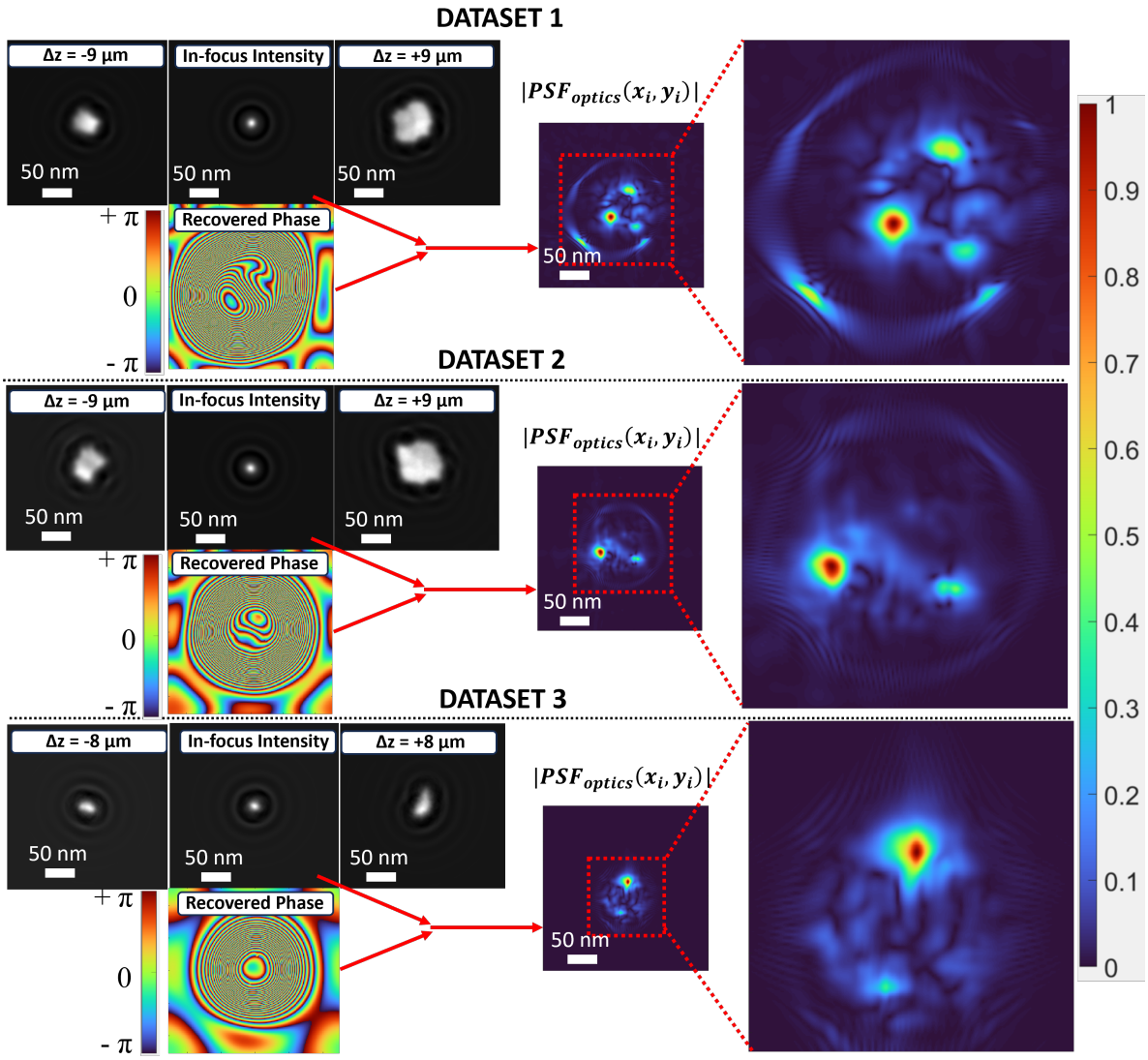

Figure 5.7: Visualization of the point-spread function of the probe forming optics (PSF_{optics}). The experiments were performed on a TESCAN MIRA3 SEM with a Schottky gun of virtual source size 20 nm. For all the datasets, the $|PSF_{optics}|$ shows that the performance of the lens system is tremendously limited by aberrations. The zoomed-in part shows the effect of the astigmatic phase for all datasets

of the probe forming optics (PSF_{optics}) for the first time in an uncorrected SEM. We show the $|PSF_{optics}|$ for three different datasets (see Figure 5.7).

Figure 5.7 shows the recovered phases of the in-focus probe intensities for all the datasets and the respective PSF_{optics}. Now, we can compute the point-spread function of the optics of an uncorrected SEM and appreciate how poor the lens system is. At lower voltages, the quality of phase retrieval was poor and therefore we have not included the PSF_{optics} results for lower beam energies $E = 2\ keV\ and\ 5\ keV$.

In this chapter, we demonstrated an experimental application of using a wave optical description of the SEM column and probe formation. Using the probe intensities generated from AURA, we were able to retrieve the lost phase of the electron probe using the defocus experiment. Based on the phase estimates ($\phi_{estimated}$) we were able to show the point-spread function of the lens system (PSF_{optics}) in an uncorrected SEM for the first time. This work is a major step towards wavefront-sensing-based aberration correction in SEM.

Chapter 6

Improving Phase Retrieval

In the last chapter, we discussed non-interferometric phase retrieval of the focused electron probe based on defocus diversity. Recovering lost phase for a beam intensity that is close to a Gaussian distribution is quite challenging and using defocus as a diversity method is not optimal. The defocus diversity method has some inherent drawbacks.

Drawbacks of defocus diversity

- We need to capture around $15 - 20$ images of the same nanoparticles. It is experimentally challenging to get a sufficiently accurate dataset. Ideally, the difference between the images should only be attributed to the change in focus. However, in the process of imaging the same field of view, the particle and the background themselves might change and move due to radiation damage and heating.
- High information diversity between measurements is always favorable for better phase retrieval using multiple measurements. But by adding defocus, the images still have high spatial information correlation which leads to stagnation of phase solution and very slow convergence.

One of our goals in this chapter is to point out that when working with iterative phase retrieval methods, the quality and efficiency of phase recovery are important. Information diversity between measurements can be introduced by defocus (see Chapter 5), angular diversity, transverse translation diversity, etc. [142, 143, 144]. However, for standard diversity methods, the measurements always have high structural similarity. For instance, as mentioned above for defocus, there exists a strong correlation in structural information between multiple measurements that leads to stagnation in phase solutions [145]. To perform an efficient non-interferometric phase retrieval of the electron probe, we require a much better diversity metric compared to controlled defocus. Therefore, we propose the use of electron vortex beams for this.

6.1 Electron vortex beams

Since the first experimental generation of electron vortex beams (EVB) in 2010 [146, 147], there has been a tremendous advancement in the field of structured electron beams [148]. Many techniques have been developed for the generation of EVBs [149, 150, 8, 151], a spiral phase plate (SPP) being the simplest one (see Figure 6.1). The thickness of the material is milled down using electron beam lithography or a focused-ion beam in a spiral pattern to induce the desired phase shift. The electron wavefunction traveling within the material experiences elastic scattering and accumulates a phase that is directly related to the mean inner potential and thickness of the material [99]. EVBs carry orbital angular momentum as evident from their helical phase structure. The EVB phase function can be represented as $e^{il\theta}$ where l represents the orbital angular momentum (OAM) state of the beam and θ is the azimuthal angle. The intensity of EVB is donut-shaped with zero energy at the center and the size (radius) is directly related to l.

EVBs have become a central area of interest within the electron microscopy and

electron lithography communities. They have found various applications in electron microscopy, spectroscopy, particle manipulation, etc. [148]. Therefore, we propose electron probe phase retrieval in scanning electron microscopy (SEM) as one of the novel applications of EVB.

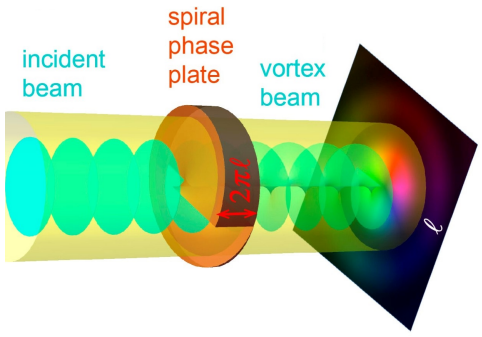

Figure 6.1: Electron vortex beam generation using Silicon Nitride/graphite spiral phase plates. This image was taken from Bliokh *et al.* [8].

6.2 Spiral phase diversity

Mathematically for a phase function $e^{i\varphi} = cos\varphi + isin\varphi$, maximum diversity can be introduced between two intensities if the information comes from quadrature components: $sin\varphi$ and $cos\varphi$ respectively. This kind of transformation is achieved using the Hilbert transform in two-dimensional (2D) functions. Vortex/spiral phase plate (SPP) to generate a beam with OAM state with $l = 1$ shown in Figure 6.2 is a generalization of the one-dimensional Hilbert transform [145].

It is well known that these vortex beams carry orbital angular momentum and have a spiral phase profile. This spiral phase can be used to produce probe intensities with highly non-redundant information as demonstrated below in Figure 6.2. We use these two intensities to perform phase retrieval of the electron probe. Therefore, in this work, we have proposed an experiment for robust phase retrieval of the electron probe based on spiral phase diversity [145, 152].

6.2.1 Proposed Experiment

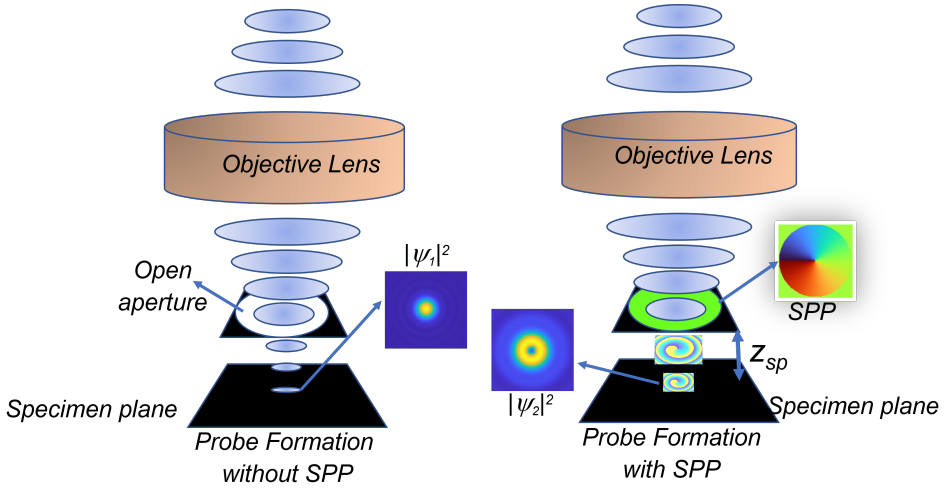

Figure 6.2: Proposed experimental setup to generate two probe intensities one with an open aperture (Bessel beam) and the other with SPP in the aperture (vortex beam). For this simulation z_{sp} was $2\mu m$ and beam energy was 20 keV

We begin by capturing the first high-resolution SEM image for a fixed set of SEM parameters (voltage, convergence angle, working distance, etc.) with an open aperture in the z_{sp} plane, as shown in Figure 6.2 (left). Then for the same operating parameters, we capture a second image after inserting a spiral phase plate (SPP) $exp(i\varphi)$ at a distance z_{sp} as shown in Figure 6.2 (right). The SPP generates a vortex beam that scans the specimen to produce an image with highly non-redundant data [145]. Our goal is to have substantial information diversity between the two SEM images. Then we use the method proposed by Zotta, Nevins *et al.* [6] to determine the probe intensity distribution from these two SEM images. For the first image, the probe magnitude should be close to a Gaussian ($|\psi_1|$) and for the second image, the probe magnitude should have a donut shape ($|\psi_2|$) (near zero energy at the center). The two probe intensities $|\psi_1|^2$ (without SPP) and $|\psi_2|^2$ (with SPP) are the inputs for the phase retrieval algorithm.

6.2.2 Iterative Algorithm

Many phase retrieval techniques based on alternative projections onto convex sets (APOCS), alternate between two planes of known information. For single intensity-based phase retrieval techniques (Gercherg-Saxton, Hybrid Input-Output) [80], the algorithm oscillates between the spatial and Fourier domains with constraints in both domains. Analogously, our iterative algorithm oscillates between the aperture plane and the specimen plane. We use the two known intensities $|\psi_1|^2$ and $|\psi_2|^2$, as constraints in the specimen plane. The known spiral phase function $exp(i\varphi)$, and the finite circular aperture act as constraints in the aperture plane, see Figure 6.3. The choice of the angular spectrum method (ASM) as the propagator function was based on the sampling constraints and propagation distance [5] in our simulation.

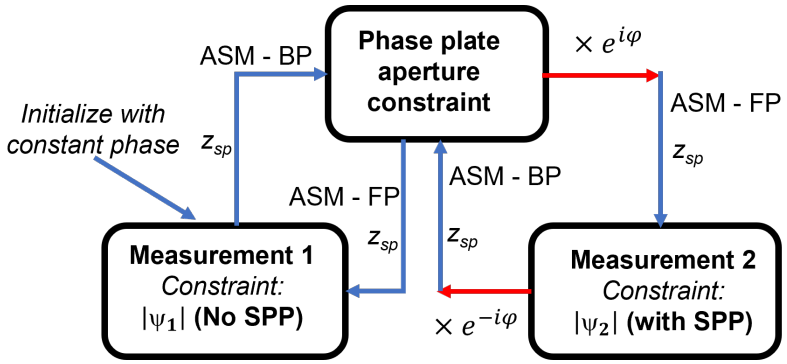

Figure 6.3: Flowchart of iteration used for SPP-based phase retrieval. ASM – Angular spectrum method, FP – Forward Propagation, BP – Backward propagation. Here $\varphi = l\theta$.

6.3 Simulation Results

In our simulations, to establish a convergence metric we have used normalized sum squared error [153] shown in Equation 6.3.1. One of the important simulation parameters to decide was the selection of the value for l. A higher value of l signifies higher

orbital angular momentum and a bigger radius of the intensity-donut for $|\psi_2|^2$ as shown in Figure 6.4.

$$n - SSE = \frac{\sum_{pixels}(|\psi_{ground-truth}| - |\psi_{reconstruction}|)^2}{\sum_{pixels}|\psi_{ground-truth}|^2} \tag{6.3.1}$$

We found in the simulation that theoretically the phase retrieval is independent of the value of l. Figure 6.4 shows the phase reconstruction for both $|\psi_1|^2$ (without SPP) and $|\psi_2|^2$ (with SPP) for $l = 1 - 5$. It can be seen that the reconstruction for both $|\psi_1|^2$ and $|\psi_2|^2$ are similar for all values of l. However, as we go higher in l, artifacts start appearing in $|\psi_2|^2$ because of aliasing. Since we want adequately sampled phases, lower values of $l = 1$ *or* 2 are recommended for the simulation or experiment.

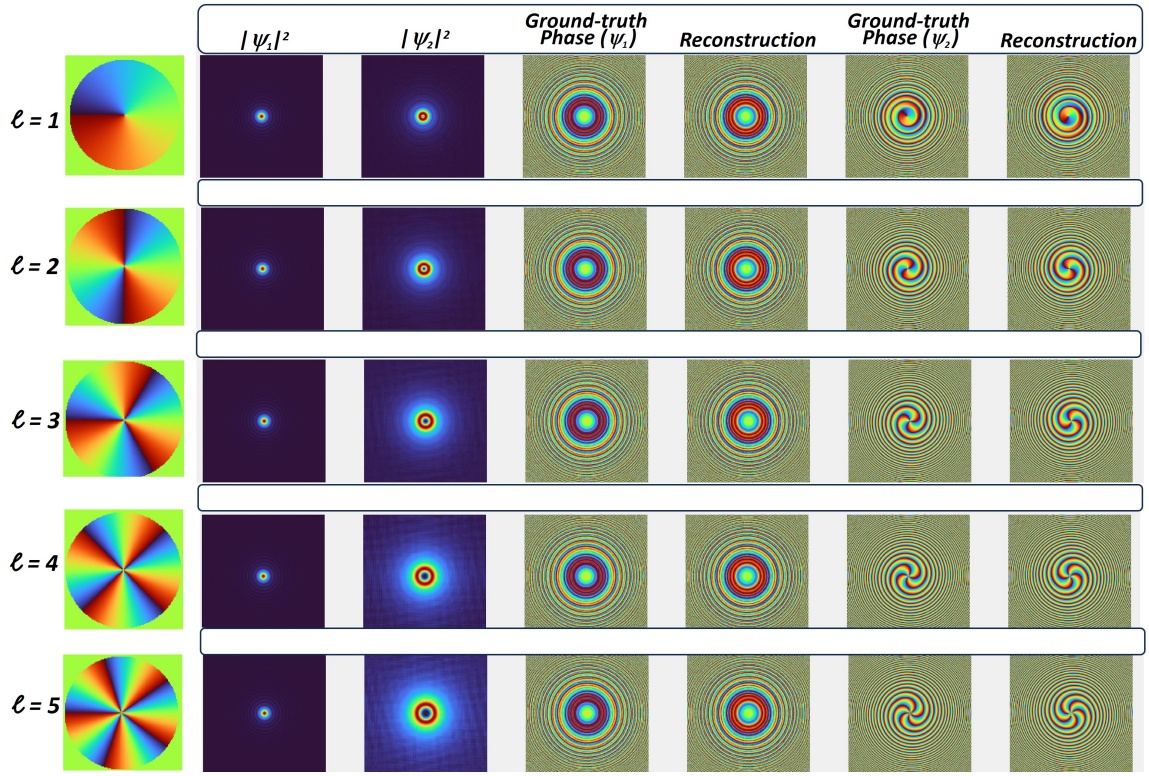

Figure 6.4: Phase reconstruction for $|\psi_1|^2$ and $|\psi_2|^2$ for different values of l. Ground-truth is the original phase that wasn't given as an input to the algorithm and reconstruction is the recovered phase using just the two intensities and the known spiral phase function.

Figure 6.5 shows robust phase retrieval of the electron probe with only two intensities. The $|\psi_2|^2$ generated for this used $l = 1$. The iterative algorithm converged quickly $(10 - 20$ iterations) and the normalized sum squared error (n-SSE) in $|\psi_1|^2$ reconstruction was very low. For the ideal probe (no aberrations added), the n-SSE was 0.01 and for the aberrated probe (defocus, spherical aberration, astigmatism present) n-SSE was 0.07. This simulation corroborates our hypothesis that designing a phase retrieval experiment based on spiral phase diversity is a much more efficient way to recover the probe phase compared to defocus diversity. The next step would be to model the SPP (Silicon-Nitride/Graphite) thickness to induce a 2π phase shift based on beam energy for actual fabrication.

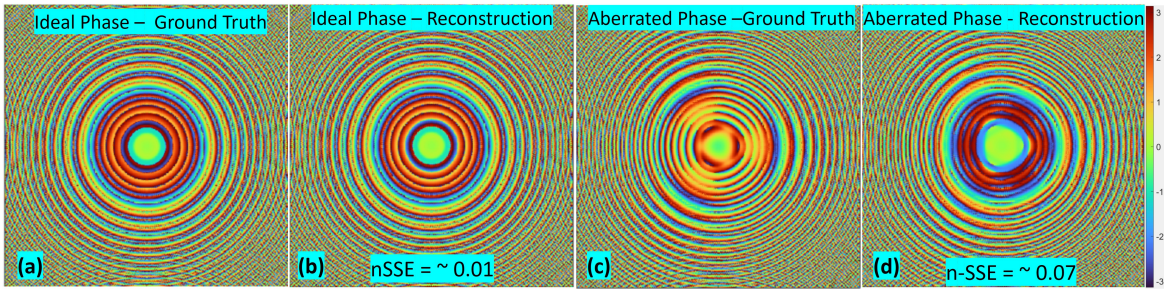

Figure 6.5: Phase retrieval simulation results for $|\psi_1|^2$ based on the proposed experimental setup. (a) Ideal probe phase with an open aperture, (b) Ideal phase reconstruction, (c) Aberrated probe phase with an open aperture, (d) Aberrated phase reconstruction.

In this chapter, we have proposed an efficient method to perform non-interferometric phase retrieval of the electron probe using electron vortex beams. We explained that spiral phase diversity produces highly non-redundant information between two measurements which addresses the limitations posed by the defocus diversity method. Using simulation we demonstrated that the proposed SPP experiment could perform stable phase retrieval with just two intensity measurements for both ideal and aberrated cases.

Chapter 7

Adaptive Electron Optics Pipeline for SEM

Chapters 5 and 6 were focused on the phase retrieval of the electron probe at the specimen plane. This chapter focuses on outlining the importance of having a complete description (intensity and phase) of the electron probe. As mentioned in Chapter 1, most of the aberration correction research in SEM has been focused on the development and improvement of the multipole correctors [26, 27]. It is time to move towards more accessible ways for aberration correction based on wavefront sensing.

The process of aberration correction starts with an aberration diagnostic/estimation method to quantify the aberration coefficients. Then a combination of multipole elements is used with the lens field to mitigate the aberration. The focus is to make the lenses better to get better output. However, correcting the optics using hardware has some inherent drawbacks as shown in Figure 7.1. Another way is working with the imperfect optics and then adding a reconstruction step to correct the output. It is important to stress that this is not image processing, but rather using the imperfect output for feedback in the system.

The bigger issue here is that there are no standard techniques for aberration quan-

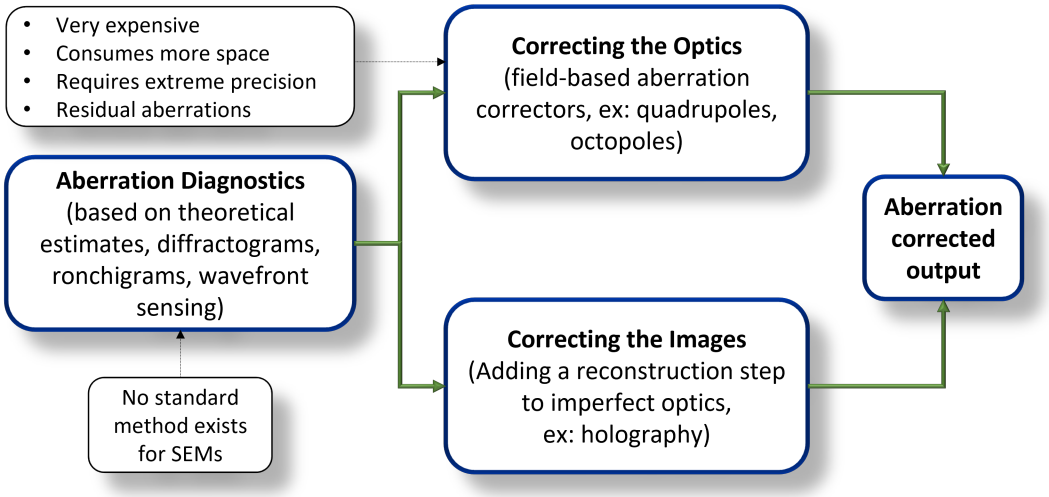

Figure 7.1: Aberration correction pipeline for electron microscopes.

tification in an uncorrected SEM (which is obvious because the beam information is lost and not imaged as an exit wave like in TEM or STEM). The aberration correction reported in LVSEM uses theoretical estimates of lower-order coefficients instead of actual aberration sensing. Most of the aberration correction has mostly been focused on perfecting the optics. Although they were a breakthrough in electron optics, they are very expensive, and the resolution is still limited by residual aberrations. Just to give some context let's see an example for an uncorrected SEM. An SEM without an aberration corrector can in practice resolve only $\sim 5-10\ nm$ at 20 keV that corresponds to a wavelength, $\lambda\ = \sim 8.5\ pm$. This makes the instrument's performance $\sim$ 1000 times poorer than the theoretical limit.

Over the last two decades, exploiting the quantum wave nature of electron beams has been the cornerstone for numerous advances in the field of electron microscopy and spectroscopy. The ability to manipulate and detect coherent electrons is at the core of many of these developments. However, it is curious to note that these experiments and their applications are almost exclusively realized for TEM or STEM. In newer aberration-corrected TEM and STEM, there is no need for phase retrieval and wave-

front sensing to get rid of aberrations. In such transmission microscopes with aberration correctors, we can directly train a system to produce sharp (aberration-corrected) images by tuning the aberration correctors using optimization techniques on the image features. Although very effective, these methods cannot be used for an SEM. Therefore, knowing the probe intensity and phase and hence the aberrated wavefront is the way to move forward toward "aberration-free" imaging in SEM.

One may enquire why is the wave nature of electrons more readily used in TEM or STEM. The answer lies probably in the similarity of working principle between light microscopes and TEM/STEM. A highly coherent source is used to illuminate the object and the transmitted interaction wave intensity is imaged on a pixelated detector device. The scanning electron microscope (SEM) is fundamentally different from all transmission microscopes which makes access to the illumination information obscure. The lens system forms a focused scanning electron probe (SEP) and the beam specimen interaction which is captured by multiple detectors based on respective generated signal energies. Since no exit wave can be imaged directly in SEM, the SEP information (intensity and phase) is completely lost. We have discussed the phase retrieval of the SEP in Chapter 5 and 6. This phase information is crucial for quantification and correction of the wavefront aberrations present in the lens system.

7.1 Adaptive optics pipeline

Adaptive optics in astronomy [154], light microscopy [155], and many other areas of imaging science have been very successful in producing excellent “aberration-free” images. A recent example would be one of the modern triumphs of science, the James Webb Space Telescope (JWST) which also employs a dedicated adaptive optics system [156]. Adaptive optics systems for aberration correction generally have a wavefront sensing mechanism followed by a dynamic wavefront modulator to produce the desired

aberration-free output as shown in Figure 7.2. For light optics, devices like deformable mirror devices (DMDs) and spatial light modulators (SLM) are available that offer dynamic control over the optical phase. In the case of electron optics, static/passive beam shaping [67, 99] has made tremendous progress, and dynamic control on wavefront shaping has shown rapid development [42, 44, 157, 47]. However, even with dynamic control of phase, we would still need a wavefront sensing mechanism and that is where the SEM problem becomes more challenging compared to TEM/STEM.

For TEM and STEM, numerous interferometric (holography-based, ptychography-based, etc.) or non-interferometric (defocus diversity-based, etc.) phase retrieval techniques already exist in literature. Based on Ronchigrams or just intensity images of the specimen the lost phase information can be recovered and then used to estimate aberrations in the optics. Furthermore, there also has been recent advancement in aberration diagnostic in STEM using artificial neural networks [158]. However, none of these techniques have been applied to the field of SEM until now. Apart from the work shown in this dissertation, no phase retrieval technique exists for beam wavefront sensing in SEMs. It is important to note that in SEM we are talking about wavefront sensing of the SEP (beam) before it has interacted with the specimen unlike in TEM/STEM. As methods for reconstructing the SEP intensity improve, there is a parallel need for realizing fast and efficient beam phase retrieval in SEM. The ability to estimate phase aberrations in the SEP through wavefront sensing will open the door for adaptive optics-based aberration correction and push the field towards aberration-free diffraction-limited imaging.

7.2 Wavefront sensing-based aberration correction

Field-based multipole aberration correctors are designed to counter specific low-order aberrations. Therefore, the resolution is still limited by the higher-order residual aber-

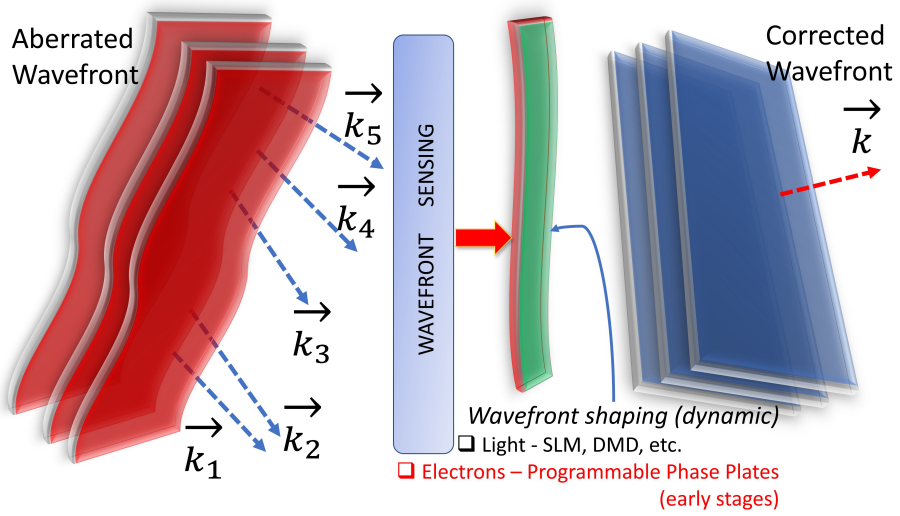

Figure 7.2: The schematic diagram for an adaptive optics setup. A wavefront sensing mechanism senses the aberrated wavefront and an inverse phase function is generated by the wavefront shaping device to get the desired ideal beam phase

rations. Wavefront sensing-based aberration correction using the SEP phase would be able to quantify aperture aberrations accurately. At higher voltages, where the chromatic aberration does not limit the resolution, all coherent aberrations can be accurately corrected, see Figure 7.3. Some beam phase retrieval techniques exist making it is possible to quantify chromatic aberrations too [159]. So in principle, even for incoherent aberrations like chromatic aberration at lower voltages, inverse phase masks can be used to mitigate their effect.

Now, here we outline the process of phase mask design for aberration correction. In Chapter 5, we have shown the PSF_{optics}, so we go back to its definition and take its

inverse Fourier transform.

$$\mathscr{F}^{-1}[PSF_{optics}] = h(x_i, y_i) = A(x_{ep}, y_{ep})W(x_{ep}, y_{ep}) \quad \text{(Aperture is known)} \tag{7.2.1}$$

$$W(x_{ep}, y_{ep}) = \mathscr{F}^{-1}[PSF_{optics}]/A(x_{ep}, y_{ep}) \quad \text{(Estimation of wavefront error)} \tag{7.2.2}$$

Now, as we have calculated $W(x_{ep}, y_{ep})$, the design for the phase mask is just the inverse filter W^{-1}. It is important to note that because of noise present in the system and inherent error in the estimation of PSF_{optics}, W^{-1} is always going to be a pseudo-inverse. In an ideal scenario, we aim to find a W^{-1} such that $W^{-1}W \approx \mathbb{I}$, where $\mathbb{I}$ is an identity matrix. Then, in theory, we will get an aberration-free aperture function which will produce aberration-free probes improving the final image resolution.

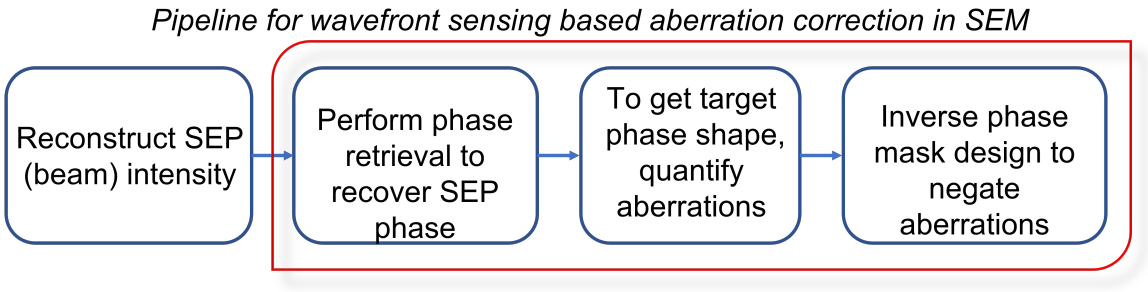

Figure 7.3: Flowchart of the aberration correction process based on wavefront sensing for SEM

In this chapter, we talked about the adaptive optics pipeline for SEM. Currently, no standard aberration diagnostics are available for the uncorrected SEM. Using the wavefront sensing pipeline shown in Figure 7.3, accurate aberration quantification can be possible. Therefore, aberration correction can be performed using wavefront sensing instead of multipole aberration correctors. In principle, achieving "aberration-free" probes should be possible using this pipeline and the resolution would not be limited by residual aberrations.

Chapter 8

Conclusion

8.1 Contribution Summary

SEMs have always been treated as secondary compared to TEM/STEM. As we move towards the quantum revolution, more and more applications of wave optical treatment of electron beams are being realized. However, all this progress typically is limited to TEM/STEM. This dissertation aims to change that. Our goal is the advancement of scanning electron microscopy as a domain where we can completely characterize the beam wavefunction as it is currently possible for TEM/STEM. For that, we have used the wave optical representation of the SEM optics. The first part of the dissertation was developing the wave-optical models for the SEM optics which are novel contributions to the field. Aberration diagnostics using deep learning and electron beam phase retrieval both are direct applications of the wave optical representation of the electron beam.

SEM-Nano (Chapter 2) represents a detailed study of the probe-forming capabilities of modern SEMs using a point-spread function model. It provides a microscopist the capability to visualize the probe under different operating conditions of the SEM in the presence of different aberrations. A tool like this was long overdue! The *plane-by-plane* propagation model (Chapter 3) addresses a different question: "Given an optical

column setup, can we model probe formation without using a point-spread function approximation ?"

For real-time aberration correction, fast and accurate aberration quantification is crucial. In Chapter 4 we developed a deep learning-based technique to do that. Given the probe intensity and its defocused version, this technique quantifies the aberration present in the probe. In this study, we also demonstrated aberration correction (on simulated data) and its effect on imaging.

Our main contribution is the phase retrieval of the electron probe in SEM (Chapter 5). We have recovered the lost phase of the electron probe using defocus variation. This has enabled us to visualize the point-spread function of the SEM optics (PSF_{optics}) for the first time. Having the probe intensity and phase opens a new area of wavefront-sensing-based aberration correction in SEM. Finally, we have proposed an experiment based on spiral phase diversity (Chapter 6) that will improve the efficiency of non-interferometric phase retrieval in SEM. Chapter 7 ties the whole dissertation together and provides an overview of where this research fits in the bigger picture of electron optics in SEM.

8.2 Experimental Recommendations

The defocus experiment is extremely sensitive to any movement of the specimen in the *z-plane*. It is important to ensure accuracy when moving the specimen by $\Delta z = 1\ \mu m$ step, as most sample stages are not accurately calibrated for such a small displacement. For example: Sometimes $\Delta z = 1\ \mu m$ might correspond to $1.25\ \mu m$ and sometimes it might correspond to $0.66\ \mu m$. It is important to notice that difference and capture that in the iterative algorithm for better phase reconstruction.

Furthermore, if the beam is sitting in the same area for a long time, the specimen might become contaminated which will degrade the quality of phase retrieval.

Therefore, the best way to capture the images is to image different nanoparticles whenever the specimen is moved in the *z-plane*. Finally, our reference image is a "single" Au-nanoparticle. Hence we want a FOV that has numerous $(50 - 100)$ well-isolated nanoparticles so that the stacking of the nanoparticle images can produce an error-free image of a single Au-nanoparticle with a higher *signal-to-noise* ratio.

8.3 Future Directions

Wave Optical Modeling and SEM image simulation

Modeling the electron source emission, the optical column, and the beam-matter interaction form a powerful end-to-end simulation of images that would be extremely close to actual images taken from an electron microscope. End-to-end simulations to generate final images exist for TEM/STEM [76].

However, that is not the case for SEM. Some simulations exist that simulate SEM images based on Monte-Carlo simulation of electron-matter interaction [59, 160, 161]. There has been work to model the SEM column and probe formation based on the classical picture [95, 93, 94] and the wave picture (see Chapters 2 and 3). There has been some recent research on wave optical modeling of electron source also [138, 139]. So, it would be fascinating to develop an end-to-end SEM simulation where the electron source emission, beam propagation, optics, and probe formation are all modeled using wave optics, and the electron-matter interaction is also integrated to have an accurate image simulation.

Improving Deconvolution

The AURA software uses a simple Wiener-filter-based deconvolution to reconstruct probe intensities. It is known that Wiener deconvolution adds ringing artifacts to the

reconstructions [162, 163] as it is based on the Fourier transform of the object and the image. The reference image of Au-nanoparticle doesn't have a Gaussian profile, therefore the Fourier spectrum has zeros (hence the rings). Therefore, moving to a more sophisticated deconvolution technique that works in the spatial domain (for example: Richardson-Lucy deconvolution) and recovers the probe intensity in the presence of noise more efficiently is an avenue for further improvement.

Aberration diagnostics on experimental probe images

Another exciting area of further research would be testing the performance of the deep learning technique on the experimental probe images obtained from deconvolution to quantify aberrations. The challenge would be to match the resolution (pixel size) of the images in the simulation and the experiment.

Phase Retrieval Performance

The robustness of PSF_{optics} calculation depends directly on how accurately we can estimate the probe phase. In Chapter 6 we discussed a better non-interferometric method based on spiral-phase diversity. In Chapter 5, the defocus diversity phase retrieval is not dependent on a constrained error minimization method. An upgrade to improve the defocus-diversity method would be using an algorithm where the convergence criteria are defined more rigorously [164]. Once we can recover stable solutions for probe phases, they can be decomposed into aberration polynomials to quantify individual aberration coefficients accurately. Moving towards an interferometric way of phase retrieval is also an avenue for further inquiry that removes the involvement of a simulated reference/object.

Bibliography

[1] B.J. Inkson. Chapter 2 - scanning electron microscopy (sem) and transmission electron microscopy (tem) for materials characterization. In *Materials Characterization Using Nondestructive Evaluation (NDE) Methods*, pages 17–43. 2016. (document), 1.1, 1.2

[2] Naresh Marturi. Vision and visual servoing for nanomanipulation and nanocharacterization in scanning electron microscope. page 23, 11 2013. (document), 1.3

[3] Pavel Vesely. Handbook of biological confocal microscopy, 3rd ed. by james b. pawley, editor. springer science + business media, llc, new york (2006). isbn 10: 0-387-25921-x; isbn 13: 987-0387-25921-5. *Scanning*, 29(3), 2007. (document), 1.4

[4] Surya Kamal and Richard K Hailstone. SEM Nano: An Electron Wave Optical Simulation for the Scanning Electron Microscope. *Microscopy and Microanalysis*, 28(2):441–453, 04 2022. (document), 1.5, 3.1, 3.3.5, 4, 4.1, 4.2.1, 4.3.2, 5, 5.2

[5] Wenhui Zhang, Hao Zhang, Colin JR Sheppard, and Guofan Jin. Analysis of numerical diffraction calculation methods: from the perspective of phase space optics and the sampling theorem. *JOSA A*, 37(11):1748–1766, 2020. (document), 3.2.2.2, 3.2, 6.2.2

[6] Matthew Zotta, Mandy Nevins, Richard Hailstone, and Eric Lifshin. The determination and application of the point spread function in the scanning electron microscope. *Microscopy and Microanalysis*, 24:396–405, 08 2018. (document), 1.3, 1.4, 2.2.6, 5.2.2, 5.2, 6.2.1

[7] LJ Allen and MP Oxley. Phase retrieval from series of images obtained by defocus variation. *Optics communications*, 199(1-4):65–75, 2001. (document), 5.1.1, 5.4, 5.5

[8] Konstantin Y Bliokh, Igor P Ivanov, Giulio Guzzinati, Laura Clark, Ruben Van Boxem, Armand Béché, Roeland Juchtmans, Miguel A Alonso, Peter Schattschneider, Franco Nori, et al. Theory and applications of free-electron vortex states. *Physics Reports*, 690:1–70, 2017. (document), 6.1, 6.1

[9] D. Voelz. Computational fourier optics: A matlab tutorial. 2011. (document), 2.2.3, 2.2.4, 2.1, 2.2.5.1, 2.2.7, 3.2.1

[10] Albert V Crewe, M Isaacson, and D Johnson. A simple scanning electron microscope. *Review of Scientific Instruments*, 40(2):241–246, 1969. 1.1

[11] Albert V Crewe, J Wall, and J Langmore. Visibility of single atoms. *science*, 168(3937):1338–1340, 1970. 1.1

[12] DH Shin, EJ Kirkland, and J Silcox. Annular dark field electron microscope images with better than 2 å resolution at 100 kv. *Applied physics letters*, 55(23):2456–2458, 1989. 1.1

[13] David J Smith. Progress and perspectives for atomic-resolution electron microscopy. *Ultramicroscopy*, 108(3):159–166, 2008. 1.1

[14] Stephen J Pennycook. Seeing the atoms more clearly: Stem imaging from the crewe era to today. *Ultramicroscopy*, 123:28–37, 2012. 1.1

[15] Yimei Zhu, H Inada, K Nakamura, and J Wall. Imaging single atoms using secondary electrons with an aberration-corrected electron microscope. *Nature materials*, 8(10):808–812, 2009. 1.1

[16] David C Joy. Second best no more. *Nature Materials*, 8(10):776–777, 2009. 1.1

[17] Kalsoom Akhtar, Shahid Ali Khan, Sher Bahadar Khan, and Abdullah M Asiri. Scanning electron microscopy: Principle and applications in nanomaterials characterization. *Handbook of materials characterization*, pages 113–145, 2018. 1.1

[18] Beverley J Inkson. Scanning electron microscopy (sem) and transmission electron microscopy (tem) for materials characterization. In *Materials characterization using nondestructive evaluation (NDE) methods*, pages 17–43. Elsevier, 2016. 1.1

[19] Oliver D Patterson, Julie Lee, Chris Lei, and Dave Salvador. E-beam inspection for detection of sub-design rule physical defects. In *2012 SEMI Advanced Semiconductor Manufacturing Conference*, pages 383–387. IEEE, 2012. 1.1

[20] Li Chen, Jun Xu, and Jing Chen. Applications of scanning electron microscopy in earth sciences. *Science China Earth Sciences*, 58:1768–1778, 2015. 1.1

[21] KE Carr. Applications of scanning electron microscopy in biology. *International review of cytology*, 30:183–255, 1971. 1.1

[22] PB Fischer and Stephen Y Chou. 10 nm electron beam lithography and sub-50 nm overlay using a modified scanning electron microscope. *Applied physics letters*, 62(23):2989–2991, 1993. 1.1

[23] David C Joy. Low voltage scanning electron microscopy-current status, present problems, and future solutions. *e-Journal of Surface Science and Nanotechnology*, 4:369–375, 2006. 1.1

[24] Jon Orloff. *Handbook of charged particle optics*. CRC press, 2017. 1.1, 3.1

[25] Otto Scherzer. Über einige fehler von elektronenlinsen. *Zeitschrift für Physik*, 101(9-10):593–603, 1936. 1.1

[26] Joachim Zach and Maximilian Haider. Aberration correction in a low voltage sem by a multipole corrector. *Nuclear Instruments and Methods in Physics Research Section A: Accelerators, Spectrometers, Detectors and Associated Equipment*, 363(1-2):316–325, 1995. 1.1, 7

[27] Joachim Zach and Maximilian Haider. Correction of spherical and chromatic aberration in a low voltage sem. *Optik (Stuttgart)*, 98(3):112–118, 1995. 1.1, 7

[28] Harald Rose. Outline of a spherically corrected semiaplanatic medium-voltage transmission electron microscope. *Optik*, 85:19–24, 1990. 1.1

[29] Hiroyoshi Kazumori, Kazuhiro Honda, Miyuki Matsuya, Masaru Date, and Charles Nielsen. Field emission sem with a spherical and chromatic aberration corrector. *Microscopy and Microanalysis*, 10(S02):1370–1371, 2004. 1.1

[30] Munehiro Ogasawara, Yuji Fukudome, Kiyoshi Hattori, Shuichi Tamamushi, Soshi Koikari, and Kazunori Onoguchi. Automatic focusing and astigmatism correction method based on fourier transform of scanning electron microscope images. *Japanese journal of applied physics*, 38(2R):957, 1999. 1.1

[31] Shinobu Uno, Kazuhiro Honda, Natsuko Nakamura, Miyuki Matsuya, and Joachim Zach. Aberration correction and its automatic control in scanning electron microscopes. *Optik*, 116(9):438–448, 2005. 1.1

[32] F Zemlin, K Weiss, P Schiske, W Kunath, and K-H Herrmann. Coma-free alignment of high resolution electron microscopes with the aid of optical diffractograms. *Ultramicroscopy*, 3:49–60, 1978. 1.1, 4.2.1

[33] Robert M Glaeser, Dieter Typke, Peter C Tiemeijer, James Pulokas, and Anchi Cheng. Precise beam-tilt alignment and collimation are required to minimize the phase error associated with coma in high-resolution cryo-em. *Journal of structural biology*, 174(1):1–10, 2011. 1.1

[34] Takeshi Kawasaki, Tomonori Nakano, and Kotoko Hirose. Developing an aberration-corrected schottky emission sem and method for measuring aberration. *Microelectronic engineering*, 86(4-6):1017–1020, 2009. 1.1, 4.2.1

[35] PW Hawkes. The correction of electron lens aberrations. *Ultramicroscopy*, 156:A1–A64, 2015. 1.1

[36] David C Joy. The aberration corrected sem. In *AIP Conference Proceedings*, volume 788, pages 535–542. American Institute of Physics, 2005. 1.1, 3.1

[37] RH Van Aken, DJ Maas, CW Hagen, JE Barth, and P Kruit. Design of an aberration corrected low-voltage sem. *Ultramicroscopy*, 110(11):1411–1419, 2010. 1.1

[38] Hideto Dohi and Pieter Kruit. Design for an aberration corrected scanning electron microscope using miniature electron mirrors. *Ultramicroscopy*, 189:1–23, 2018. 1.1

[39] Diederik J Maas, Sander Henstra, Marcel Krijn, and Sjoerd Mentink. Electrostatic aberration correction in low-voltage sem. In *Charged Particle Detection, Diagnostics, and Imaging*, volume 4510, pages 205–217. SPIE, 2001. 1.1

[40] Christoph Weißbäcker and Harald Rose. Electrostatic correction of the chromatic and of the spherical aberration of charged-particle lenses. *Journal of electron microscopy*, 50(5):383–390, 2001. 1.1

[41] Christoph Weißbäcker and Harald Rose. Electrostatic correction of the chromatic and of the spherical aberration of charged-particle lenses (part ii). *Journal of electron microscopy*, 51(1):45–51, 2002. 1.1

[42] Jo Verbeeck, Armand Béché, Knut Müller-Caspary, Giulio Guzzinati, Minh Anh Luong, and Martien Den Hertog. Demonstration of a 2× 2 programmable phase plate for electrons. *Ultramicroscopy*, 190:58–65, 2018. 1.1, 4, 7.1

[43] Amir H Tavabi, Paolo Rosi, Enzo Rotunno, Alberto Roncaglia, Luca Belsito, Stefano Frabboni, Giulio Pozzi, Gian Carlo Gazzadi, Peng-Han Lu, Robert Nijland, et al. Experimental demonstration of an electrostatic orbital angular momentum sorter for electron beams. *Physical review letters*, 126(9):094802, 2021. 1.1, 4

[44] Francisco Vega Ibáñez, Armand Béché, and Johan Verbeeck. Can a programmable phase plate serve as an aberration corrector in the transmission electron microscope (tem)? *Microscopy and Microanalysis*, 29(1):341–351, 2023. 1.1, 4, 7.1

[45] Marius Constantin Chirita Mihaila, Philipp Weber, Matthias Schneller, Lucas Grandits, Stefan Nimmrichter, and Thomas Juffmann. Transverse electron-beam shaping with light. *Physical Review X*, 12(3):031043, 2022. 1.1, 4

[46] Ori Reinhardt and Ido Kaminer. Theory of shaping electron wavepackets with light. *ACS Photonics*, 7(10):2859–2870, 2020. 1.1, 4

[47] Chu-Ping Yu, Francisco Vega Ibañez, Armand Béché, and Johan Verbeeck. Quantum wavefront shaping with a 48-element programmable phase plate for electrons. *SciPost Physics*, 15(6):223, 2023. 1.1, 4, 7.1

[48] Surya Kamal and Richard K Hailstone. Need for wavefront sensing in scanning electron microscopy, 2023. 1.1

[49] Helen ML Faulkner, Leslie J Allen, MP Oxley, and D Paganin. Computational aberration determination and correction. *Optics communications*, 216(1-3):89–98, 2003. 1.1

[50] Leslie J Allen, MP Oxley, and D Paganin. Computational aberration correction for an arbitrary linear imaging system. *Physical Review Letters*, 87(12):123902, 2001. 1.1

[51] O. (Ed.). Jon. *Handbook of Charged Particle Optics (2nd ed.). CRC Press.*, pages 391–435. (2009). 1.3, 1.3, 2.1, 2.2.6

[52] Matthew Zotta, Sharadh Jois, Prathamesh Dhakras, Miguel Rodriguez, and J. Lee. Direct measurement of the electron beam spatial intensity profile via carbon nanotube tomography. *Nano Letters*, 19:4435–4441, 06 2019. 1.3, 1.4

[53] Matthew Zotta and Eric Lifshin. Scanning electron microscope point spread function determination through the use of particle dispersions. *Microscopy and Microanalysis*, 23:124–125, 07 2017. 1.3, 1.4

[54] Yudhishthir Kandel, Matthew Zotta, Andrew Caferra, Richard Moore, and Eric Lifshin. Measurement of the electron beam point spread function (psf) in a scanning electron microscope (sem). *Microscopy and Microanalysis*, 21:699–700, 08 2015. 1.3, 1.4

[55] M. S. Bronsgeest, J. E. Barth, L. W. Swanson, and P. Kruit. Probe current, probe size, and the practical brightness for probe forming systems. *Journal of Vacuum Science & Technology B: Microelectronics and Nanometer Structures Processing, Measurement, and Phenomena*, 26(3):949–955, 2008. 1.3, 2.1, 3.1, 3.3.5

[56] M. Haider, S. Uhlemann, and J. Zach. Upper limits for the residual aberrations of a high-resolution aberration-corrected stem. *Ultramicroscopy*, 81(3):163–175, 2000. 1.3, 2.2.4, 4.1, 4.2.1, 4.3.1

[57] Jolana Kološová, Tomáš Hrnčíř, Jaroslav Jiruše, Miroslav Rudolf, and Jakub Zlámal. On the calculation of sem and fib beam profiles. *Microscopy and Microanalysis*, 21(S4):206–211, 2015. 1.4

[58] Eric Lifshin, Matthew Zotta, David Frey, Sarah Lifshin, Mandy Nevins, and Jeffrey Moskin. A software approach to improving sem resolution, image quality, and productivity. *Microscopy Today*, 25(3):18–25, 2017. 1.4, 5.2.2

[59] Dominique Drouin, Alexandre Réal Couture, Dany Joly, Xavier Tastet, Vincent Aimez, and Raynald Gauvin. Casino v2. 42—a fast and easy-to-use modeling tool for scanning electron microscopy and microanalysis users. *Scanning: The Journal of Scanning Microscopies*, 29(3):92–101, 2007. 1.4, 4.3.2, 8.3

[60] Lixin Zhang, Mathijs W.H. Garming, Jacob P. Hoogenboom, and Pieter Kruit. Beam displacement and blur caused by fast electron beam deflection. *Ultramicroscopy*, 211:112925, 2020. 2.1

[61] M. J. Fransen, J. S. Faber, Th. L. van Rooy, P. C. Tiemeijer, and P. Kruit. Experimental evaluation of the extended schottky model for zro/w electron emission. *Journal of Vacuum Science & Technology B: Microelectronics and Nanometer Structures Processing, Measurement, and Phenomena*, 16(4):2063–2072, 1998. 2.1

[62] M.J. Fransen, Th. L. Van Rooy, P.C. Tiemeijer, M.H.F. Overwijk, J.S. Faber, and P. Kruit. On the electron-optical properties of the zro/w schottky electron emitter. volume 111 of *Advances in Imaging and Electron Physics*, pages 91–166. Elsevier, 1999. 2.1

[63] Peter Hawkes and Erwin Kasper. Chapter 43 - general features of electron guns. In Peter Hawkes and Erwin Kasper, editors, *Principles of Electron Optics (Second Edition)*, pages 1051–1061. Academic Press, second edition edition, 2018. 2.1

[64] Peter Hawkes and Erwin Kasper. Chapter 44 - theory of electron emission. In Peter Hawkes and Erwin Kasper, editors, *Principles of Electron Optics (Second Edition)*, pages 1063–1081. Academic Press, second edition edition, 2018. 2.1

[65] L Reimer. Scanning electron microscopy: Physics of image formation and microanalysis, second edition. *Measurement Science and Technology*, 11:1826, 11 2000. 2.1, 2.2.2, 3.1, 3.2.1, 4.2.1, 4.2.1, 5.2

[66] Max Born, Emil Wolf, A. B. Bhatia, P. C. Clemmow, D. Gabor, A. R. Stokes, A. M. Taylor, P. A. Wayman, and W. L. Wilcock. *Principles of Optics: Electromagnetic Theory of Propagation, Interference and Diffraction of Light*. Cambridge University Press, 7 edition, 1999. 2.1, 2.2.5.3

[67] Roy Shiloh, Peng-Han Lu, Roei Remez, Amir H Tavabi, Giulio Pozzi, Rafal E Dunin-Borkowski, and Ady Arie. Nanostructuring of electron beams. *Physica Scripta*, 94(3):034004, jan 2019. 2.1, 3.1, 3.2.2.4, 3.2.2.4, 7.1

[68] I. Madan, G. M. Vanacore, S. Gargiulo, T. LaGrange, and F. Carbone. The quantum future of microscopy: Wave function engineering of electrons, ions, and nuclei. *Applied Physics Letters*, 116(23):230502, 2020. 2.1

[69] Jo Verbeeck, H Tian, and Peter Schattschneider. Production and application of electron vortex beams. *Nature*, 467:301–4, 09 2010. 2.1

[70] T. Řiháček, M. Horák, T. Schachinger, F. Mika, M. Matějka, S. Krátký, T. Fořt, T. Radlička, C.W. Johnson, L. Novák, B. Sed'a, B.J. McMorran, and I. Müllerová. Beam shaping and probe characterization in the scanning electron microscope. *Ultramicroscopy*, 225:113268, 2021. 2.1, 3.1

[71] Albert V. Crewe. Optimization of small electron probes. *Ultramicroscopy*, 23(2):159–167, 1987. 2.1

[72] J. E. Barth and P. Kruit. Addition of different contributions to the charged particle probe size. *Optik*, 101:101–109, 1996. 2.1, 3.1

[73] Mitsugu Sato. Properties of the imaging performance of an electron optical system for sem. *Nuclear Instruments and Methods in Physics Research Section A: Accelerators, Spectrometers, Detectors and Associated Equipment*, 645(1):74–78, 2011. The Eighth International Conference on Charged Particle Optics. 2.1, 3.1

[74] Mandy C. Nevins, Matthew D. Zotta, Richard K. Hailstone, and Eric Lifshin. Visualizing astigmatism in the sem electron probe. *Microscopy and Microanalysis*, 24(S1):604–605, 2018. 2.1, 3.1

[75] C. Dwyer, R. Erni, and J. Etheridge. Measurement of effective source distribution and its importance for quantitative interpretation of stem images. *Ultramicroscopy*, 110(8):952–957, 2010. PROCEEDINGS OF THE INTERNATIONAL WORKSHOP ON ENHANCED DATA GENERATED BY ELECTRONS. 2.1, 2.2.5.1, 2.2.5.3, 5.2.1

[76] J. Barthel. Dr. probe: A software for high-resolution stem image simulation. *Ultramicroscopy*, 193:1–11, 2018. 2.1, 3.1, 8.3

[77] Raynald Gauvin, Eric Lifshin, Hendrix Demers, Paula Horny, and Helen Campbell. Win x-ray: A new monte carlo program that computes x-ray spectra obtained with a scanning electron microscope. *Microscopy and microanalysis : the official journal of Microscopy Society of America, Microbeam Analysis Society, Microscopical Society of Canada*, 12:49–64, 03 2006. 2.1

[78] Dominique Drouin, Alexandre Réal Couture, Dany Joly, Xavier Tastet, Vincent Aimez, and Raynald Gauvin. Casino v2.42—a fast and easy-to-use modeling tool for scanning electron microscopy and microanalysis users. *Scanning*, 29(3):92–101, 2007. 2.1, 4.3.2

[79] Ray F. Egerton. *The Transmission Electron Microscope*, pages 57–92. Springer US, Boston, MA, 2005. 2.2.1, 4.1

[80] Joseph W Goodman. *Introduction to Fourier optics, 4th ed.*, volume 1. 2017. 2.2.3, 2.2.3, 3.1, 3.2.2.2, 3.2.2.3, 4.1, 5.1.1, 5.2, 6.2.2

[81] Jacob Wirth. *Point Spread Function and Modulation Transfer Function Engineering*. PhD thesis, 2019. Thesis. Rochester Institute of Technology. 2.2.3, 2.2.3

[82] D. Typke and K. Dierksen. Determination of image aberrations in high-resolution electron microscopy using diffractogram and cross-correlation methods. *Optik*, 99:155–166, 1995. 2.2.4, 4.2.1

[83] O.L. Krivanek, N. Dellby, and A.R. Lupini. Towards sub-Å electron beams. *Ultramicroscopy*, 78(1):1–11, 1999. 2.2.4

[84] Xifeng Xiao and David Voelz. Wave optics simulation approach for partial spatially coherent beams. *Opt. Express*, 14(16):6986–6992, Aug 2006. 2.2.5.1

[85] Frank Dubois, Maria-Luisa Novella Requena, Christophe Minetti, Olivier Monnom, and Eric Istasse. Partial spatial coherence effects in digital holographic microscopy with a laser source. *Appl. Opt.*, 43(5):1131–1139, Feb 2004. 2.2.5.1

[86] Martin J. Bastiaans. Application of the wigner distribution function to partially coherent light. *J. Opt. Soc. Am. A*, 3(8):1227–1238, Aug 1986. 2.2.5.1

[87] G. Gbur and T.D. Visser. Chapter 5 - the structure of partially coherent fields. volume 55 of *Progress in Optics*, pages 285–341. Elsevier, 2010. 2.2.5.1

[88] Tatiana Latychevskaia. Spatial coherence of electron beams from field emitters and its effect on the resolution of imaged objects. *Ultramicroscopy*, 175:121–129, 2017. 2.2.5.1

[89] L. Trepte K.J. Hanssen. *Optik*, 32:519–538, 1971. 2.2.5.1

[90] Jay Theodore Cremer. Chapter 3 - geometric neutron and x-ray optics – aberrations. In Jay Theodore Cremer, editor, *Advances in Imaging and Electron Physics*, volume 172 of *Advances in Imaging and Electron Physics*, pages 429–495. Elsevier, 2012. 2.2.5.2

[91] P. Nellist and J. Rodenburg. Beyond the conventional information limit: the relevant coherence function. *Ultramicroscopy*, 54:61–74, 1994. 2.2.5.2

[92] P.C. Tiemeijer, P.M. Mul, Bert Freitag, S. Kujawa, and Jan Ringnalda. Breaking the spherical and chromatic aberration barrier in transmission electron microscopy. *Ultramicroscopy*, 102, 04 2005. 2.2.5.2, 2.2.5.2

[93] Eric Munro. Computer programs for the design and optimization of electron and ion beam lithography systems. *Nuclear Instruments and Methods in Physics*

Research Section A: Accelerators, Spectrometers, Detectors and Associated Equipment, 258(3):443–461, 1987. 3.1, 8.3

[94] Eric Munro, Haoning Liu, Catherine Rouse, and John Rouse. A simulation program for electron mirrors using boundary element method. In *Advances in Imaging and Electron Physics*, volume 212, pages 87–110. Elsevier, 2019. 3.1, 8.3

[95] J Zlámal and B Lencová. Development of the program eod for design in electron and ion microscopy. *Nuclear Instruments and Methods in Physics Research Section A: Accelerators, Spectrometers, Detectors and Associated Equipment*, 645(1):278–282, 2011. 3.1, 8.3

[96] D Cubric, B Lencova, FH Read, and J Zlamal. Comparison of fdm, fem and bem for electrostatic charged particle optics. *Nuclear Instruments and Methods in Physics Research Section A: Accelerators, Spectrometers, Detectors and Associated Equipment*, 427(1-2):357–362, 1999. 3.1

[97] John A Rouse. Three dimensional computer modeling of electron optical systems. In *Advances in imaging and electron physics*, volume 208, pages 129–241. Elsevier, 2018. 3.1

[98] David Edwards Jr. A new paradigm for fdm: cylindrically symmetric electrostatics. In *Advances in Imaging and Electron Physics*, volume 215, pages 141–180. Elsevier, 2020. 3.1

[99] Dolev Roitman, Roy Shiloh, Peng-Han Lu, Rafal E Dunin-Borkowski, and Ady Arie. Shaping of electron beams using sculpted thin films. *ACS photonics*, 8(12):3394–3405, 2021. 3.1, 6.1, 7.1

[100] Jolana Kološová, Tomáš Hrnčíř, Jaroslav Jiruše, Miroslav Rudolf, and Jakub Zlámal. On the calculation of sem and fib beam profiles. *Microscopy and Microanalysis*, 21(S4):206–211, 2015. 3.1

[101] Surya Kamal and Richard Hailstone. Modeling sem column, probe formation, and imaging using fourier optics. *Microscopy and Microanalysis*, 27(S1):3336–3337, 2021. 3.1

[102] MV Klein and TE Furtak. Optics, 2d. ed., 1986. 3.1

[103] David G Voelz and Michael C Roggemann. Digital simulation of scalar optical diffraction: revisiting chirp function sampling criteria and consequences. *Applied optics*, 48(32):6132–6142, 2009. 3.2.1, 3.2.2.3

[104] WO Saxton. A new way of measuring microscope aberrations. *Ultramicroscopy*, 81(2):41–45, 2000. 3.2.2.4

[105] Peter W Hawkes and Erwin Kasper. *Principles of Electron Optics, Volume 3: Fundamental Wave Optics*. Academic press, 2022. 3.2.2.4, 5.2.1

[106] Roy Shiloh, Roei Remez, and Ady Arie. Prospects for electron beam aberration correction using sculpted phase masks. *Ultramicroscopy*, 163:69–74, 2016. 3.2.2.4

[107] Giulio Pozzi, Marco Beleggia, Takeshi Kasama, and Rafal E Dunin-Borkowski. Interferometric methods for mapping static electric and magnetic fields. *Comptes rendus physique*, 15(2-3):126–139, 2014. 3.2.2.4

[108] Stephan Uhlemann and Maximilian Haider. Residual wave aberrations in the first spherical aberration corrected transmission electron microscope. *Ultramicroscopy*, 72(3-4):109–119, 1998. 4.1, 4.2.1

[109] Kotoko Hirose, Tomonori Nakano, and Takeshi Kawasaki. Automatic aberration-correction system for scanning electron microscopy. *Microelectronic engineering*, 88(8):2559–2562, 2011. 4.2.1

[110] RL Barnes and IK Openshaw. A comparison of experimental and theoretical cs values for some probe-forming lenses. *Journal of Physics E: Scientific Instruments*, 1(6):628, 1968. 4.2.1

[111] Yair Rivenson, Zoltán Göröcs, Harun Günaydin, Yibo Zhang, Hongda Wang, and Aydogan Ozcan. Deep learning microscopy. *Optica*, 4(11):1437–1443, 2017. 4.2.3

[112] Kevin de Haan, Zachary S Ballard, Yair Rivenson, Yichen Wu, and Aydogan Ozcan. Resolution enhancement in scanning electron microscopy using deep learning. *Scientific reports*, 9(1):12050, 2019. 4.2.3

[113] Francisco López de la Rosa, Roberto Sánchez-Reolid, José L Gómez-Sirvent, Rafael Morales, and Antonio Fernández-Caballero. A review on machine and deep learning for semiconductor defect classification in scanning electron microscope images. *Applied Sciences*, 11(20):9508, 2021. 4.2.3

[114] Jeffrey M Ede. Deep learning in electron microscopy. *Machine Learning: Science and Technology*, 2(1):011004, 2021. 4.2.3

[115] Sergei V Kalinin, Colin Ophus, Paul M Voyles, Rolf Erni, Demie Kepaptsoglou, Vincenzo Grillo, Andrew R Lupini, Mark P Oxley, Eric Schwenker, Maria KY Chan, et al. Machine learning in scanning transmission electron microscopy. *Nature Reviews Methods Primers*, 2(1):11, 2022. 4.2.3

[116] Leslie N Smith and Nicholay Topin. Super-convergence: Very fast training of neural networks using large learning rates. In *Artificial intelligence and machine*

learning for multi-domain operations applications, volume 11006, pages 369–386. SPIE, 2019. 4.2.4

[117] Rick P Millane. Phase retrieval in crystallography and optics. *JOSA A*, 7(3):394–411, 1990. 5.1

[118] C Fienup and J Dainty. Phase retrieval and image reconstruction for astronomy. *Image recovery: theory and application*, 231:275, 1987. 5.1

[119] Kishore Jaganathan, Yonina C Eldar, and Babak Hassibi. Phase retrieval: An overview of recent developments. *Optical Compressive Imaging*, pages 279–312, 2016. 5.1

[120] Helen Mary Louise Faulkner and JM Rodenburg. Movable aperture lensless transmission microscopy: a novel phase retrieval algorithm. *Physical review letters*, 93(2):023903, 2004. 5.1

[121] Wim Coene, Guido Janssen, Marc Op de Beeck, and Dirk Van Dyck. Phase retrieval through focus variation for ultra-resolution in field-emission transmission electron microscopy. *Physical Review Letters*, 69(26):3743, 1992. 5.1, 5.1.1

[122] F Hüe, JM Rodenburg, AM Maiden, Francis Sweeney, and PA Midgley. Wavefront phase retrieval in transmission electron microscopy via ptychography. *Physical Review B*, 82(12):121415, 2010. 5.1

[123] Liqi Zhou, Jingdong Song, Judy S Kim, Xudong Pei, Chen Huang, Mark Boyce, Luiza Mendonça, Daniel Clare, Alistair Siebert, Christopher S Allen, et al. Low-dose phase retrieval of biological specimens using cryo-electron ptychography. *Nature communications*, 11(1):2773, 2020. 5.1

[124] Georgios Varnavides, Stephanie M Ribet, Steven E Zeltmann, Yue Yu, Benjamin H Savitzky, Vinayak P Dravid, Mary C Scott, and Colin Ophus. Iterative phase retrieval algorithms for scanning transmission electron microscopy. *arXiv preprint arXiv:2309.05250*, 2023. 5.1

[125] Georgios Varnavides, Stephanie Ribet, Reed Yalisove, Joel Moore, Colin Ophus, and Mary C Scott. Simultaneous electrostatic and magnetic vector potential phase retrieval using electron ptychography, 2023. 5.1

[126] Ulf Schnars, Claas Falldorf, John Watson, Werner Jüptner, Ulf Schnars, Claas Falldorf, John Watson, and Werner Jüptner. *Digital holography*. Springer, 2015. 5.1

[127] Bahram Javidi, Artur Carnicer, Arun Anand, George Barbastathis, Wen Chen, Pietro Ferraro, JW Goodman, Ryoichi Horisaki, Kedar Khare, Malgorzata Kujawinska, et al. Roadmap on digital holography. *Optics express*, 29(22):35078–35118, 2021. 5.1

[128] John M Rodenburg. Ptychography and related diffractive imaging methods. *Advances in imaging and electron physics*, 150:87–184, 2008. 5.1

[129] John Rodenburg and Andrew Maiden. Ptychography. *Springer Handbook of Microscopy*, pages 819–904, 2019. 5.1

[130] Franz Pfeiffer. X-ray ptychography. *Nature Photonics*, 12(1):9–17, 2018. 5.1

[131] Kedar Khare, Mansi Butola, and Sunaina Rajora. Non-interferometric phase retrieval. In *Fourier Optics and Computational Imaging*, pages 217–235. Springer, 2023. 5.1, 5.1.1

[132] Joseph W Goodman. *Statistical optics*. John Wiley & Sons, 2015. 5.2.1

[133] Leonard Mandel and Emil Wolf. *Optical coherence and quantum optics*. Cambridge university press, 1995. 5.2.1

[134] B Cho, T Ichimura, R Shimizu, and C Oshima. Quantitative evaluation of spatial coherence of the electron beam from low temperature field emitters. *Physical review letters*, 92(24):246103, 2004. 5.2.1

[135] Tatiana Latychevskaia. Spatial coherence of electron beams from field emitters and its effect on the resolution of imaged objects. *Ultramicroscopy*, 175:121–129, 2017. 5.2.1

[136] Tatiana Latychevskaia. Phase retrieval methods applied to coherent imaging. In *Advances in Imaging and Electron Physics*, volume 218, pages 1–62. Elsevier, 2021. 5.2.1

[137] Shuhei Hatanaka and Jun Yamasaki. Quantitative measurement of spatial coherence of electron beams emitted from a thermionic electron gun. *JOSA A*, 38(12):1893–1900, 2021. 5.2.1

[138] Faruk Krečinić and Ralph Ernstorfer. Wave-mechanical electron-optical modeling of field-emission electron sources. *Physical Review Applied*, 15(6):064031, 2021. 5.2.1, 8.3

[139] Soichiro Tsujino. On the brightness, transverse emittance, and transverse coherence of field emission beam. *Journal of Vacuum Science & Technology B*, 40(3), 2022. 5.2.1, 8.3

[140] Mandy C Nevins. *Point Spread Function Determination in the Scanning Electron Microscope and Its Application in Restoring Images Acquired at Low Voltage*. Rochester Institute of Technology, 2019. 5.2.2

[141] TC Petersen, DM Paganin, Matthew Weyland, Tapio Petteri Simula, Samuel Anthony Eastwood, and Michael John Morgan. Measurement of the gouy phase anomaly for electron waves. *Physical Review A*, 88(4):043803, 2013. 5.3

[142] Bruce H Dean and Charles W Bowers. Diversity selection for phase-diverse phase retrieval. *JOSA A*, 20(8):1490–1504, 2003. 6

[143] Manuel Guizar-Sicairos and James R Fienup. Phase retrieval with transverse translation diversity: a nonlinear optimization approach. *Optics express*, 16(10):7264–7278, 2008. 6

[144] Peifan Liu, Jun Yan, Hao Hao, and Ying K Wu. Phase retrieval for short wavelength orbital angular momentum beams using knife-edge diffraction. *Optics Communications*, 474:126077, 2020. 6

[145] Manoj Kumar Sharma, Charu Gaur, Paramasivam Senthilkumaran, and Kedar Khare. Phase imaging using spiral-phase diversity. *Applied Optics*, 54(13):3979–3985, 2015. 6, 6.2, 6.2.1

[146] Masaya Uchida and Akira Tonomura. Generation of electron beams carrying orbital angular momentum. *nature*, 464(7289):737–739, 2010. 6.1

[147] Johan Verbeeck, He Tian, and Peter Schattschneider. Production and application of electron vortex beams. *Nature*, 467(7313):301–304, 2010. 6.1

[148] Konstantin Y Bliokh, Ebrahim Karimi, Miles J Padgett, Miguel A Alonso, Mark R Dennis, Angela Dudley, Andrew Forbes, Sina Zahedpour, Scott W Hancock, Howard M Milchberg, et al. Roadmap on structured waves. *Journal of Optics*, 25(10):103001, 2023. 6.1

[149] Benjamin J McMorran, Amit Agrawal, Ian M Anderson, Andrew A Herzing, Henri J Lezec, Jabez J McClelland, and John Unguris. Electron vortex beams with high quanta of orbital angular momentum. *science*, 331(6014):192–195, 2011. 6.1

[150] Jérémie Harris, Vincenzo Grillo, Erfan Mafakheri, Gian Carlo Gazzadi, Stefano Frabboni, Robert W Boyd, and Ebrahim Karimi. Structured quantum waves. *Nature Physics*, 11(8):629–634, 2015. 6.1

[151] Ruixuan Yu, Pengcheng Huo, Mingze Liu, Wenqi Zhu, Amit Agrawal, Yan-qing Lu, and Ting Xu. Generation of perfect electron vortex beam with a customized beam size independent of orbital angular momentum. *Nano Letters*, 23(6):2436–2441, 2023. 6.1

[152] Santiago Echeverri-Chacón, René Restrepo, Carlos Cuartas-Vélez, and Néstor Uribe-Patarroyo. Vortex-enhanced coherent-illumination phase diversity for phase retrieval in coherent imaging systems. *Optics letters*, 41(8):1817–1820, 2016. 6.2

[153] Sudheer Jawla, Jean-Philippe Hogge, and Stefano Alberti. Theoretical investigation of iterative phase retrieval algorithm for quasi-optical millimeter-wave rf beams. *IEEE transactions on plasma science*, 37(3):403–413, 2009. 6.3

[154] Richard Davies and Markus Kasper. Adaptive optics for astronomy. *Annual Review of Astronomy and Astrophysics*, 50:305–351, 2012. 7.1

[155] Martin J Booth. Adaptive optical microscopy: the ongoing quest for a perfect image. *Light: Science & Applications*, 3(4):e165–e165, 2014. 7.1

[156] D Scott Acton, J Scott Knight, A Contos, Stefano Grimaldi, J Terry, P Lightsey, A Barto, B League, Bruce Dean, J Scott Smith, et al. Wavefront sensing and

controls for the james webb space telescope. In *Space Telescopes and Instrumentation 2012: Optical, Infrared, and Millimeter Wave*, volume 8442, pages 877–887. SPIE, 2012. 7.1

[157] Stephanie M Ribet, Steven E Zeltmann, Karen C Bustillo, Rohan Dhall, Peter Denes, Andrew M Minor, Roberto Dos Reis, Vinayak P Dravid, and Colin Ophus. Design of electrostatic aberration correctors for scanning transmission electron microscopy. *Microscopy and Microanalysis*, 29(6):1950–1960, 2023. 7.1

[158] Giovanni Bertoni, Enzo Rotunno, Daan Marsmans, Peter Tiemeijer, Amir H Tavabi, Rafal E Dunin-Borkowski, and Vincenzo Grillo. Near-real-time diagnosis of electron optical phase aberrations in scanning transmission electron microscopy using an artificial neural network. *Ultramicroscopy*, 245:113663, 2023. 7.1

[159] Matthew D Bergkoetter, Brian E Kruschwitz, Seung-Whan Bahk, and James R Fienup. Measurement of chromatic aberrations using phase retrieval. *JOSA A*, 38(12):1853–1865, 2021. 7.2

[160] Hendrix Demers, Nicolas Poirier-Demers, Alexandre Réal Couture, Dany Joly, Marc Guilmain, Niels de Jonge, and Dominique Drouin. Three-dimensional electron microscopy simulation with the casino monte carlo software. *Scanning*, 33(3):135–146, 2011. 8.3

[161] LCPM van Kessel and CW Hagen. Nebula: Monte carlo simulator of electron–matter interaction. *SoftwareX*, 12:100605, 2020. 8.3

[162] MK Kaushik, GC Chandrakala, and R Abhinay. Ringing and blur artifact removal in image processing applications. In *2018 Second International Conference on Intelligent Computing and Control Systems (ICICCS)*, pages 260–264. IEEE, 2018. 8.3

[163] Filip Šroubek, Tomáš Kerepeckỳ, and Jan Kamenickỳ. Iterative wiener filtering for deconvolution with ringing artifact suppression. In *2019 27th European Signal Processing Conference (EUSIPCO)*, pages 1–5. IEEE, 2019. 8.3

[164] Takahiro Tamura, Yukinori Nakane, Hiroshi Nakajima, Shigeo Mori, Ken Harada, and Yoshizo Takai. Phase retrieval using through-focus images in lorentz transmission electron microscopy. *Microscopy*, 67(3):171–177, 2018. 8.3